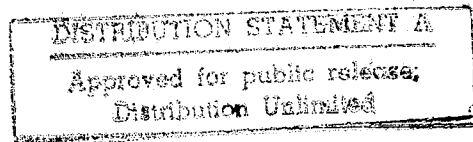


APPLIED
COMPUTATIONAL
ELECTROMAGNETICS
SOCIETY
JOURNAL

March 1995
Vol. 10 No. 1

ISSN 1054-4887



19950308 169

GENERAL PURPOSE AND SCOPE. The Applied Computational Electromagnetics Society Journal hereinafter known as the *ACES Journal* is devoted to the exchange of information in computational electromagnetics, to the advancement of the state-of-the-art, and to the promotion of related technical activities. A primary objective of the information exchange is the elimination of the need to "re-invent the wheel" to solve a previously-solved computational problem in electrical engineering, physics, or related fields of study. The technical activities promoted by this publication include code validation, performance analysis, and input/output standardization; code or technique optimization and error minimization; innovations in solution technique or in data input/output; identification of new applications for electromagnetics modeling codes and techniques; integration of computational electromagnetics techniques with new computer architectures; and correlation of computational parameters with physical mechanisms.

SUBMISSIONS CONTENT. The *ACES Journal* welcomes original, previously unpublished papers, relating to **applied computational electromagnetics**.

Typical papers will represent the computational electromagnetics aspects of research in electrical engineering, physics, or related disciplines. However, papers which represent research in **applied computational electromagnetics** itself are equally acceptable.

For additional details, see "Information for Authors", elsewhere in this issue.

SUBSCRIPTIONS. All members of the Applied Computational Electromagnetics Society (ACES) who have paid their subscription fees are entitled to receive the *ACES Journal* with a minimum of two issues per calendar year. **Current annual subscription fees are subject to change every 1 April.** Current fees are:

AREAS: U.S. and Canada: **SURFACE/AIRMAIL:** \$65 Individual, \$115 Organizational ; Mexico, Central & So. America: **AIRMAIL:** \$70 Individual, \$115 Organizational, **SURFACE MAIL:** \$68; Europe, Former USSR, Turkey, Scandinavia, **AIRMAIL:** \$78 Individual, \$115 Organizational, **SURFACE MAIL:** \$68; Asia, Africa, Middle East and Pacific Rim: **AIRMAIL:** \$85 Individual, \$115 Organizational, **SURFACE MAIL:** \$68. **FULL-TIME STUDENTS:** \$25.00. REMIT TO "ACES" BY: (1) BANK DRAFTS (MUST BE DRAWN ON U.S. BANK with US BANK ADDRESS); (2) INTERNATIONAL MONEY ORDER, (3) TRAVELER'S CHECKS IN U.S. DOLLARS; (4) VISA, MASTERCARD, DISCOVER AND AMEX CREDIT CARDS.

Back issues, when available, are \$15.00 each. Subscriptions to ACES, orders for back issues of the *ACES Journal* and changes of addresses should be sent to:

Dr. Richard Adler
ACES Executive Officer
ECE Department, Code ECAB
Naval Postgraduate School
833 Dyer Road, Room 437
Monterey, CA 93943-5121 USA

Allow four week's advance notice for change of address. Claims for missing issues will not be honored because of insufficient notice or address change or loss in mail unless the secretary is notified within 60 days for USA and Canadian subscribers or 90 days for subscribers in other countries, from the last day of the month of publication. For information regarding reprints of individual papers or other materials, see "Information for Authors".

LIABILITY. Neither ACES or the *ACES Journal* editors are responsible for any consequence of misinformation or claims, express or implied, in any published material in an *ACES Journal* issue. This also applies to advertising, for which only camera-ready copies are accepted. Authors are responsible for information contained in their papers. If any material submitted for publication includes material which has already been published elsewhere, it is the author's responsibility to obtain written permission to reproduce such material.

APPLIED
COMPUTATIONAL
ELECTROMAGNETICS
SOCIETY
Journal

March 1995
Vol. 10 No. 1

ISSN 1054-4887

The ACES Journal is abstracted in INSPEC, in Engineering Index, and in DTIC.

The second, third, fourth, and fifth illustrations on the front cover have been obtained from Lawrence Livermore National laboratory.

The first illustration on the front cover has been obtained from FLUX2D software, CEDRAT S.S. France, MAGSOFT Corporation, New York.

THE APPLIED COMPUTATIONAL ELECTROMAGNETICS SOCIETY JOURNAL

EDITORS

EDITOR-IN-CHIEF/ACES

W. Perry Wheless, Jr.
University of Alabama, EE Dept.
PO Box 870286
Tuscaloosa, AL 35487-0286 USA

EDITOR-IN-CHIEF/JOURNAL

Duncan C. Baker
EE Dept. University of Pretoria
0002 Pretoria, SOUTH AFRICA

MANAGING EDITOR

Richard W. Adler
ECE Department Code ECAB
833 Dyer Rd. Room 437
Naval Postgraduate School
Monterey, CA 93943-5121, USA

ASSOC. EDITOR-IN-CHIEF/JOURNAL

Adalbert Konrad
University of Toronto
Toronto, Ont. CANADA

EDITOR-IN-CHIEF, EMERITUS

Robert M. Bevensee
Box 812
Alamo, CA 94507-0516 USA

EDITOR-IN-CHIEF, EMERITUS

David E. Stein
USAF Scientific Advisory Board
Pentagon
Washington, DC 20330 USA

Brian A. Austin
University of Liverpool
Liverpool, UK

Christian Hafner
Swiss Federal Inst. of Technology
Zurich, SWITZERLAND

Peter Krylstedt
National Defence Research Est.
Sundbyberg, SWEDEN

Fulvio Bessi
Ingegneria dei Sistemi S.p.A.
Pisa, ITALY

Roger Harrington
Syracuse University
Syracuse, NY, U.S.A.

Stanley Kubina
Concordia University
Montreal, Quebec, CANADA

Robert Bevensee
Box 812
Alamo, CA USA

Donald F. Herrick
ERIM
Ann Arbor, MI, USA

Karl J. Langenberg
Universitat Kassel
Kassel, GERMANY

John R. Bowler
University of Surrey
Surrey, UK

Kueichien C. Hill
Wright Laboratory
Wright-Patterson AFB, OH, USA

Ronald Marhefka
Ohio State University
Columbus, OH, USA

Robert T. Brown
Lockheed Aeronautical Sys. Co.
Valencia, CA, USA

Todd H. Hubing
University of Missouri-Rolla
Rolla, MO, USA

Gerald Meunier
INPG/ENSIEG
St. Martin-d'Heres Cedex, FRANCE

Chalmers M. Butler
Clemson University
Clemson, SC, USA

Nathan Ida
The University of Akron
Akron, OH, USA

Edmund K. Miller
Ohio University
Athens, OH, USA

Edgar Coffey
Advanced Electromagnetics
Albuquerque, NM, USA

Magdy F. Iskander
University of Utah
Salt Lake City, UT, USA

Kenzo Miya
University of Tokyo
Tokyo, JAPAN

Tony Fleming
Telecom Australia
Clayton, Victoria, AUSTRALIA

Kiyohiko Itoh
Hokkaido University
Sappora, JAPAN

Osama A. Mohammed
Florida International University
Miami, FL, USA

EDITORS (Continued)

Pat Foster
Microwave & Antenna Systems
Gt. Malvern, Worc. UK

Randy J. Jost
SRI International
Arlington, VA, USA

Giorgio Molinari
University of Genova
Genova, ITALY

Gregory R. Haack
DSTO
AUSTRALIA

Linda P.B. Katehi
University of Michigan
Ann Arbor, MI, USA

Frederic A. Molinet
Societe Mothesim
Le Plessis-Robinson, FRANCE

Gerrit Mur
Technische Universiteit Delft
Delft, NETHERLANDS

Chris Smith
Kaman Sciences Corp.
Colorado Springs, CO, U.S.A.

Frank Walker
Boeing Defence & Space Group
Seattle, WA U.S.A.

Takayoshi Nakata
Okayama University
Okayama, JAPAN

David E. Stein
USAF Scientific Advisory Board
Pentagon
Washington, DC 20330, USA

Keith W. Whites
University of Kentucky
Lexington, KY, U.S.A.

Andrew F. Peterson
Georgia Institute of Technology
Atlanta, GA, U.S.A.

C.W. "Bill" Trowbridge
Vector Fields Limited
Oxford, UK

John W. Williams
SAIC
Germantown, MD 20874

Harold A. Sabbagh
Sabbagh Associates
Bloomington, IN, U.S.A.

Jean-Claude Verite
Electricite de France
Clamart, Cedex, FRANCE

Manfred Wurm
FB Technik
Kiel, GERMANY

Accesion For	
NTIS	CRA&I
DTIC	TAB
Unannounced	<input type="checkbox"/>
Justification _____	
By _____	
Distribution /	
Availability Codes	
Dist	Avail and / or Special
A-1	

THE APPLIED COMPUTATIONAL ELECTROMAGNETICS

TABLE OF CONTENTS

Vol. 10 No. 1

March 1995

"The NEC2 Radiation Patterns of Under-Segmented Wire Grid Models of a Fighter Aircraft Compared to Measurements" by O. Givati and A.P.C. Fourie	5
"A Surface Integral Equation Formulation for Low Contrast Scatterers Based on Radiation Currents" by P.M. Goggans and A.W. Glisson	15
"The Measured Equation of Invariance Method Applied to Randomly Rough Surfaces" by J.B. Schneider and S.L. Broschat	19
"WIREGRID: A NEC2 Pre-processor" by C.F. du Toit and D.B. Davidson	31
"A Guide to Implementational Aspects of the Spatial-Domain Integral Equation Analysis of Microstrip Antennas" by L.T. Hildebrand and D.A. McNamara	40
"Performance of a Characteristic-Based, 3-D, Time-Domain Maxwell Equations Solver on the Intel Touchstone Delta" by J.S. Shang, K.C. Hill and D.A. Calahan	52
"On the Applicability of the Biconjugate Gradient FFT Method for the Thin Conducting Plate Problem" by T.V. Tran and A. McCowen	63
Institutional Membership	69
Announcements	
Call for Papers - Special Issue on Advances in the Application of the Method of Moments to Electromagnetic Radiation and Scattering Problems	71
Call for Papers - Special Issue on Applied Mathematics: Meeting the Challenges Presented by Computational Electromagnetics	72
ACES Membership Form	73
Advertising Rates	74
Copy Information	74
Copyright Form	75

© 1995, The Applied Computational Electromagnetics Society

THE NEC2 RADIATION PATTERNS OF UNDER-SEGMENTED WIRE GRID MODELS OF A FIGHTER AIRCRAFT COMPARED TO MEASUREMENTS

O. Givati and APC. Fourie

University of the Witwatersrand, Johannesburg
Private Bag 3, P O WITS 2050, South Africa

ABSTRACT

This paper presents results of a NEC2 method of moments evaluation of VHF/UHF antennas on a wire grid model of a fighter aircraft. The study shows that practically useful radiation patterns results can be obtained when the grid model is considerably under-segmented in aircraft regions which are electrically far removed from the antennas. Normal modelling guide-lines requires approximately 35000 segments for the fighter grid model at 400 MHz; judicious under-segmentation gave useful results using a model comprising 5000 segments. This reduction in segments reduced computer time by a factor of 343 and memory requirements is reduced by a factor of 18. NEC2 radiation patterns are compared to measurements on a 1/10th scale model which was performed in an anechoic chamber compact range.

1 INTRODUCTION

The paper consider a study of radiation patterns from antennas mounted on a fighter aircraft. NEC2 [1] computed radiation patterns are used for subsequent statistical assessment of link performance for the aircraft during typical mission profiles. Wire grids and segments much longer than the recommended [1] 0.1λ were used in areas far removed from the antennas to reduce execution time and memory requirements. Measured results, as well as comparison to more densely segmented numerical models, were used to ensure that these violations of modelling rules still produced useful values. It may be argued that numerical modelling is superfluous when measured results are available, but this is not the case when considering that:

- measurements in only three principle planes were performed and compared to a subset of the computed values; the statistical link analysis requires full three dimensional pattern information which is difficult and time consuming to obtain by measurement.
- traditional engineering normally argues that measurements constitute the more definitive characterization of a system when compared with calculation. This is definitely not always the case with

radiation pattern measurements, especially on scale models, and many electromagnetics engineers can attest to cases where more confidence can be placed on values obtained from calculation or simulation.

The engineer is hence in a difficult position. He has two methods giving two sets of results - both associated with some potentially large errors. On the positive side is the fact that the two sets of results were obtained using two entirely different methods, with appropriate techniques used in both cases to minimize errors. Qualitative agreement will definitely demonstrate the absence of major blunders in both methods, and engineering judgement and cost will dictate which set of results is likely to be more appropriate.

Valid numerical models, for the purpose of subsequent statistical link analysis, are hence those which show qualitative agreement with measured results. Quantitative comparison between the measured and computed radiation patterns is difficult and often misleading, because:

- errors may be large when comparing measured and computed values at specific angles, but such errors may only be due to a slight offset in the position of a radiation pattern null, for instance. Such small angular offsets are not of any concern when performing statistical analysis of communication link performance.
- the existence of significant measurement errors also frustrate efforts to call the deviation from measured values "simulation errors".

It is hence evident that some of the more traditional quantitative measures of agreement between measured and computed results will be less useful and often meaningless. It is indeed left to the reader to assess the presented comparisons between measured and computed results and decide on their worth for a specific application. The most difficult aspect of the comparison, in fact, is the inaccuracies with the measurements themselves; the extent of such inaccuracies can easily be gauged by the deviations from symmetry in certain planes, as well as comparing corresponding points where different planes intersect.

2 SCALE MODEL MEASUREMENTS

A 1/10th scale model of the fighter aircraft was constructed from polystyrene and covered with polymer sheets. The model was then copper-plated to ensure adequate conductivity. The antennas were incorporated into the model by internally guiding coaxial cable to the antenna positions and protruding the inner conductor by 30mm to form monopoles corresponding to the top-fin and bottom-fin antennas respectively.

Radiation pattern measurements in the principle planes (azimuth, side and pitch roll) were then performed on the scale model using a compact range suitable for the frequency range 2GHz-18GHz. The compact range consists of a 25 m x 10 m x 10 m anechoic chamber, calibrated feed antenna, offset parabolic reflector and positioner with three axes of freedom. The range was calibrated using a vertically polarized, standard gain horn in the frequency range 2 GHz-4 GHz. The standard gain antenna was then replaced with the scale model with the mounting bar in the same horizontal position as the standard gain antenna and the middle of the model at the same height as the standard gain antenna. The measurement system hence measured absolute gain in dB relative to an isotropic source (dBi). The only adjustment to the measured dB_i values was to compute the losses in the cable leading from the calibrated connector to the antenna and to subtract these losses from the measurements in order to obtain the actual gain as measured at the antenna port.

The following movements were executed with the positioner to measure the pattern in the three principle aircraft planes (only the position and movements for the top fin antenna are given below; the bottom fin was measured using exact inverse positions and positioner movements):

- Azimuth (yaw) plane: The model was mounted horizontally and upright and simply rotated through 360°.
- Pitch plane: The model was mounted upright and horizontal, facing the receiving antenna. The model was then tilted 90° forward and 90° backwards to produce the measurement points between 0° and 180° in the plots of results. The model was then mounted facing away from the receiving antenna and again tilted 90° towards and 90° away from the receiving antenna to produce the values plotted between 180° through 360°. It is during the extremes of these tilting movements away from the receiving antenna that reflections associated with the

positioner and mounting bar bending (referred to below) were most severe (corresponding to the plotted values at angles 0° and 180°).

- Roll plane: The model was mounted upright and broadside to the receiving antenna (one wing pointing towards the receiving antenna). The model was then tilted 90° towards and 90° away from the receiving antenna to produce one half of the measured points. It was then rotated by 180° and the same movements were repeated to yield the remaining values of measurements. Once again the comments above regarding errors apply with most severe cases for roll plane graph angles 90° and 270°.

It should be noted that only vertically polarized gain was measured, since this is the dominant polarization from both antennas and was also the only polarization of interest when performing link assessments. The signal source for measurements was also linked to the scale model via a cable which was always routed along the body of the scaled model to ensure that the cable enters the model at the opposite side of the model in relation to the antenna position (model mounting upright and upside down was possible using the mounting arrangement to facilitate this aim). When HF measurements on scale models were performed in the past, a stand alone source was constructed and housed inside the scale model fuselage, because at lower frequencies the aircraft electrical dimensions are small in terms of wavelengths, and the cable shield carries substantial currents which affect the measurements. At higher frequencies, however, the interaction between an antenna mounted on one side of the aircraft with the measurement cable on the opposite side is minimal. A stand alone signal source would have been a disadvantage, in the VHF/UHF case where one is interested in absolute gain values, because it would need to be custom designed with suitable calibrated characteristics.

No measurements are error-free, and measurement uncertainty is particularly difficult to ascertain when radiation patterns are measured. Using the described measurement set-up the following factors may have been the cause of some of the errors (these are more or less listed in order of their severity):

- Inaccuracies in the scale model finish and dimensions. Some of the results presented shows some signs of asymmetry which is most likely due to slight errors in curvature on either side of the antenna

- Interaction between the model and the positioner. These are most severe when the model is tilted backwards (away from the source) during roll and pitch plane measurements. This interaction manifests itself most prominently when one observes the errors in the measurements at the angles where the measured values do not coincide. (Note the 90° and 270° measurements in roll plane and the 0° and 180° points during pitch plane measurements).
- Angular errors due to a certain amount of bending in the perspex mounting bar when the model was tilted for roll and pitch plane measurements. Once again most severe for the 90° and 270° measurements in roll plane and the 0° and 180° points during pitch plane measurements.
- Rotation "wobbles" because the mount in the fuselage is not absolutely perpendicular to the fuselage horizontal datum line.
- Errors due to the fact that the protruding monopoles were not always exactly straight. This manifests itself most commonly in terms of errors in the position of the natural monopole pattern nulls.

No significant errors were caused by source amplitude instability, reflections from the chamber walls and other systematic errors associated with the range. The compact range used is professionally constructed and designed for measurements in the frequency range of interest. The calibration procedure ensures that equipment error levels are accounted for, and the quiet zone associated with the measurements is larger than the maximum movement and model dimensions during the course of the measurement manoeuvres.

3 GENERATION OF THE NUMERICAL MODELS

In this section, representations of the aircraft grid models, used for the evaluation of the top and bottom fin antennas' performance, are shown in Fig. 4 and 6. Different grid models were constructed in order to evaluate the antennas' performances at different frequencies. The numerical model uses symmetry, and therefore only half of each representative grid model is displayed. The two halves are connected at the aircraft axis of symmetry, where the segments are seen to be terminated.

The numerical models of the aircraft were constructed using the Structure Interpolation and Gridding software package, SIG [2], developed by EM-Simulations (Pty) Ltd. The SIG package generates a three-dimensional grid model from a set of user defined cross-sectional cuts at points of abrupt change along the three dimensional structure - as indicated in Fig. 3. The user-defined cross-sections shown in Fig. 3 form the basis for the grid models, shown in Figs. 4 and 5. Wings and other features attached to the main fuselage are accommodated, using the SIG package, by tagging curves which represents features in a user defined cross section and using corresponding tag numbers in later user defined cross sections. In this way, for instance, cross-section 11 in Fig. 3 consists of 3 curves with three tag numbers: The first curve represents the main fuselage, the second the top extension of the cockpit and the last curve in that cross section will just be a single point representing the start of the wing. In the next cross section (12 in Fig. 3) these three curves are re-defined with the dimensions at that cross sectional point and the curve which was tagged as the wing will in this case be a line; interpolation between the single point curve in cross section 11 and the line in cross section 12 defines the characteristic delta wing of this fighter aircraft. The ability of SIG to accommodate appendages to a fuselage in this fashion is exceedingly useful, because the gridding routine ensures that the attached features are connected at all points of the grid.

The grid models shown in Figs. 4 and 5 are generated by interpolating the cross-sectional cuts between the user defined cross-sections (in Fig. 3), at intervals which are not greater than the specified target segment lengths of the user-defined cross-sections. The segmentations produced by SIG are mainly quadrilaterals, with the side lengths approximately equal to the target segment lengths requested. Some triangular grid elements are also formed when curves expand or contract from one cross-section to the next (eg. wings regions). These triangular grid elements also have edge lengths approximately equal to the required segment length. The segment radii are calculated by the SIG package to ensure that the surface area of the segments comprising the grid is approximately twice the surface area of the structure which is modelled. Also note that SIG automatically generated segments abutting the symmetry plane which are only half the grid length to ensure grid size continuity across the symmetry plane.

The SIG program allows the user to specify a specific target segment length for every user defined cross section. This target segment length is then used until a new target length is specified in a subsequent user defined cross section. This SIG feature allowed the variable segmentation (and hence grid size) used during this study.

The use of segment lengths larger than 0.1λ significantly reduces the number of segments used in the numerical model. Generally, such a violation of the numerical modelling rules can result in an invalid numerical model. In this paper, we show that the effect of under-segmentation, in regions which are sufficiently removed from the antennas, is negligible on electrically large structures. In return, the reduction in computation time is significantly large. The effect of under-segmentation can be seen in Fig. 1 and 2, where the radiation patterns of the top-fin antenna on two different 120MHz grid models is simulated according to the segmentation schemes indicated in Table 1.

Section No. (Fig. 3)	Target segment length (120MHz)	Target segment length (120MHz)	Target segment length (220MHz)	Target segment length (300MHz)	Target segment length (400MHz)
1	0.15λ	0.25λ	0.12λ	0.18λ	0.24λ
2	0.15λ	0.25λ	0.12λ	0.18λ	0.24λ
3	0.15λ	0.25λ	0.12λ	0.18λ	0.24λ
4	0.15λ	0.25λ	0.12λ	0.15λ	0.20λ
5	0.15λ	0.25λ	0.10λ	0.12λ	0.16λ
6	0.15λ	0.25λ	0.10λ	0.10λ	0.13λ
7	0.15λ	0.25λ	0.12λ	0.16λ	0.21λ
8	0.15λ	0.25λ	0.18λ	0.22λ	0.29λ
9	0.15λ	0.25λ	0.18λ	0.22λ	0.29λ
10	0.15λ	0.25λ	0.20λ	0.24λ	0.32λ
11	0.15λ	0.25λ	0.20λ	0.24λ	0.32λ
12	0.15λ	0.25λ	0.18λ	0.25λ	0.33λ
13	0.10λ	0.10λ	0.16λ	0.22λ	0.29λ
14	0.10λ	0.10λ	0.10λ	0.13λ	0.17λ
15	0.10λ	0.10λ	0.10λ	0.10λ	0.13λ
16	0.10λ	0.10λ	0.10λ	0.15λ	0.2λ
17	0.10λ	0.10λ	0.10λ	0.15λ	0.2λ
Total No. of segment	1936	1092	4502	4982	4982

Table 1: The segmentation schemes used to generate the grid model of the aircraft at 120MHz, 220MHz, 300MHz and 400MHz.

The segmentation schemes used to generate the numerical models of the aircraft at 220MHz, 300MHz, and 400MHz, and for which theoretical results are presented in this paper, are indicated in Table 1. The total number of segments used to numerically model the aircraft in its entirety (as indicated in Table 1) are much reduced compared to that which would be required if target segments length of 0.1λ were used. Specifying a target segment length of 0.1λ would result in approximately 11400 segments for the 220MHz grid model, 20000 segments for the 300MHz grid model and 35300 segments for the 400MHz grid model.

4 PREDICTED AND MEASURED RESULTS

Appreciating the electrical size and geometrical complexity of the aircraft model, the numerically predicted radiation patterns are compared with the measured radiation patterns in Fig. 6 to Fig. 23. A close examination of the measured results reveal that while the aircraft is symmetrical, the measured patterns shows some asymmetry. In addition, at angles where two measurements were taken, repeatability errors are noted; the discussion in Section 2 gave the reasons for these asymmetry and repeatability errors. Mostly these repeatability errors are noted at points where the model was tilted backwards and the positioner interaction as well as some bending of the perspex mount caused measurement errors. Although comparison of patterns in terms of normalized values, as presented in [3, 4 and 5], are based on pattern integration on a complete volumetric data set, including both polarizations for both measured and computed patterns, the comparison between measured and theoretical results in this paper is shown in terms of absolute gains which are associated with the dominant polarization. The predicted results obtained for the lower frequencies numerical models exhibit better qualitative agreement with measured results because:

- electrically smaller size of the overall problem tends to result in simpler pattern shapes with fewer main lobes and nulls.
- they differ in their segmentation schemes (as shown in Table 1) and generally have segmentation closer to that which is required by the NEC2 modelling guide-lines [1].
- they are generally speaking less prone to numerical errors due to the smaller problem size.

The 400 MHz cases (Figs. 18 to 23) shows some cases where agreement between measurements and NEC2 results are poor, mainly due to extreme under-segmentation (0.33λ for some portions) and probably represents the limit to which this technique can be stretched. For the purpose of statistical link analysis these results were still useful, but they may be unsuitable for some more demanding evaluations.

5 CONCLUSION

The main conclusions and recommendations of this study are listed below:

- Under-segmentation of the aircraft geometry in areas removed from the antennas made the evaluation of antennas at UHF frequencies possible; without this technique most available computer resources will be inadequate for such an evaluation.
- Limited measurements (with some significant errors in some cases) proved useful in qualitatively assessing the merit of the computed results.
- Measured results can be considerably improved by changing the mounting method on scale models such that only azimuth rotation is required. This can be achieved by providing side mounts as well as front and back mounts for pitch and roll plane measurements respectively. This technique was used during subsequent studies with different aircraft and eliminated the problem of repeatable results for the same measurements points (at 0° and 360° , for instance).
- The SIG program [2] proved to be very useful for automatic grid generation of the aircraft. Particularly due to the ability to vary grid size, handle symmetry and generate grid models for different frequencies.

REFERENCES

- [1] Burke, G.J. and Poggio, A.J. (1981) "Numerical Electromagnetics Code (NEC) - Method of Moments", Naval Oceans Systems Centre, San Diego, C.A., 92152. Technical Document 116, Vol. 1.
- [2] Structure Interpolation and Gridding (SIG) software package developed by EM-Simulations (Pty) Ltd, P O Box 1380, Pinegowrie, 2123, South Africa.
- [3] Kubina, S.J. (1983) "Numerical Modelling Methods for Predicting Antenna Performance on Aircraft", AGARD Lecture Series No. 131, Sept. 1983, pp 9-1 to 9-38.
- [4] Peng, J., Balanis, C.A. and Britcher, C.R. (1993) "Improvement of the NEC Code's Upper Limit and Pattern Prediction of a Helicopter Structure", IEEE Antennas and Propagation Society International Symposium, University of Michigan, Ann Arbor, Michigan, USA., June 28 - July 2, 1993, Vol. 1., pp 56-59.
- [5] Peng, J., Choi, J., and Balanis, C.A. (1991) "Progress: Development of an interactive graphics program for EM codes" 7th Annual Review of Progress in Applied Computational Electromagnetics at Naval Postgraduate School Monterey, CA., March 1991, pp 10-19.

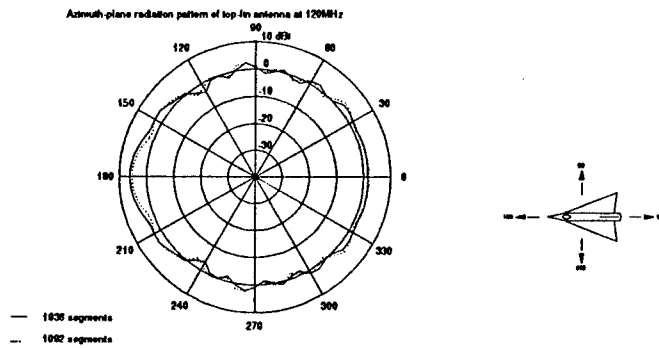


Figure 1: Theoretical azimuth-plane radiation patterns of the Top-Fin antenna at 120MHz as obtained by NEC2 for two different grid models of the fighter aircraft. Both numerical models use 0.10λ segment lengths in the vicinity of the Top-Fin antenna. In the regions which are sufficiently removed from the Top-Fin antenna, the one model uses 0.15λ segment lengths while the other model uses 0.25λ segment lengths.

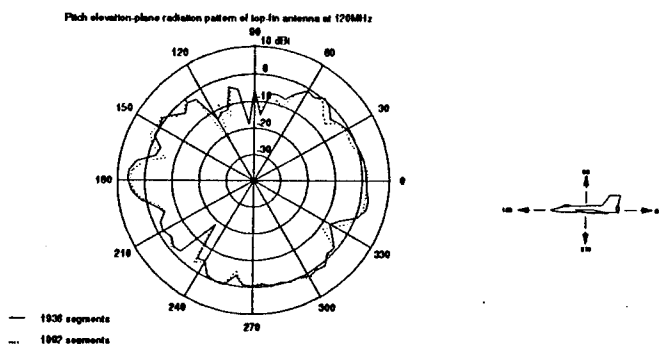


Figure 2: Theoretical pitch elevation-plane radiation patterns of the Top-Fin antenna at 120MHz as obtained by NEC2 for two different grid models of the fighter aircraft. Both numerical models use 0.10λ segment lengths in the vicinity of the Top-Fin antenna. In the regions which are sufficiently removed from the Top-Fin antenna, the one model uses 0.15λ segment lengths while the other model uses 0.25λ segment lengths.

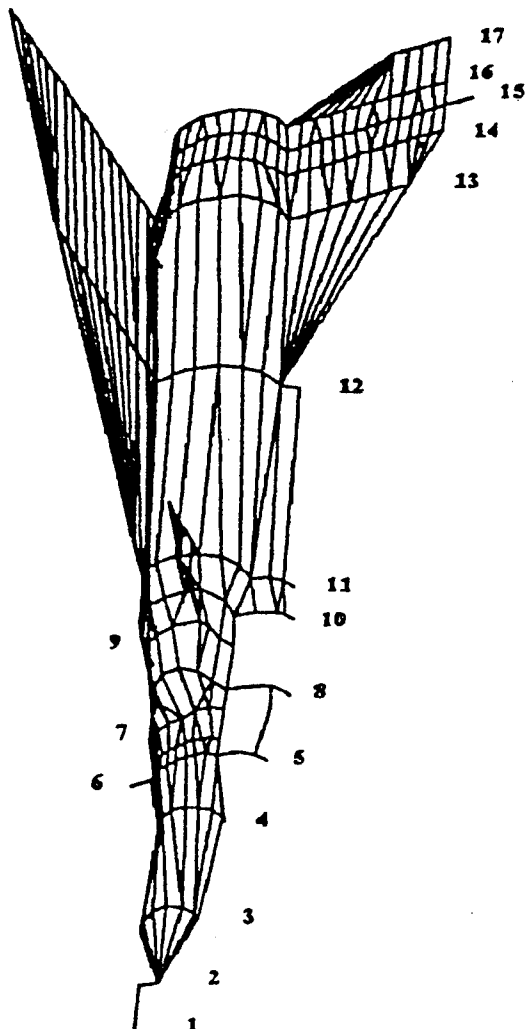


Figure 3: The user defined cross-sections used to generate the grid model of the fighter aircraft (The longitudinal lines shown in this figure are just for ease of visualizing the structure and to give an indication of the linear interpolation between the cross sections).

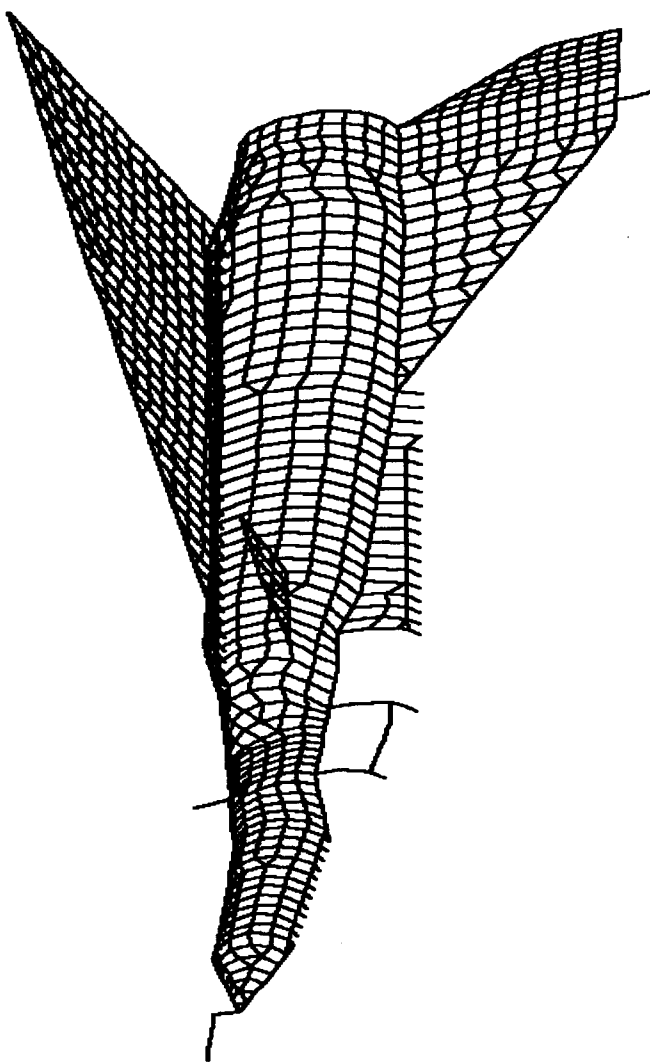


Figure 4: The grid model of the fighter aircraft at 220MHz. Since symmetry is used for simulations, only half of the grid model is displayed. The two halves are connected at the aircraft axis of symmetry where segments are seemed to be terminated. This numerical model comprises of 4502 segments with the shortest segment lengths being 0.10λ (in the vicinity of the antennas) and the longest segment lengths being 0.20λ (in a region removed from the antennas).

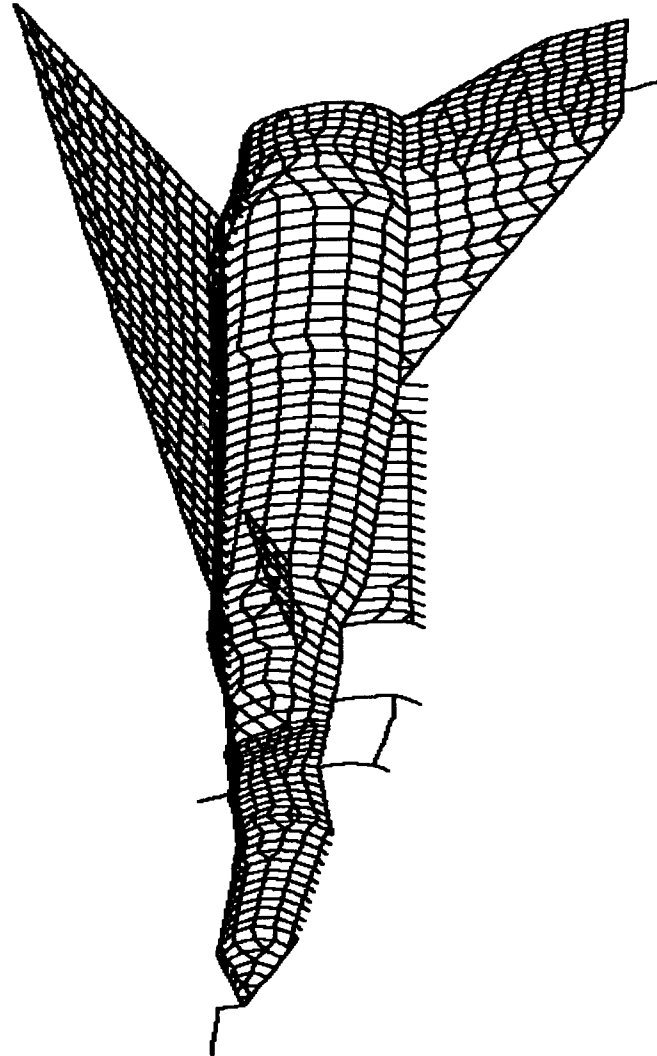


Figure 5: The grid model of the fighter aircraft at 300MHz. Since symmetry is used for simulations, only half of the grid model is displayed. The two halves are connected at the aircraft axis of symmetry where segments are seemed to be terminated. This numerical model comprises of 4982 segments with the shortest segment lengths being 0.10λ (in the vicinity of the antennas) and the longest segment lengths being 0.25λ (in a region removed from the antennas).

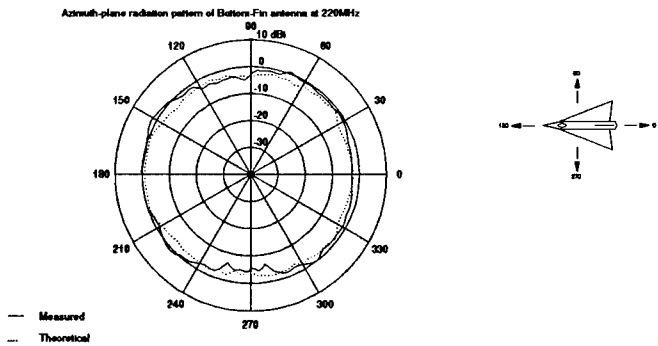


Figure 6: Measured and theoretical azimuth radiation patterns of the Bottom-Fin antenna at 220MHz. The numerical model comprises of 4502 segments with the shortest and longest segment lengths being 0.10λ and 0.20λ respectively.

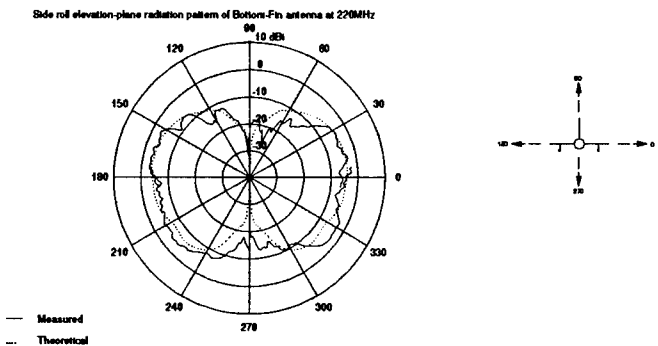


Figure 7: Measured and theoretical side roll elevation-plane radiation patterns of the Bottom-Fin antenna at 220MHz. The numerical model comprises of 4502 segments with the shortest and longest segment lengths being 0.10λ and 0.20λ respectively.

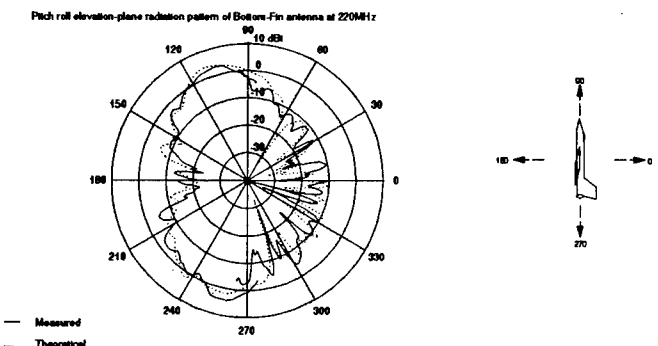


Figure 8: Measured and theoretical pitch roll elevation-plane radiation patterns of the Bottom-Fin antenna at 220MHz. The numerical model comprises of 4502 segments with the shortest and longest segment lengths being 0.10λ and 0.20λ respectively.

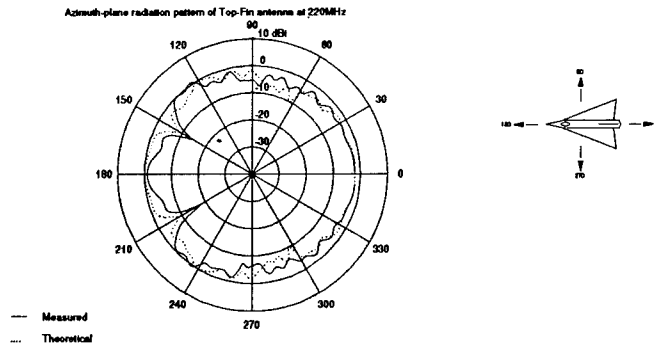


Figure 9: Measured and theoretical azimuth radiation patterns of the Top-Fin antenna at 220MHz. The numerical model comprises of 4502 segments with the shortest and longest segment lengths being 0.10λ and 0.20λ respectively.

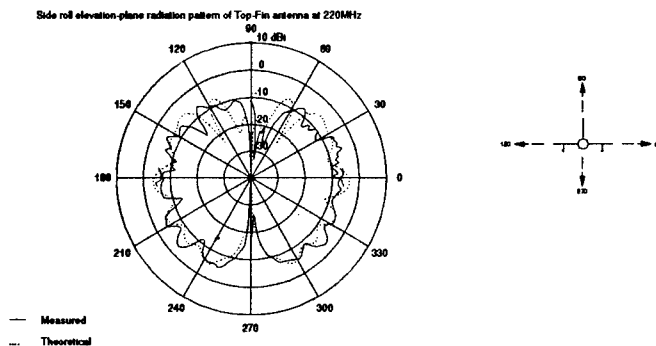


Figure 10: Measured and theoretical side roll elevation-plane radiation patterns of the Top-Fin antenna at 220MHz. The numerical model comprises of 4502 segments with the shortest and longest segment lengths being 0.10λ and 0.20λ respectively.

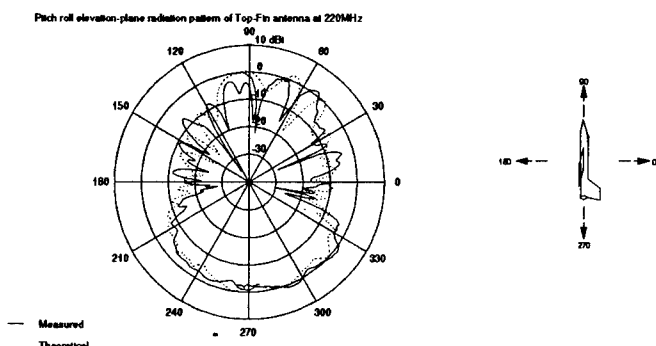


Figure 11: Measured and theoretical pitch roll elevation-plane radiation patterns of the Top-Fin antenna at 220MHz. The numerical model comprises of 4502 segments with the shortest and longest segment lengths being 0.10λ and 0.20λ respectively.

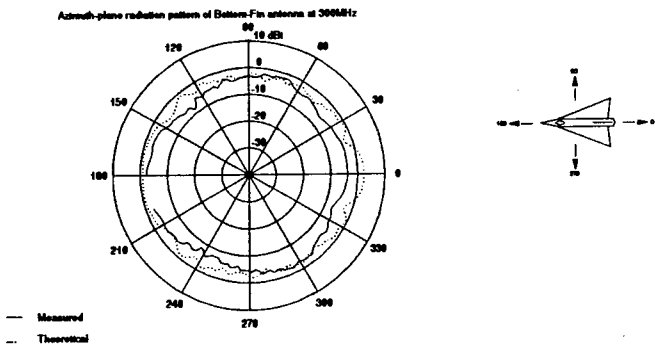


Figure 12: Measured and theoretical azimuth radiation patterns of the Bottom-Fin antenna at 300MHz. The numerical model comprises of 4982 segments with the shortest and longest segment lengths being 0.10λ and 0.25λ respectively.

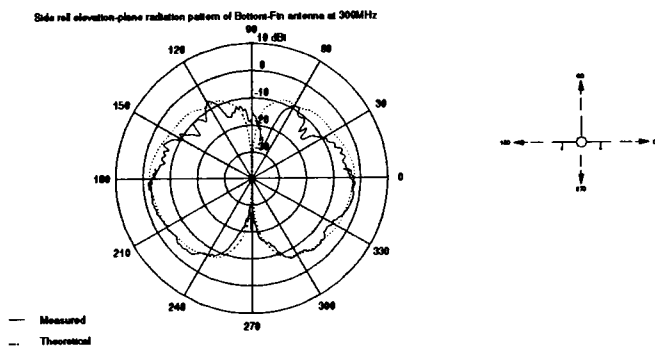


Figure 13: Measured and theoretical side roll elevation-plane radiation patterns of the Bottom-Fin antenna at 300MHz. The numerical model comprises of 4982 segments with the shortest and longest segment lengths being 0.10λ and 0.25λ respectively.

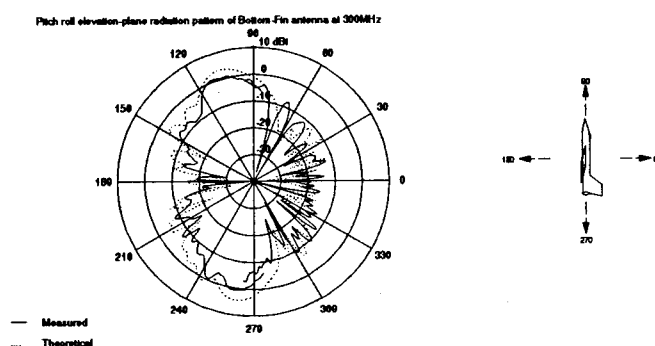


Figure 14: Measured and theoretical pitch roll elevation-plane radiation patterns of the Bottom-Fin antenna at 300MHz. The numerical model comprises of 4982 segments with the shortest and longest segment lengths being 0.10λ and 0.25λ respectively.

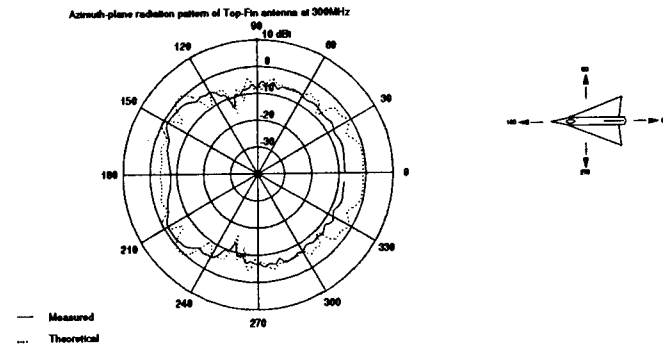


Figure 15: Measured and theoretical azimuth radiation patterns of the Top-Fin antenna at 300MHz. The numerical model comprises of 4982 segments with the shortest and longest segment lengths being 0.10λ and 0.25λ respectively.

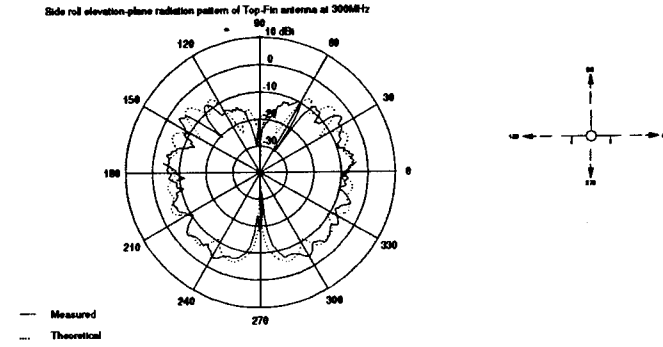


Figure 16: Measured and theoretical side roll elevation-plane radiation patterns of the Top-Fin antenna at 300MHz. The numerical model comprises of 4982 segments with the shortest and longest segment lengths being 0.10λ and 0.25λ respectively.

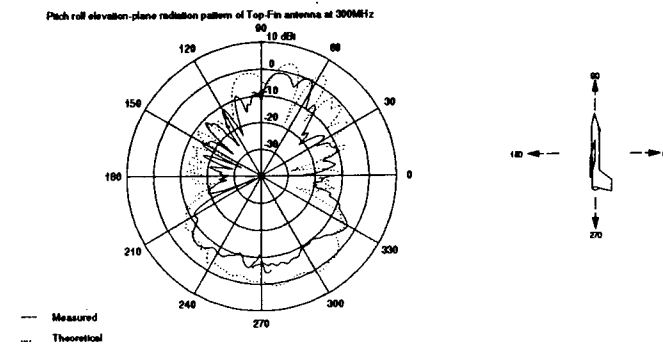


Figure 17: Measured and theoretical pitch roll elevation-plane radiation patterns of the Top-Fin antenna at 300MHz. The numerical model comprises of 4982 segments with the shortest and longest segment lengths being 0.10λ and 0.25λ respectively.

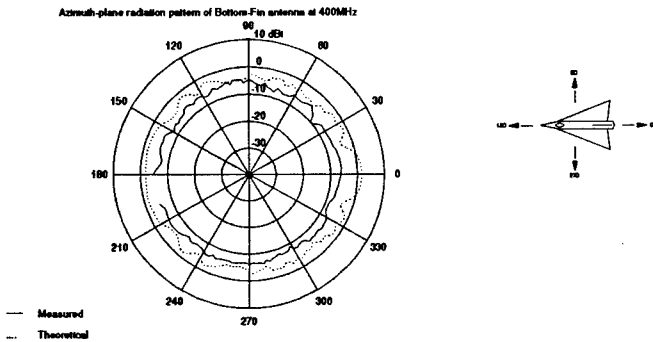


Figure 18: Measured and theoretical azimuth radiation patterns of the Bottom-Fin antenna at 400MHz. The numerical model comprises of 4982 segments with the shortest and longest segment lengths being 0.13λ and 0.33λ respectively.

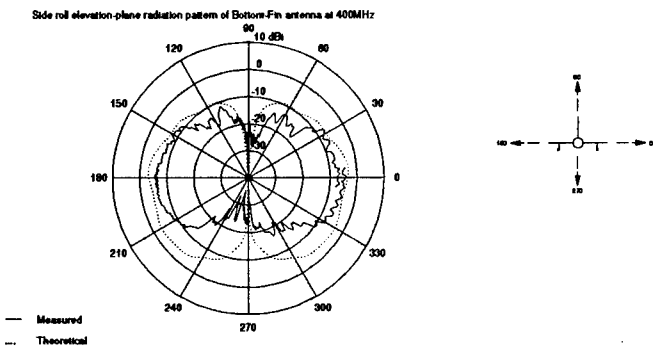


Figure 19: Measured and theoretical side roll elevation-plane radiation patterns of the Bottom-Fin antenna at 400MHz. The numerical model comprises of 4982 segments with the shortest and longest segment lengths being 0.13λ and 0.33λ respectively.

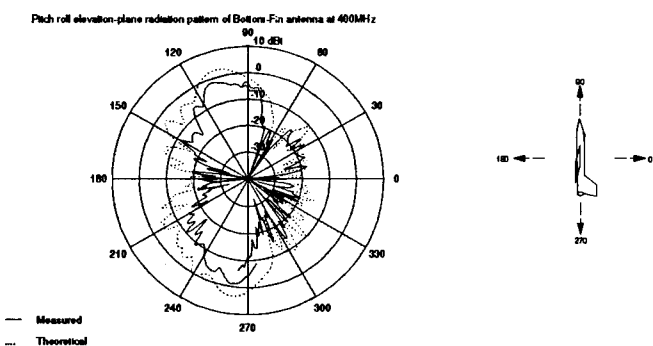


Figure 20: Measured and theoretical pitch roll elevation-plane radiation patterns of the Bottom-Fin antenna at 400MHz. The numerical model comprises of 4982 segments with the shortest and longest segment lengths being 0.13λ and 0.33λ respectively.

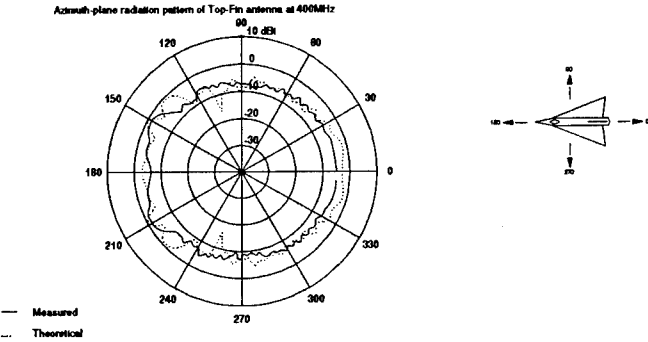


Figure 21: Measured and theoretical azimuth radiation patterns of the Top-Fin antenna at 400MHz. The numerical model comprises of 4982 segments with the shortest and longest segment lengths being 0.13λ and 0.33λ respectively.

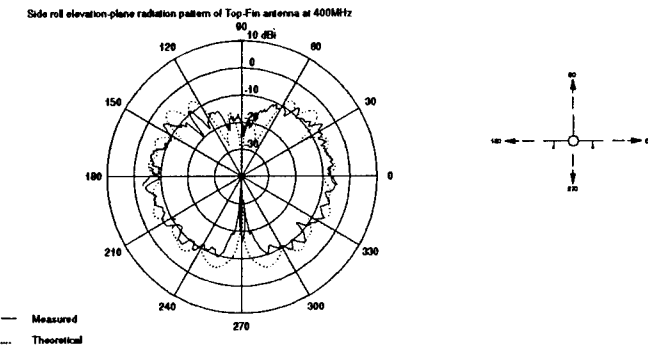


Figure 22: Measured and theoretical side roll elevation-plane radiation patterns of the Top-Fin antenna at 400MHz. The numerical model comprises of 4982 segments with the shortest and longest segment lengths being 0.13λ and 0.33λ respectively.

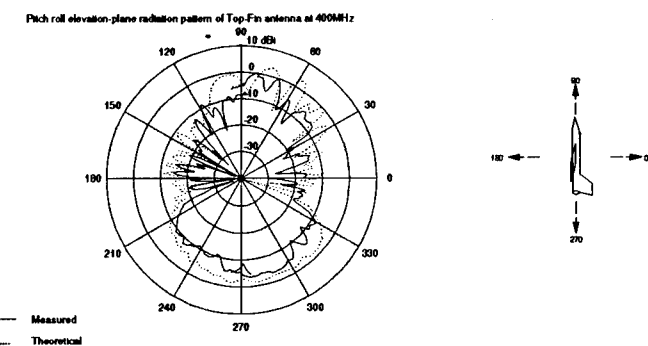


Figure 23: Measured and theoretical pitch roll elevation-plane radiation patterns of the Top-Fin antenna at 400MHz. The numerical model comprises of 4982 segments with the shortest and longest segment lengths being 0.13λ and 0.33λ respectively.

A SURFACE INTEGRAL EQUATION FORMULATION FOR LOW CONTRAST SCATTERERS BASED ON RADIATION CURRENTS

Paul M. Goggans and Allen W. Glisson

Department of Electrical Engineering, University of Mississippi
University, MS 38677

Abstract - A new surface integral equation formulation based on radiation currents is presented. Numerical problems have been observed when treating low contrast scatterers with surface integral equation formulations based on the total equivalent currents. These problems result because the total equivalent currents are large compared with the radiation currents for low contrast materials. The surface integral equation formulation presented here avoids this problem by solving directly for the radiation currents.

I. INTRODUCTION

This paper presents a new surface integral equation formulation for determining the electromagnetic field scattered by objects with low contrast. Low contrast materials are characterized by a relative permittivity and relative permeability close to unity. Low contrast materials include compressed gases and commonly used plastic foams.

When used in conjunction with a numerical integral equation solution, the conventional surface integral equation formulations can result in a poor estimate of the field scattered by a low contrast object. The poor performance of the standard formulations is due to their being cast in terms of the total equivalent current on the boundary surface of the scattering body. Only a portion of the total equivalent current gives rise to the scattered field. When this portion is small (as in the case of low contrast scatterers), errors in the radar cross section (RCS) calculation can occur. The new integral equation formulation is cast only in terms of the portion of the total current that gives rise to the scattered field; hence, the new formulation avoids this problem.

Here the new integral equation formulation is implemented in a moment method (MM) program for two-dimensional objects. Results of the numerical method are verified by comparison with series solution results for circular cylindrical objects.

II. THE SURFACE INTEGRAL EQUATIONS

Consider a closed dielectric scatterer in free space with surface A and illuminated by source currents in the free space region. For a common choice of the combination constants a set of combined field integral equations [1,2] for this scatterer may be written succinctly as

$$-\left[\mathbf{E}_{\text{tan}}^+(\mathbf{J}) + \mathbf{E}_{\text{tan}}^+(\mathbf{M}) \right] \frac{1}{\eta_0} - \hat{\mathbf{n}} \times \left[\mathbf{H}^+(\mathbf{J}) + \mathbf{H}^+(\mathbf{M}) \right] = \mathbf{E}_{\text{tan}}^+(\mathbf{J}^i, \mathbf{M}^i) / \eta_0 + \hat{\mathbf{n}} \times \mathbf{H}^+(\mathbf{J}^i, \mathbf{M}^i) \quad (1)$$

just inside A

$$-\left[\mathbf{E}_{\text{tan}}^-(\mathbf{J}) + \mathbf{E}_{\text{tan}}^-(\mathbf{M}) \right] \frac{1}{\eta_0} + \hat{\mathbf{n}} \times \left[\mathbf{H}^-(\mathbf{J}) + \mathbf{H}^-(\mathbf{M}) \right] = 0. \quad (2)$$

just outside A

The following definitions are made with respect to (1) and (2):

A	- Dielectric/free space boundary
\mathbf{J}, \mathbf{M}	- Equivalent electric and magnetic surface currents on A
$\mathbf{J}^i, \mathbf{M}^i$	- Source currents of the incident wave
$\hat{\mathbf{n}}$	- Outward surface normal on A
$\mathbf{E}^+, \mathbf{H}^+$	- Electric and magnetic fields calculated in an infinite homogeneous free space region
$\mathbf{E}^-, \mathbf{H}^-$	- Electric and magnetic fields calculated in an infinite homogeneous region with constitutive parameters of the dielectric
η_0	- Characteristic impedance of free space

The tangential portion of the electric field on A is determined using the expression

$$\mathbf{E}_{\text{tan}} = -\hat{\mathbf{n}} \times \hat{\mathbf{n}} \times \mathbf{E} \quad (3)$$

Equation (1) corresponds to the exterior equivalent situation where the scatterer is replaced with free space and the equivalent surface currents radiate the scattered field

outside the boundary of the scatterer and the negative of the incident fields inside the scatterer. Equation (2) corresponds to the interior equivalent situation where the free space region is replaced with dielectric and the negative of the equivalent surface currents radiate zero fields in the exterior region and the same fields as in the original scattering problem in the interior region.

The total equivalent surface currents can be partitioned into scattering (radiation) currents and incident currents as follows:

$$\begin{aligned} \mathbf{J} &= \mathbf{J}^* + \mathbf{J}^{\circ} \\ \mathbf{M} &= \mathbf{M}^* + \mathbf{M}^{\circ} \end{aligned} \quad (4)$$

where

$$\mathbf{J}^{\circ} = \hat{\mathbf{n}} \times \mathbf{H}^+ (\mathbf{J}^i, \mathbf{M}^i) \quad (5)$$

and

$$\mathbf{M}^{\circ} = -\hat{\mathbf{n}} \times \mathbf{E}^+ (\mathbf{J}^i, \mathbf{M}^i). \quad (6)$$

The incident currents \mathbf{J}° and \mathbf{M}° are the total equivalent surface currents for a free space or "phantom" dielectric scatterer. Thus, the incident currents must radiate zero scattered field in the exterior region of the exterior equivalent problem. Clearly, for an actual dielectric scatterer, the scattering currents alone produce the total scattered field in the exterior equivalent problem.

Substituting (4) into (1) and making use of the linearity of the electric and magnetic field operators to manipulating the result yields:

$$\begin{aligned} -[\mathbf{E}_{\tan}^+ (\mathbf{J}^*) + \mathbf{E}_{\tan}^+ (\mathbf{M}^*)] \frac{1}{\eta_0} - \hat{\mathbf{n}} \times [\mathbf{H}^+ (\mathbf{J}^*) + \mathbf{H}^+ (\mathbf{M}^*)] = \\ [\mathbf{E}_{\tan}^+ (\mathbf{J}^i, \mathbf{M}^i) + \mathbf{E}_{\tan}^+ (\mathbf{J}^{\circ}, \mathbf{M}^{\circ})] \frac{1}{\eta_0} \\ + \hat{\mathbf{n}} \times [\mathbf{H}^+ (\mathbf{J}^i, \mathbf{M}^i) + \mathbf{H}^+ (\mathbf{J}^{\circ}, \mathbf{M}^{\circ})] \end{aligned} \quad (7)$$

just inside A

Because the "incident currents" produce the negative of the incident fields in the interior region of the exterior equivalent problem (7) can be reduced to

$$\begin{aligned} -[\mathbf{E}_{\tan}^+ (\mathbf{J}^*) + \mathbf{E}_{\tan}^+ (\mathbf{M}^*)] \frac{1}{\eta_0} - \hat{\mathbf{n}} \times [\mathbf{H}^+ (\mathbf{J}^*) + \mathbf{H}^+ (\mathbf{M}^*)] \\ = 0. \quad (8) \end{aligned}$$

just inside A

Equation (8) is a statement of the fact that the scattering currents must radiate zero fields in the interior of the exterior scattering problem. Substituting (4) into (2) yields:

$$\begin{aligned} -[\mathbf{E}_{\tan}^- (\mathbf{J}^*) + \mathbf{E}_{\tan}^- (\mathbf{M}^*)] \frac{1}{\eta_0} + \hat{\mathbf{n}} \times [\mathbf{H}^- (\mathbf{J}^*) + \mathbf{H}^- (\mathbf{M}^*)] = \\ [\mathbf{E}_{\tan}^- (\mathbf{J}^{\circ}) + \mathbf{E}_{\tan}^- (\mathbf{M}^{\circ})] \frac{1}{\eta_0} - \hat{\mathbf{n}} \times [\mathbf{H}^- (\mathbf{J}^{\circ}) + \mathbf{H}^- (\mathbf{M}^{\circ})] \quad (9) \end{aligned}$$

just outside A

Equations (8) and (9) are a set of coupled integral equations which can be solved for the scattering currents directly. In this new integral equation formulation the excitation is moved from the exterior region to the interior region. The excitation in the new formulation is dependent on the material parameters of the scatterer. For a "phantom" dielectric scatterer, the right hand side of (9) (the excitation) is zero so that the scattering currents are identically zero.

The radiation current integral equation formulation presented here is developed from the conventional combined field integral equation (CFIE) formulation. A similar radiation current integral equation formulation can also be obtained for the PMCHW [2,3] formulation by following the same steps. The radiation current integral equation formulation is also easily extended to the multiple dielectric scatterer case.

III. NUMERICAL RESULTS

To demonstrate the radiation current integral equation formulation it was implemented in a two-dimensional moment method program [4]. For this program (8) and (9) were specialized to the transverse magnetic (TM) and transverse electric (TE) polarization cases. The 2-D MM program used a piecewise linear approximation to the contour of the scatterer and pulse current expansion with point matching. Segments of the piecewise linear representation of the scatterer are referred to as zones.

Because the program originally used the conventional CFIE there was no need to change the calculation of the MM impedance matrix when implementing the new formulation (note that the operator forms on the left sides of (1) and (2) are identical to those on the left sides of (8) and (9)). Only the calculation of the excitation required modification. Accurate calculation of the excitation is critical to the success of the method. On linear zones the incident currents \mathbf{J}° and \mathbf{M}° have constant magnitude and linear phase for an incident plane wave. If the excitation in (9) is calculated using the existing

impedance elements (which assume constant magnitude and constant phase) it was observed that the radiation current based formulation yields no better results than the conventional formulation when treating low contrast scatterers. This observation is true for both the TE and TM cases. To achieve accurate results, the phase variation of the incident currents on each zone must be incorporated in the calculation of the excitation. The best approach is to derive new impedance elements which incorporate the linear phase variation of the incident currents. An alternative numerical approximation is to subdivide each linear zone into an odd number of subzones to more accurately model the phase variation of the incident currents. In this approach the field at the match point of the center subzone of each zone is calculated using the existing impedance elements (not the ones in the MM matrix but ones for each subzone calculated with the same routines). The use of an odd number of subzones is required so that match point of the center subzone will be the same as the match point of the entire zone. The former approach is more accurate and requires less computation. The latter approach, however, has the advantage of not being limited to plane wave excitation. For expedience, the latter approach was taken here with each zone being divided into eleven subzones for the calculation of the excitation.

Figure 1 compares the bistatic RCS of a low contrast dielectric cylinder calculated using the conventional formulation with those calculated using the radiation current formulation. Also plotted in Fig. 1 are series solution results. The radius of the cylinder is one free space wavelength, λ_0 . The dielectric constant of the cylinder is 1.01. The MM program is written in FORTRAN and uses single precision floating point numbers. For both numerical solutions the cylinder was divided into 100 linear zones. The plane wave was incident from $\phi = 180^\circ$. In Fig. 1 the RCS, σ , is normalized by λ_0 . Figure 1a is for a TM polarized incident wave and Fig. 1b is for a TE polarized incident wave. Figure 1 demonstrates the error in the calculated RCS which can occur when treating low contrast scatterers using the conventional formulation.

Figure 2 compares the magnitude of the normalized electric and magnetic scattering current for the case of Fig. 1b (TE polarization). Series solution results are also given. Figure 2a plots the electric current and Fig. 2b plots the magnetic current. The electric current is normalized by the incident magnetic field and the magnetic current is normalized by the incident electric field. Because the conventional formulation calculates the total equivalent currents, the scattered currents in Fig. 2 for the conventional formulation were determined by subtracting the incident currents from the calculated total currents. The radiation current formulation determines the scattered

currents directly. Figure 2 illustrates that use of the conventional formulation results in errors in the scattering currents for low contrast scatterers. As expected these errors occur at places on the scatterer where the scattering current is small.

IV. CONCLUSIONS

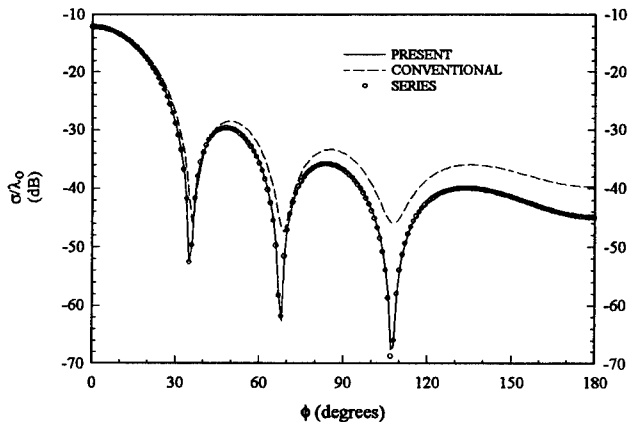
A radiation current based surface integral equation formulation for low contrast scatterers was presented. Numerical results demonstrate the utility and validity of the new formulation.

Although its main application appears to be in treating low contrast scatterers, the radiation current formulation is also useful for accurately determining the equivalent currents on general material bodies in regions of the surface where the radiation currents are small. Note that unlike the most commonly used low-contrast formulation, the Müller formulation [3], the radiation current formulation works for high contrast scatterers as well as low contrast scatterers.

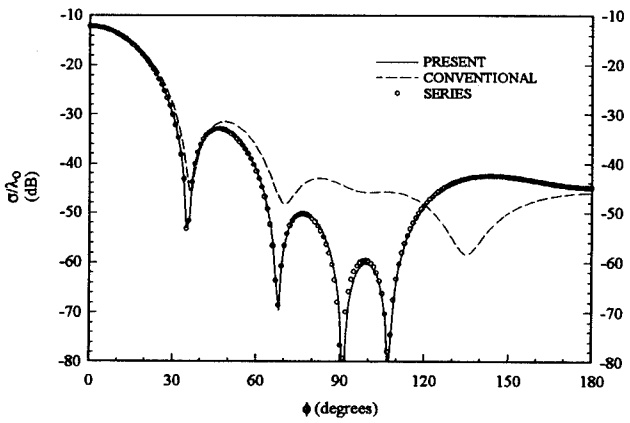
Implementation of the formulation in existing moment method programs is relatively straightforward since the moment matrix is unchanged. Only the excitation vector must be changed.

REFERENCES

- [1] J. R. Mautz and R. F. Harrington, "Boundary formulations for aperture coupling problems," *Arch. Elek. Übertragung*, vol. 34, pp. 377-384, 1980.
- [2] A. A. Kishk and L. Shafai, "On the accuracy limits of different integral equation formulations for numerical solution of dielectric bodies of revolution," *Can. J. Phys.*, vol. 63, pp. 1532-1539, 1985.
- [3] J. R. Mautz and R. F. Harrington, "Electromagnetic scattering from a homogeneous body of revolution," *Arch. Elek. Übertragung*, vol. 32, pp. 71-80, 1979.
- [4] P. M. Goggans and T. H. Shumpert, "CFIE MOM solution for TE and TM incidence on a 2-D conducting body with a dielectric filled cavity," *IEEE Trans. Antennas Propagat.*, vol. AP-38, pp. 1645-1649, October 1990.

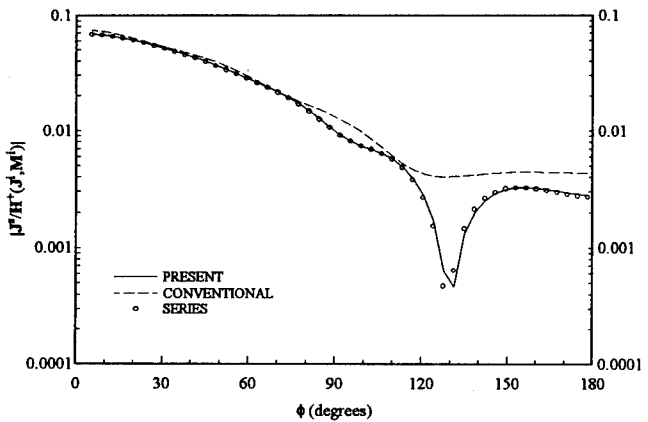


(a) TM polarization

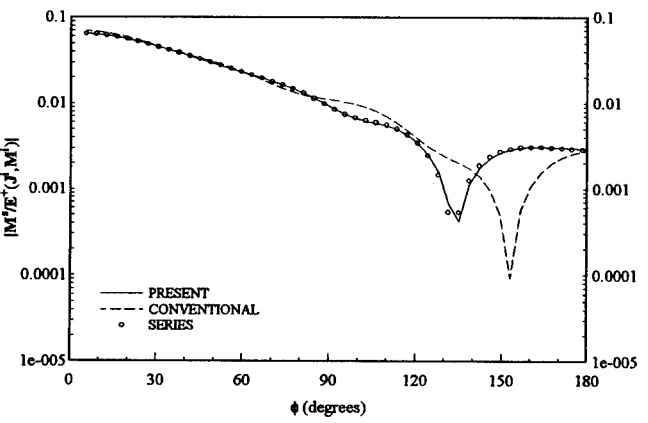


(b) TE polarization

Figure 1. Bistatic RCS of a dielectric cylinder with a radius of one free-space wavelength and a dielectric constant of 1.01. The plane wave is incident from $\phi = 180^\circ$.



(a) Electric current



(b) Magnetic current

Figure 2. Normalized scattering currents on of a dielectric cylinder with a radius of one free-space wavelength and a dielectric constant of 1.01. The TE polarized plane wave is incident from $\phi = 180^\circ$.

The Measured Equation of Invariance Method Applied to Randomly Rough Surfaces

John B. Schneider and Shira Lynn Broschat*

Abstract

The Measured Equation of Invariance (MEI) method has received considerable attention recently. Unlike more traditional numerical techniques, MEI solutions are obtained by inversion of a relatively small *and* sparse matrix. Therefore, the MEI method can potentially provide a solution much more quickly than other techniques. To date, the MEI method has been applied primarily to discrete objects. In this paper, bistatic radar cross sections for one-dimensional, perfectly conducting, randomly rough surfaces are obtained using the MEI method. The implementation suitable for this problem requires some modification and enhancement of the original algorithm to achieve the desired accuracy. These algorithmic changes can be applied to the discrete scattering problem as well. Monte Carlo results for the bistatic scattering cross section for surfaces with Gaussian statistics and satisfying a Gaussian roughness spectrum are compared to those from another technique and excellent agreement is obtained.

I. Introduction

The Measured Equation of Invariance (MEI) method was recently introduced [1, 2, 3, 4] as a way to determine the electromagnetic fields scattered from discrete objects. Initially, results were reported mostly for conducting two-dimensional objects, but the method can be applied much more broadly. Hybrid techniques have been used in conjunction with the MEI method to obtain scattering from penetrable objects [5, 6, 7, 8]; however, many of these scatterers can be analyzed using a simpler scheme if the metrons are selected carefully [2]. Additionally, the

MEI method can be used to provide solutions to Laplace's equation [3, 9].

The principal attraction of the MEI method is that it yields a solution via a sparse and relatively small matrix, and hence requires much less time and memory than more conventional techniques. The computational mesh is terminated very close to the scattering object. Interior mesh points are related to each other using standard finite difference techniques while boundary nodes are handled using the Measured Equations of Invariance. The time required to fill the matrix is roughly $O(N^2)$, where N is the number of unknowns on the boundary. Because the matrix is sparse, the time required to invert the matrix is small ($O(N)$); thus, the total computation time is dominated by the time required to fill the matrix. This is in contrast to the traditional Method of Moments approach which requires the inversion of a full matrix (an $O(N^3)$ operation).

In this paper the MEI method is used to solve for the bistatic radar cross sections for randomly rough surfaces. Specifically, ensemble averaging over a number of surface realizations is used to approximate the results for a single, infinitely long surface. Surfaces with Gaussian statistics and satisfying a Gaussian roughness spectrum are assumed. However, it should be emphasized that this numerical technique is not restricted to this class of surfaces.

In Section II a brief review of the MEI method is provided. The pertinent aspects of the rough surface scattering problem are outlined in Section III. In Section IV our implementation of a MEI-based solution to the problem is described. Finally, results are presented in Section V.

II. Review of the MEI Method

Ultimately, our goal is to solve the wave equation subject to the appropriate boundary conditions. For the

*The authors are with the School of Electrical Engineering and Computer Science, Washington State University, Pullman, WA 99164-2752

sake of concreteness, we assume TM illumination of a perfectly-conducting, two-dimensional scatterer (e.g., a surface for which the height varies as a function of one spatial coordinate) so that the governing differential equation is reduced to a scalar one:

$$(\nabla^2 + k^2)E_z = 0 \quad (1)$$

where k is the wavenumber of the incident field. If space is discretized into a uniform mesh and a local configuration of nodes is as shown in Fig. 1, (1) can be approximated using central differences to obtain

$$-(4 - k^2 \Delta^2)E_{z0} + E_{z1} + E_{z2} + E_{z3} + E_{z4} = 0 \quad (2)$$

where Δ is the separation between mesh points. This can be written more generally as

$$\sum_{i=0}^N \alpha_i E_{zi} = 0, \quad (3)$$

where N is the number of nodes “connected” to the zeroth (central) node and the α_i ’s represent appropriate weights. For a Cartesian structure, such as in Fig. 1, all weights for the surrounding nodes are equal. Had a polar mesh been used, the weights would have to account for the global location within the mesh, i.e., the weights would be a function of the radial distance from the origin. If a higher-order differencing scheme had been used, N would have to be increased. These difference equations are invariant to the location and geometry of the scatterer and to the field of excitation. The appeal of the finite difference formulation is the sparsity and ease of calculating the non-zero elements in the resulting matrix. However, the finite difference approach is problematic in that it provides no simple way to terminate the computational mesh for unbounded problems.

To address this shortcoming, Mei developed the Measured Equation of Invariance (MEI) method that combines features of both differential and integral based methods [4]. Basically, the MEI method provides a means to select appropriate α_i ’s in (3) so that the mesh need not be orthogonal. This allows the fields at the nodes on the edge of the computational domain to be related simply to points in the interior. Furthermore, Mei maintains that the resulting set of equations (and hence the α_i ’s) is location dependent, geometry specific, and invariant to the field of excitation. The MEI method does not seek to find

a strict discretization of the wave equation. Instead, the discretization that is obtained is an approximation to an unknown operator that satisfies both the wave equation and the radiation condition. This is discussed in more detail in [2].

To illustrate the technique, consider the configuration of nodes shown in Fig. 2. These nodes are typical of the mesh at the edge of the computational domain. We seek α_i ’s such that

$$\sum_{i=0}^3 \alpha_i E_{zi} = 0. \quad (4)$$

Since (4) is a homogeneous equation, one of the weights (e.g., α_0) may be chosen arbitrarily. The remaining three weights are determined via three equations. These equations are obtained by assuming independent source distributions, known as metrons, over the surface of the scatterer. Each metron gives rise to a field, known as the measured field, which is easily calculated. The weights are obtained by satisfying (4) for each of the measured fields. Specifically, three metrons are assumed J_s^1 , J_s^2 , and J_s^3 . From these the n th measured field $E_z^n(\mathbf{r})$ is obtained via

$$E_z^n(\mathbf{r}) = \int_S J_s^n(\mathbf{r}') G(\mathbf{r}|\mathbf{r}') ds' \quad (5)$$

where \mathbf{r} is the observation point, \mathbf{r}' is a point on the surface, and $G(\mathbf{r}|\mathbf{r}')$ is the appropriate Green’s function (typically the free space Green’s function). Assuming $\alpha_0 = 1$, the remaining weights are obtained using

$$\begin{bmatrix} \alpha_1 \\ \alpha_2 \\ \alpha_3 \end{bmatrix} = - \begin{bmatrix} E_{z1}^1 & E_{z2}^1 & E_{z3}^1 \\ E_{z1}^2 & E_{z2}^2 & E_{z3}^2 \\ E_{z1}^3 & E_{z2}^3 & E_{z3}^3 \end{bmatrix}^{-1} \cdot \begin{bmatrix} E_{z0}^1 \\ E_{z0}^2 \\ E_{z0}^3 \end{bmatrix} \quad (6)$$

which can be written as

$$\boldsymbol{\alpha} = -\mathbf{M}^{-1} \cdot \mathbf{M}_0 \quad (7)$$

where the matrix \mathbf{M} contains the measured fields at the neighboring nodes while the vector \mathbf{M}_0 contains the fields sampled at the zeroth node.

Although the metrons are chosen to be independent, the sampled values of the measured fields over a small number of mesh points may not be independent. Hence, the matrix \mathbf{M} may be singular and a solution to (7) will not exist. There are several ways to circumvent this problem. Perhaps the easiest is to use more metrons, and subsequently more measured fields, than unknowns. In this

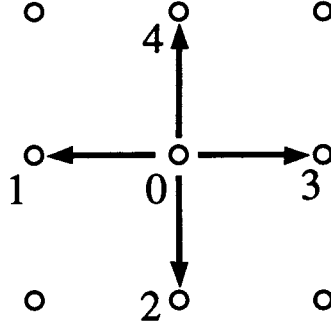


Figure 1: Nodes in the computational mesh.

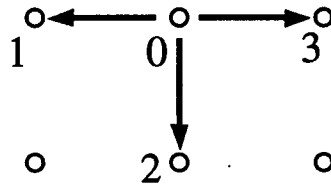


Figure 2: Typical configuration of nodes at the edge of the computational mesh

case, the weights are obtained via least squares so that α is the vector that minimizes $\|\mathbf{M} \cdot \alpha + \mathbf{M}_0\|$. This least squares operation is performed on a small matrix (e.g., in the work presented here \mathbf{M} is 5×3) and thus requires negligible time relative to the calculation of the measured fields.

In principle the MEI method can be used for all nodes within the computational domain. However, this would require careful treatment of the singularity in the integrand of (5) for nodes adjacent to the surface (i.e., at least one neighboring node would be on the surface and the measured field for this node would require careful calculation of (5)). To obviate the consideration of this singularity, a layer of nodes that use standard finite difference coefficients is placed adjacent to the surface. If the mesh is non-orthogonal, but relatively undistorted, Pous has found that weights can be obtained using a local polar approximation [2]. This layer of nodes insures that the measured fields only need to be calculated at points above the surface.

From this point, the MEI method is similar to the finite difference method. The weights found above are used to construct a “connectivity matrix” \mathbf{A} that specifies the relationship between every node in the mesh. Each row number corresponds to the global node number for a given unknown (i.e., the field at that node). The non-zero elements in that row correspond to the α_i ’s associated with

the neighboring nodes and the node itself. The connectivity matrix is sparse, and it may have other structure (such as bandedness) that can be exploited. For nodes that are adjacent to the surface of the scatterer, one of the neighboring values corresponds to the known surface field which serves as the forcing function to the system of equations. Symbolically, this is written as

$$\mathbf{A} \cdot \mathbf{E} = \mathbf{F} \quad (8)$$

where \mathbf{E} contains the unknown field values at each node in the computational mesh and \mathbf{F} is the forcing function determined by a combination of the known surface field and the weights determined using the local polar approximation. The solution is then obtained via

$$\mathbf{E} = \mathbf{A}^{-1} \mathbf{F}. \quad (9)$$

Once \mathbf{E} has been determined, the actual surface currents are deduced and far-field quantities are obtained as described in Sec. IV.

III. Rough Surface Scattering Problem

Currently rough surface scattering is of interest to researchers in a variety of disciplines. It has applications in such diverse areas as ultrasonics, radar imaging, sonar

detection, solid-state physics, optics, astronomy, and microwave remote sensing.

In the past three decades, much work has been done in the development of approximate analytic models to predict wave scattering from rough surfaces. These include the small slope approximation [10, 11, 12], the phase perturbation technique [13, 14], the operator expansion method [15, 16], the Dashen-Wurmser approximation [17], the unified perturbation method [18, 19], and the quasi-slope approximation [20]. In addition, some work has been done in the development of Monte Carlo numerical techniques that are exact in the sense that no physical approximations are made in the underlying equations. These include techniques based on integral equations [21, 22], the finite element method [23], and finite difference methods [24, 25, 26]. In this work we consider the MEI method. We restrict our consideration to perfectly conducting, one-dimensional, randomly rough surfaces with Gaussian statistics and satisfying a Gaussian surface roughness spectrum [27]. Surfaces with Gaussian statistics have been studied extensively [11, 21, 28, 29].

The problem geometry is shown in Fig. 3. TM illumination is assumed so the total electric field at the surface vanishes (Dirichlet boundary condition). The surface profile is given by $f(x)$. The mean height of the surface is zero, i.e., $\langle f \rangle_s = 0$, where $\langle \cdot \rangle_s$ indicates averaging over the entire surface. The standard deviation, or RMS surface height, is given by $h = \sqrt{\langle f^2 \rangle_s}$. Both surface heights and slopes are Gaussian distributed.

The normalized correlation function is defined by

$$C(\zeta) = \frac{\langle f(x)f(x+\zeta) \rangle_s}{h^2}, \quad (10)$$

which for Gaussian surfaces is given by

$$C(\zeta) = \exp\left(\frac{-\zeta^2}{l^2}\right). \quad (11)$$

The correlation length l is the length at which the correlation function decreases by a factor of $1/e$. The surface roughness spectrum is obtained by taking the Fourier transform of $h^2 C(\zeta)$. For Gaussian surfaces, the statistics are completely specified by just two parameters, the correlation length and the RMS surface height, and generation of surface realizations is relatively simple [21, 27].

In numerical simulations of rough surface scattering, finite-length surfaces must be used to model scattering from infinite surfaces. When a single plane wave strikes

a finite-length surface, edge diffraction occurs. One way of minimizing diffraction effects is to construct an incident wave that tapers to very small values at the surface edges. Diffraction still occurs, but it makes negligible contributions to the scattered field. Tapered incident waves have been introduced by Thorsos [21] and Chan and Fung [22]. The tapered incident field used by Thorsos is an approximation to an incident field, consisting of an angular spectrum of plane waves, that satisfies the wave equation exactly. This approximate field is given by

$$E_z^i(\mathbf{r}) = \exp\left\{-jk_i \cdot \mathbf{r} [1 + w(\mathbf{r})] - (x - y \tan \theta_i)/g^2\right\} \quad (12)$$

where

$$w(\mathbf{r}) = [2(x - y \tan \theta_i)^2/g^2 - 1]/(kg \cos \theta_i)^2, \quad (13)$$

$\mathbf{r} = (x, y)$ is a point above the surface, θ_i is the incident angle measured from the vertical, and $\mathbf{k}_i = k_0(\sin \theta_i, \cos \theta_i)$ is the free-space incident wave vector in the xy plane. Equation (12) satisfies the wave equation to order $1/(k_0 g \cos \theta_i)^2$ for $k_0 g \cos \theta_i \gg 1$. The parameter g controls the tapering, and care must be taken in its choice. Angular resolution, edge effects, and accuracy in satisfying the wave equation all depend on g [21]. In addition, the tapering must be accomplished in such a way that differences between the finite surface, tapered plane wave results and infinite surface, single plane wave results are negligible. For the numerical examples presented in this paper, $g = L/4$ is used, where L is the horizontal extent of each surface.

For each numerical study, 50 finite-length surfaces are generated using the method proposed by Thorsos [21]. Monte Carlo results are then obtained by taking the ensemble average of the cross sections of the 50 surfaces. The general procedure is to randomly generate a surface spectrum that has Gaussian statistics and then inverse transform the spectrum to obtain a surface profile. Each surface consists of N discrete points horizontally separated by Δx over a surface length L' . The x component of each point along the surface is specified by the location $x_n = n\Delta x$ for $1 \leq n \leq N$. The surfaces are generated using

$$f(x_n) = \frac{1}{L'} \sum_{\ell=-N/2}^{N/2-1} F(K_\ell) \exp[-jK_\ell x_n] \quad (14)$$

FREE SPACE ABOVE SURFACE

$$\epsilon = \epsilon_0, \mu = \mu_0$$

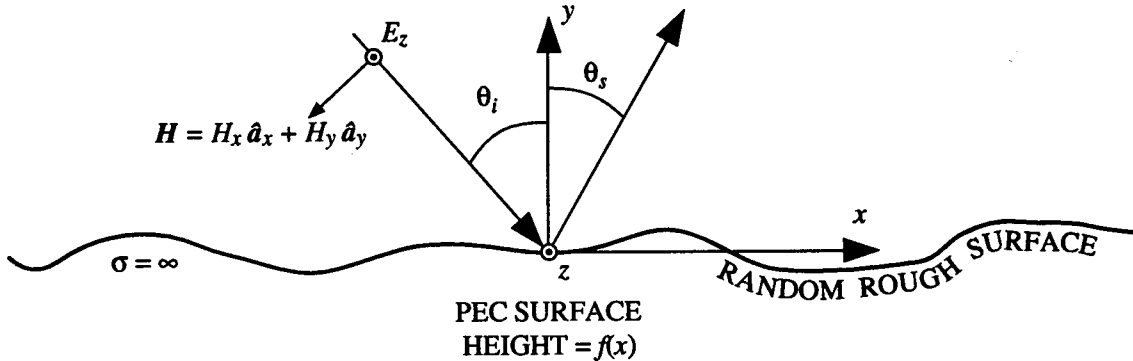


Figure 3: Problem geometry.

where, for $0 < \ell < N/2$,

$$F(K_\ell) = \sqrt{2\pi L' W(K_\ell)} \frac{1}{\sqrt{2}} [N(0, 1) - jN(0, 1)] \quad (15)$$

and for $\ell = 0$ or $N/2$

$$F(K_\ell) = \sqrt{2\pi L' W(K_\ell)} N(0, 1) \quad (16)$$

In (14)-(16)

$$W(K_\ell) = \frac{h^2 l}{2\sqrt{\pi}} \exp[-K_\ell^2 l^2 / 4] \quad (17)$$

is the Gaussian surface roughness spectrum, $K_\ell = 2\pi\ell/L'$, h is the RMS surface height, l is the correlation length, and $N(0, 1)$ is a number sampled from a Gaussian distribution with zero mean and unity variance. For $\ell < 0$, $F(K_{-\ell}) = F(K_\ell)^*$.

The nature of the discrete spectrum causes correlation of the ends of each surface. To circumvent this, an extended surface, several times longer than the N required points, is generated. Each surface used in the numerical simulation is then cut from the longer surface and, hence, the correlation of the ends is negligible. For the numerical studies presented here, surfaces with a length of $L' = 256\lambda$ were generated but segments of length $L = 80\lambda$ were used in the calculations (λ is the wavelength of the illumination).

IV. MEI Method for Rough Surfaces

In order to use the MEI method, a computational mesh enclosing the scattering object must be specified. Figure 4

shows a segment of a typical surface with a two-layer computational mesh. To generate the mesh, two mesh points are specified for each surface point. Both points are along the surface normal and are separated by a distance Δv . To obtain the surface normal, the surface slope is needed. The x and y components of the surface unit normal vector are

$$n_x = \frac{-f'(x)}{\sqrt{1 + [f'(x)]^2}} \quad (18)$$

$$n_y = \frac{1}{\sqrt{1 + [f'(x)]^2}} \quad (19)$$

where $f'(x) = df/dx$. The surface derivative could be obtained approximately using finite differences; however, the surface spectrum is needed to generate the surface realizations and is available to obtain surface slopes (see (14)). Thus, we find $f'(x)$ via

$$f'(x) = \mathcal{F}^{-1}(jKF(K)) \quad (20)$$

where \mathcal{F}^{-1} denotes the inverse Fourier transform.

Note that the surface generation scheme creates points that are *horizontally* offset from neighboring points by Δx . However, since neighboring points do not necessarily have the same vertical components, the distance between points is nonuniform.

Figure 5 shows an expanded view of one corner of the computational mesh. The global node numbers are shown together with some of the node interconnections. Odd-numbered nodes correspond to nodes in the interior while even-numbered nodes are on the outer boundary. The

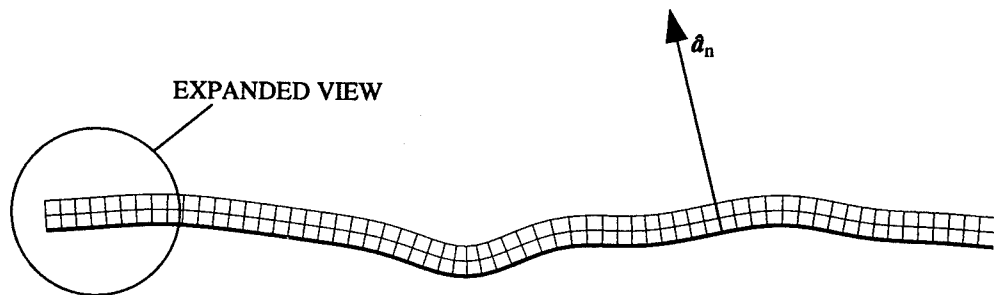


Figure 4: Segment of typical surface and computational mesh.

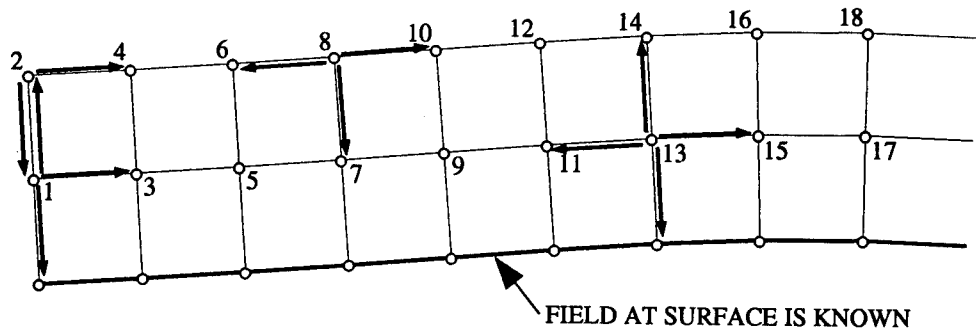


Figure 5: Expanded view of computational mesh.

first and last two nodes are exceptional and must be given special consideration. In our implementation, all odd nodes (except 1 and $N - 1$) are connected to neighboring nodes in a manner similar to node 13 shown in Fig. 5. Since neighbors are available above, below, to the left, and to the right, the local polar scheme proposed by Pous can be employed [2]. As mentioned before, this simplifies calculation of the connectivity weights and makes consideration of the singularity in the Green's function at the surface unnecessary. All even nodes between 2 and N are handled using the MEI method. These nodes are connected to one neighbor in the interior and to the neighbors to the left and right as shown for node 8. Nodes 2 and N are both connected to only two neighbors and are handled using the MEI method. Nodes 1 and $N - 1$ are treated using the local polar approximation. For these nodes, an additional node is assumed to exist to the left of node 1 or to the right of node $N - 1$ so that the proper weights can be determined. However, the field is assumed to be zero at the fictitious neighbor and it does not enter into the calculation. Note that the tapered incident field is small near nodes 1 and $N - 1$ so setting the field to zero should introduce negligible error. With this connectivity scheme, the connectivity matrix \mathbf{A} is not only sparse, but is also tightly banded—there are a total of five diagonals (including the main diagonal) that contain non-zero elements. A number of public domain routines exist, such as those in LINPACK [30], that can be used to efficiently invert such a matrix.

In many rough surface scattering problems bistatic results span a range of over 60 dB. For instance, for slightly rough surfaces the coherent specular reflection contains significant energy relative to the incoherent energy found at grazing angles. This dynamic range requires an extremely accurate numerical solution. In previously published results the accuracy of MEI-based solutions was, at most, weakly dependent on the selection of metrons. However, we found that using an initial selection of metrons that are physically unrealizable leads to poor results. Because of the accuracy required and the difficulty in making a “good” initial selection of metrons, an iterative scheme was used. The initial set of metrons was

$$\begin{aligned} J_s^1(\mathbf{r}_i) &= \exp(-x_i^2/g^2) \\ J_s^2(\mathbf{r}_i) &= \cos(k_0 \xi_i) \end{aligned}$$

$$\begin{aligned} J_s^3(\mathbf{r}_i) &= \sin(k_0 \xi_i) \\ J_s^4(\mathbf{r}_i) &= \exp(-x_i^2/g^2) \cos(k_0 y_i) \\ J_s^5(\mathbf{r}_i) &= \exp(-x_i^2/g^2) \sin(k_0 y_i) \end{aligned}$$

where g is the taper factor commensurate with the incident field, $\mathbf{r}_i = (x_i, y_i)$ corresponds to the i th point along the surface, ξ_i is the path length along the surface from the first point to the i th point, and k_0 is the free-space wavenumber. Using the following Green's function

$$G(\mathbf{r}|\mathbf{r}') = \frac{k_0 \eta_0}{4} H_0^{(2)}(k_0 |\mathbf{r} - \mathbf{r}'|), \quad (21)$$

where η_0 is the characteristic impedance of free space, the measured fields are obtained (see (5)) using

$$E_z^n(\mathbf{r}) \approx \sum_{i=1}^N J_s^n(\mathbf{r}_i) G(\mathbf{r}|\mathbf{r}_i) \Delta \xi_i \quad (22)$$

where $\Delta \xi_i$ is the distance from the i th to the $(i + 1)$ th point ($\Delta \xi_N$ is set equal to $\Delta \xi_{N-1}$).

The iterative scheme proceeds as follows. The metrons shown above are employed in the MEI method to obtain the fields above the surface. From these fields a surface current is obtained. The calculated current is used to replace one of the metrons. The calculation of fields and currents is repeated except now a different metron is replaced with the calculated current. This is repeated until sufficient accuracy is obtained or there are no more metrons to update. For each iteration, it was found that there is virtually no change in the scattered field in regions where there is significant energy. The iterative scheme is only necessary to obtain improved accuracy where the fields are significantly less than the maximum. There are a myriad of other iterative schemes that could be developed; the one presented here is not necessarily the optimum one. A better initial selection of metrons may have eliminated the need for iteration. However, this scheme does illustrate that an iterative technique can be used when there is little or no *a priori* knowledge of the actual source distribution.

It is worth mentioning that, in principle, an iterative scheme can be done with little additional computational overhead. The majority of CPU time is spent calculating the terms $G(\mathbf{r}|\mathbf{r}_i)$ for pairs of surface and mesh points. In principle, these terms just need to be calculated once (since they depend only on the geometry of the grid) and then multiplied later by the appropriate

metrons. However, in practice this requires the storage of $2N^2$ terms, which represents a prohibitive amount of memory for large problems. The code developed for this study was not optimized, and the Green's functions were recalculated for each iteration.

To calculate far-field quantities or to update the metrons in the iterative scheme, it is necessary to obtain the surface currents from the MEI-derived electric field. The currents are found using

$$J_s = \frac{-1}{jk_0\eta_0} \frac{\partial E_z}{\partial n} \quad (23)$$

where n is normal to the surface. Given the mesh structure and the fact that the total field is zero at the surface, the current can be found at a point on the surface using

$$J_s \approx \frac{-1}{jk_0\eta_0} \frac{E_z(\Delta v)}{\Delta v} = \frac{-1}{jk_0\eta_0} \frac{(E_z^{\text{mei}}(\Delta v) + E_z^{\text{inc}}(\Delta v))}{\Delta v} \quad (24)$$

where $E_z^{\text{mei}}(\Delta v)$ is the MEI-derived scattered field at the first mesh point above the surface (i.e., the first point above the surface normal and on the surface normal) and $E_z^{\text{inc}}(\Delta v)$ is the known incident field at the same point. However, this is only accurate to order $O(\Delta v)$. Since the scattered field is available at two mesh points above the surface, the surface current is obtained using second-order forward-differencing. Thus, the normal derivative is found using

$$\frac{\partial E_z}{\partial n} \approx \frac{1}{2\Delta v} (4E_z(\Delta v) - E_z(2\Delta v)) \quad (25)$$

where $E_z = E_z^{\text{mei}} + E_z^{\text{inc}}$ is the total field.

Our goal is to calculate the bistatic radar cross section per unit length for a plane wave incident on a 1-D surface. This is found using [31]

$$\sigma(\theta_s, \theta_i) = 2\pi \frac{I_s \rho}{I_i L} \quad (26)$$

where ρ is the distance to the far-field observation point, L is the length of the surface, I_s is the scattered intensity, I_i is the incident intensity, θ_s is the angle of observation measured from the vertical, and θ_i is the angle of incidence measured from the vertical. In order to find the bistatic radar cross section, it is necessary to convert the surface current to the electric field in the far field. Equation (22) could be used; however, given the distant location of the observation point, the large argument approximation of the Hankel function is used. Thus, for an

incident field with unit magnitude, we obtain the cross section using

$$\sigma(\theta_s, \theta_i) = \frac{k_0}{4} \left| \sum_{i=1}^N J_s(\mathbf{r}_i) \Delta \xi_i \exp(jk_0(x_i \cos \theta_s + y_i \sin \theta_s)) \right|^2. \quad (27)$$

V. Results

To illustrate the results of the method, consider a surface with $k_0 h = 0.33$ and $k_0 l = 2.83$. This surface has an RMS slope angle of $\gamma = 9.46^\circ$. Fifty surface realizations of length $L = 80\lambda$ were generated and enclosed in a mesh with $\Delta x = \Delta v = \lambda/16$. (This mesh spacing is typical of that reported in other applications of the MEI method. It was found that using a finer spacing did not improve the results, while a coarser mesh yielded slightly worse results.) Figure 6 shows the bistatic radar cross section obtained using the MEI method and an FDTD technique [32] that is known to be accurate for this type of surface. Since normal incidence was used, coherent specular return is at 0° . The small oscillations in the curve are due to the use of a finite number of surface realizations. Since two different sets of surface realizations were used, the oscillations do not coincide. These two methods show excellent agreement throughout the 60 dB range of the results. The MEI method results were obtained after three iterations of the metrons.

Figure 7 shows the cross section when the same surface as used for the results in Fig. 6 is illuminated by a wave incident at 45° . All aspects of the calculation (e.g., mesh structure, taper factor, and surface realizations) are the same as before except five iterations were used. As expected, the coherent specular peak is at 45° . The two results show excellent agreement everywhere except toward backward grazing angles.

Figure 8 shows the results for a surface with $k_0 h = 1.72$ and $k_0 l = 7.31$ that is illuminated with a normally incident wave. Five iterations were used. Compared to the previous surface, the correlation length has increased by a factor of $2\frac{7}{12}$ and the RMS surface height has increased by twice this same factor. This change in parameters approximately doubles the RMS slope angle so that it is now 18.43° . Because this surface is fairly rough, it produces no clear specular return; instead incoherent energy is broadly distributed over a range of scattering angles.

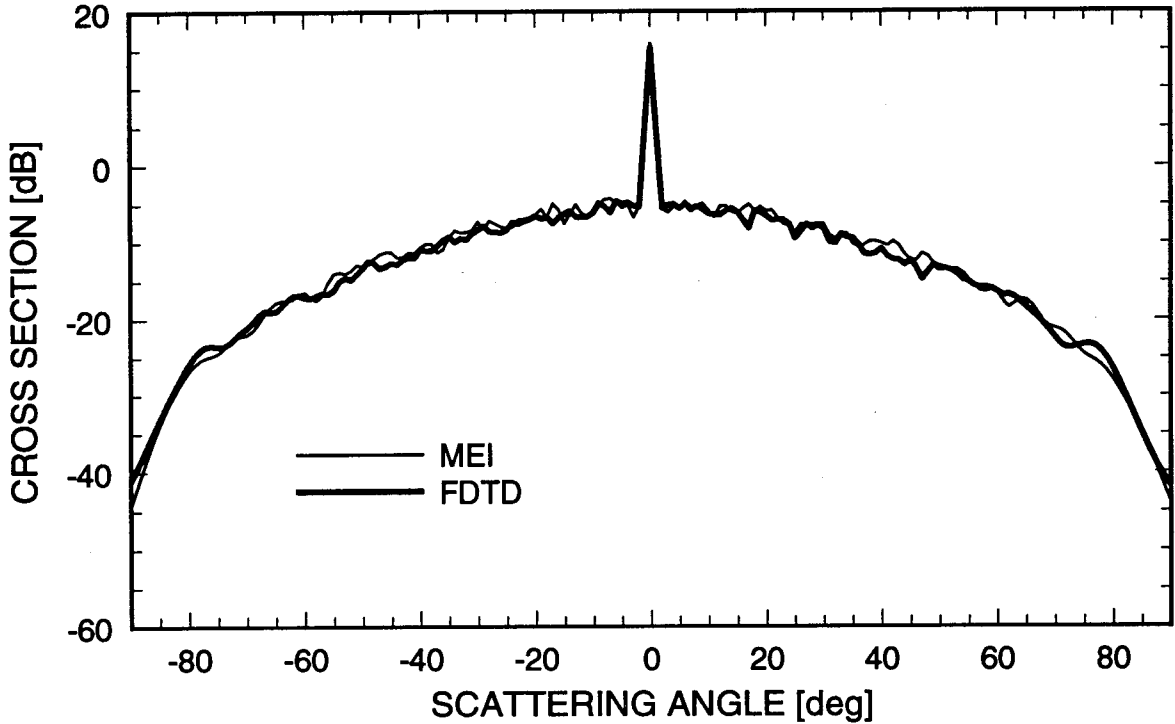


Figure 6: Radar cross section as a function of scattered angle for normal illumination of a surface with $k_0 h = 0.33$ and $k_0 l = 2.83$.

Again, there is good agreement between the two methods except at low grazing angles where the MEI method overpredicts the cross section.

The three results presented here were done in a consistent manner, i.e., all were solved using the same approach. The only difference between runs was the number of iterations—no other modifications were attempted to try to optimize the results for a particular geometry. In fact, there is every reason to believe that the results presented here are not optimum. For example, a better metron for use in the initial set might be one obtained from the physical optics equivalent, namely, $\mathbf{J}_s \approx 2\mathbf{n} \times \mathbf{H}^{\text{inc}}$. This could be used instead of the constant metron J_s^1 given in (21) and probably would be appropriate for surfaces with relatively long correlation lengths. Additionally, by incorporating the x and y components of the wavenumber rather than just using k_0 , the metrons could contain more knowledge of the incident field. There may also be better mesh structures than the one presented here.

V. Conclusions

Although the limits of the MEI method have not been completely explored, the work presented in this paper illustrates that the method has the potential to provide accurate solutions to rough surface scattering problems. The problem examined in this study required a large dynamic range. Accuracy was achieved using an iterative scheme. Additional accuracy was obtained by calculating the surface currents using second-order forward differencing.

Since the MEI method provides a solution via a sparse and relatively small matrix, it can potentially solve rough surface scattering problems in three dimensions. In that case the metrons would be a function of two variables, rather than one, and it may be much harder to select “good” metrons. Therefore, the use of an iterative scheme in three dimensions may be critical for successful implementation.

The TE problem has not been discussed but is solved in a manner very similar to that presented here. The solution for penetrable objects involves enclosing the material

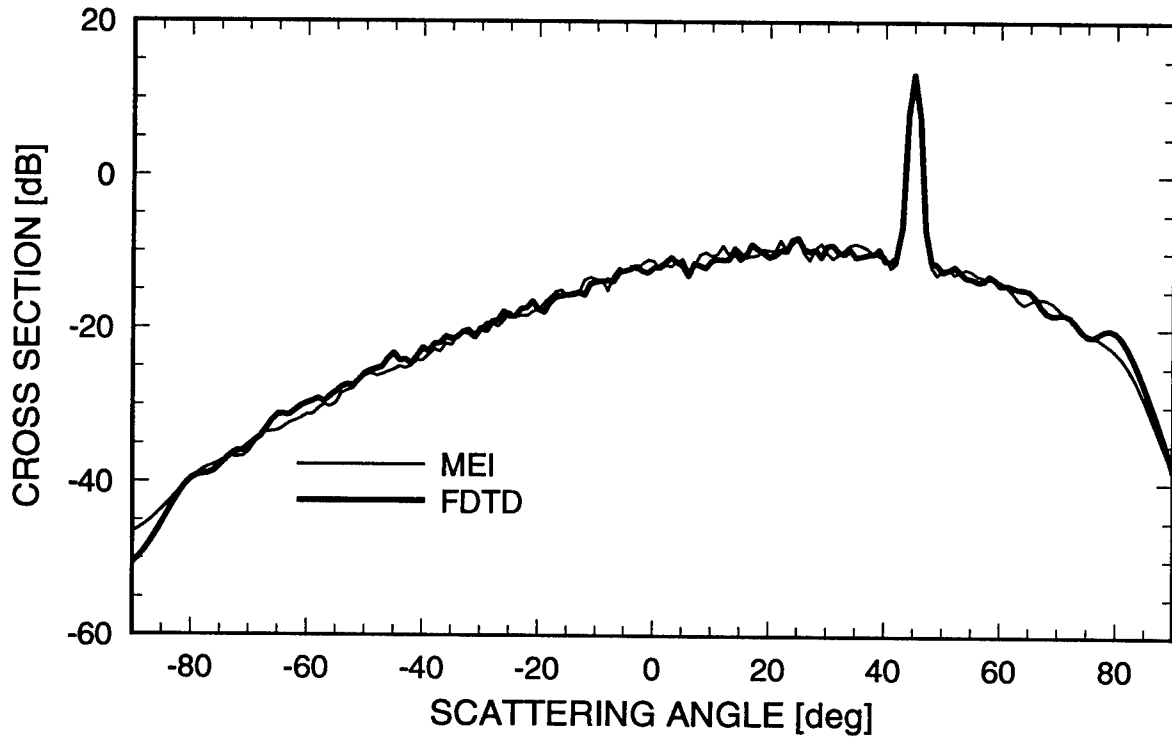


Figure 7: Radar cross section as a function of scattered angle when $\theta_i = 45^\circ$ for a surface with $k_0 h = 0.33$ and $k_0 l = 2.83$.

interface in a mesh—with mesh points on both sides of the interface. This mesh can be terminated close to the interface, but the solution is complicated by the fact that metrons must be specified in terms of both their value at the surface and their normal derivative at the surface.

Several other problems remain to be investigated. For example, if a surface is extremely rough, the computational mesh may cross itself. In other words, as mesh points are placed along the surface normal, some points will no longer have monotonically increasing values in the x direction if the normal directions change too abruptly (such as in a narrow valley). This type of highly distorted mesh does not permit use of the local polar approximation but may yield to analysis by using the MEI method for nodes in the vicinity of the mesh overlap. Other remaining topics include determination of optimum mesh structure (both in terms of spacing and number of layers) and best selection of metrons.

Acknowledgements

This work was supported by the Office of Naval Research, Code 3210A, and by the National Science Foundation under Grant No. ECS-9253547.

References

- [1] K.K. Mei, R. Pous, Z. Chen, and Y. Liu. Measured Equation of Invariance: A New Concept in Field Computation. In 1992 IEEE AP-S International Symposium and URSI Radio Science Meeting Digest, page 544, Chicago, IL, July 1992.
- [2] R. Pous. *The Measured Equation of Invariance: A New Concept in Field Computation*. PhD thesis, University of California, Berkeley, CA, 1992.
- [3] M.D. Prouty, K.K. Mei, S.E. Schwarz, and R. Pous. A New Approach to Quasi-Static Analysis with Application to Microstrip. *IEEE Microwave and Guided Wave Letters*, 3(9):302–304, 1993.

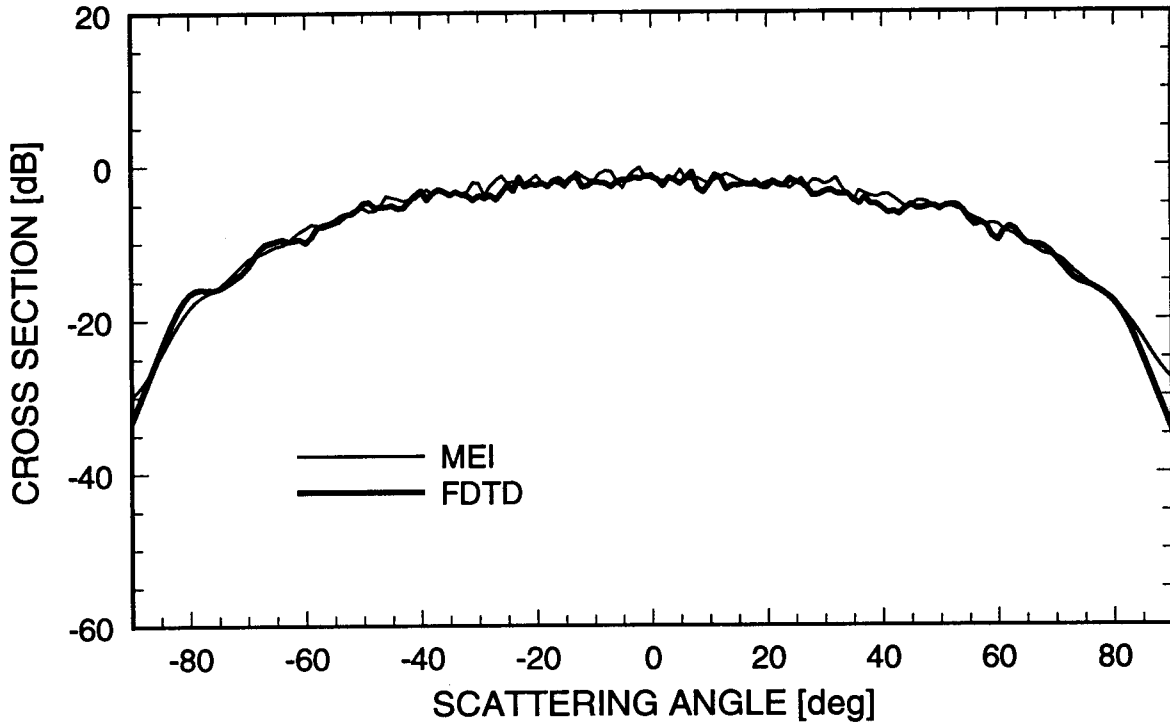


Figure 8: Radar cross section as a function of scattered angle for normal illumination of a surface with $k_0h = 1.72$ and $k_0l = 7.31$.

- [4] K.K. Mei, R. Pous, Z. Chen, Y.W. Liu, and M.D. Prouty. Measured Equation of Invariance: A New Concept in Field Computation. *IEEE Trans. Antennas Propagat.*, 42(3):320–328, 1994.
- [5] A.C. Cangellaris and D.B. Wright. Application of the Measured Equation of Invariance to Electromagnetic Scattering by Penetrable Bodies. *IEEE Trans. Mag.*, 29(2):1628–1631, 1993.
- [6] D.B. Wright and A.C. Cangellaris. MEI-Based Mesh Truncation Conditions for the Finite-Element Modeling of EM scattering by Two-Dimensional Penetrable Targets. In 1993 IEEE AP-S International Symposium and URSI Radio Science Meeting, Ann Arbor, MI, June 1993.
- [7] Y. Li, Z.J. Cendes, and X. Yuan. A Modified MEI Method for Solving Scattering Problems with the Finite Element Method. In 1993 IEEE AP-S International Symposium and URSI Radio Science Meeting, Ann Arbor, MI, June 1993.
- [8] T.L. Barkdoll and R. Lee. Finite Element Analysis of Bodies of Revolution Using the Measured Equation of Invariance. In 1993 IEEE AP-S International Symposium and URSI Radio Science Meeting, Ann Arbor, MI, June 1993.
- [9] J.L. Young, J.B. Schneider, and R.G. Olsen. Laplace's Equation and the Measured Equation of Invariance. In COMPUMAG Conference on the Computation of Electromagnetic Fields, Miami, Florida, November 1993.
- [10] A.G. Voronovich. Small-Slope Approximation in Wave Scattering by Rough Surfaces. *Sov. Phys. JETP*, 62(1):65–70, 1985.
- [11] S.L. Broschat and E.I. Thorsos. A Numerical Study of the Small Slope Approximation for Rough Surface Scattering. In Topical Meeting of the ICO, Atmospheric, Volume, and Surface Scattering and Propagation, Florence, Italy, 1991.

[12] E.I.Thorsos and S.L. Broschat. An Investigation of the Small Slope Approximation for Scattering from Rough Surfaces: Part I—Theory. *J. Acoust. Soc. Am.*, 97(3), 1995.

[13] D. Winebrenner and A. Ishimaru. Investigation of a Surface Field Phase Perturbation Technique for Scattering from Rough Surfaces. *Radio Sci.*, 20:161–170, 1985.

[14] R.M. Fitzgerald and A.A. Maradudin. A Reciprocal Phase-Perturbation Theory for Rough-Surface Scattering. *Waves in Random Media*, 4:275–296, 1994.

[15] D.M. Milder. An Improved Formalism for Wave Scattering from Rough Surfaces. *J. Acoust. Soc. Am.*, 89(2):529–541, 1991.

[16] P.J. Kaczkowski and E.I. Thorsos. Application of the Operator Expansion Method to Scattering from One-Dimensional Moderately Rough Dirichlet Random Surfaces. *J. Acoust. Soc. Am.*, 96(2):957–972, 1994.

[17] R. Dashen and D. Wurmser. Approximate Representation of the Scattering Amplitude. *J. Math. Phys.*, 32:986–996, 1991.

[18] E. Rodriguez and Y. Kim. A Unified Perturbation Expansion for Surface Scattering. *Radio Sci.*, 27:79–93, 1992.

[19] E. Rodriguez, Y. Kim, and S.L. Durden. A Numerical Assessment of Rough Surface Scattering Theories: Horizontal Polarization. *Radio Sci.*, 27:497–513, 1992.

[20] V.I. Tatarskii. The Expansion of the Kirchoff Approximation for Rough Surface Scattering Using a Gaussian Roughness Spectrum. *Wave in Random Media*, 3:127–146, 1993.

[21] E.I. Thorsos. The Validity of the Kirchhoff Approximation for Rough Surface Scattering Using a Gaussian Roughness Spectrum. *J. Acoust. Soc. Am.*, 83:78–92, 1988.

[22] H.L. Chan and A.K. Fung. A Numerical Study of the Kirchhoff Approximation in Horizontally Polarized Backscattering from a Random Surface. *Radio Sci.*, 13(5):811–818, 1978.

[23] S.H. Lou, L. Tsang, and C.H. Chan. Application of the Finite Element Method to Monte Carlo Simulations of Scattering of Waves by Random Rough Surfaces: Penetrable Case. *Waves in Random Media*, 1:287–307, 1991.

[24] A.K. Fung, M.R. Shah, and S. Tjuatja. Numerical Simulation of Scattering from Three-Dimensional Randomly Rough Surfaces. *IEEE Trans. Geosci. Remote Sensing*, 32(5):986–994, 1994.

[25] C.H. Chan, S.H. Lou, L. Tsang, and J.A. Kong. Electromagnetic Scattering of Waves by Rough Surfaces: A Finite-Difference Time-Domain Approach. *Microwave Opt. Technol. Lett.*, 4(9):355–359, 1991.

[26] F.D. Hastings, S.L. Broschat, and J.B. Schneider. An Application of the Contour Path Finite-Difference Time-Domain Method to Rough Surface Scattering. In 1993 IEEE AP-S International Symposium and URSI Radio Science Meeting, Ann Arbor, MI, June 1993.

[27] J.A. Ogilvy. *Theory of Wave Scattering from Random Rough Surfaces*. Adam Hilger, Bristol, England, 1991.

[28] E.I. Thorsos. The Validity of the Perturbation Approximation for Rough Surface Scattering Using a Gaussian Roughness Spectrum. *J. Acoust. Soc. Am.*, 86:261–277, 1989.

[29] S.L. Broschat, E.I. Thorsos, and A. Ishimaru. The Phase Perturbation Technique vs an Exact Numerical Method for Random Rough Surface Scattering. *J. Electromagnetic Waves Applications*, 3(3):237–256, 1989.

[30] J.J. Dongarra, C.B. Moler, J.R. Bunch, and G.W. Stewart. *LINPACK User's Guide*. Society for Industrial and Applied Mathematics, Philadelphia, PA, 1979.

[31] A. Ishimaru. *Wave Propagation and Scattering in Random Media*. Academic, New York, 1978.

[32] F.D. Hastings, J.B. Schneider, and S.L. Broschat. A Monte Carlo Contour Path FDTD Technique for Rough Surface Scattering. Submitted to *IEEE Trans. Antennas Propagat.*, 1994.

WIREGRID: A NEC2 pre-processor

C. F. du Toit, D.B.Davidson
Dept. of Electrical and Electronic Engineering
University of Stellenbosch
Stellenbosch 7600
South Africa
e-mail: davidson@firga.sun.ac.za

Abstract

WIREGRID is a pre-processor for the widely used public domain method of moments computer code NEC2. WIREGRID was developed for modelling metallic structures using a mesh of wires. In particular, it has powerful facilities for controlling the density of the mesh, permitting the same basic model to be used for different frequencies, with the code automatically generating a suitable mesh for a particular frequency. WIREGRID is not limited to generating wire meshes: it can also be usefully applied to true thin-wire modelling, for instance for Yagi-Uda and log-periodic antennas. In this paper, the basic philosophy of the code is described, and the code capabilities are detailed. Sufficient detail is presented so that the paper can serve as a reference for code users. The meshing algorithm is briefly described. An example is shown of the automatic mesh generation capabilities applied to an automobile. WIREGRID is available in the public domain via anonymous ftp; details of the ftp sites and hardware requirements are given in the appendices.

1 Introduction

NEC2 has become the *de-facto* standard thin-wire method of moments code that other codes are evaluated against, due not least to:

- Its powerful facilities for general thin-wire modelling. These include not only the conventional free-space treatment but also a ground treatment (both an approximate reflection coefficient approach and an "exact" — in a numerical sense — Sommerfeld treatment). NEC2 can also exploit symmetry, and handle non-radiating networks and lumped loads. This brief review highlights only some of its capabilities.
- The extensive documentation available.
- The widespread availability of the code.

However, anyone who has used NEC2 is well aware that the code, powerful as it is, can be frustrating and time-consuming to use, since the model input is described by a list of coordinate points. It is extremely easy to make an error in such an input file, and very difficult to pick it up without some graphical aid. Furthermore, when such an error is present, the code will often run and produce results that are plausible but incorrect. Hence a number of pre-processors have been written specifically for NEC2 to simplify model generation, one of which is the subject of this paper, namely WIREGRID, which we are making available in the public domain. We assume a basic familiarity with NEC2 in this paper, since WIREGRID was written specifically for NEC2 model generation.

DIDEC was one of the first pre-processors for NEC2 [1]. However, IGUANA (available from ACES as part of the NEEDS package) was one of the first *widely available* such pre-processors; it has been generally acknowledged as a useful tool but with a number of deficiencies. Work has also been reported by other researchers on graphical tools for preparing NEC2 data files; this journal has published at least two such papers [2, 3] and the 1993 ACES conference saw a number of codes of varying quality and cost being demonstrated. As this paper went to print, another South Africa group working at the University of the Witwatersrand announced a commercial software package called SIG (Structure Interpolation and Gridding), which offers facilities similar to or exceeding those in WIREGRID [4].

Our pre-processor WIREGRID was originally developed for a specific application of NEC2, namely modelling metallic structures using a mesh of wires, from whence the name. In particular, it has very powerful facilities for controlling the *density* of the mesh, permitting the same basic model to be used for different frequencies, with the code automatically generating a suitable mesh for a particular frequency (according to the $\lambda/10$ rule, for instance). Anyone who has had to generate a wire grid manually or even using a pre-processor such as IGUANA will know that this is an arduous task:

specifying the end point coordinates of each wire segment of the mesh (of even relatively simple structures) in the format required by NEC2 is an error-prone and exhausting task when done once; and if total number of segments has to be changed to produce a finer or coarser discretization, the structure must almost be re-modelled from scratch for each change. WIREGRID was developed to simplify these tasks considerably. The initial number of coordinates that must be typed in by hand is typically reduced by at least one order of magnitude for coarse meshes, and two or even three orders for fine meshes. Since many structures can be modelled by a number of flat or almost flat polygonal surfaces, it was decided that a pre-processor was needed which would take as input just the vertices of these polygons, and which would then generate the wiregrid discretization automatically. Changing the segment density then only requires a few keystrokes. Once the user is satisfied with the model, the code automatically generates the NEC2 input file with the geometry cards and a limited number of control cards.

WIREGRID is not limited to generating wire meshes: it can be usefully applied to true thin-wire modelling, for instance for Yagi-Uda and log-periodic antennas, and was most recently used for a project involving frequency selective surface modelling. However, most of its features were developed with wiregrid modelling in mind, since at the time the first version was developed (1990) we were involved with the electromagnetic characterization of HF and VHF whip antennas mounted on ground vehicles and we were encountering serious problems preparing the large data sets that this application required. Closely related research on developing a parallel version of NEC2 was also in progress at that time [5, 6]; due to the increased problem size that this parallel version of NEC2 could handle, WIREGRID also proved very useful with this work.

The code was originally developed by the first author in close liaison with the second author, and has subsequently been extensively used for both vehicle EMC modelling under contract (as outlined above) and teaching (at undergraduate and postgraduate level, as well as for short courses on NEC2). The idea underlying the code is similar to that reported by Najm [3], but the implementation is rather different. WIREGRID is highly graphically orientated, whereas Najm's code is not. It also automates a number of functions that Najm's code requires manual intervention to implement; see for example the discussion regarding the motor vehicle [3, Fig. 5]. Despite the conceptual similarities of the two codes, WIREGRID was developed independently and at about the same time [7].

As with most complex computational electromagnetic codes, while a pre-processor such as WIREGRID greatly simplifies the task of the user, a knowledge of the input

requirements, and the basic functioning, of the code is still highly advisable. The user may need to append additional control statements to the input file and may even want to change some of the geometry data afterwards.

2 Using the program

2.1 Structure Modelling

The tasks required by the user are the following: The structure must first be divided into fairly flat polygonal surfaces, which are called major elements (see Fig. 1). WIREGRID can handle up to 160 such major elements. Each major element does not need to lie *completely* in a 2D plane, but severely "twisted" elements are really beyond the capability of the code. The frequent visual feedback available from the program will permit the user to identify unsuitable elements and rectify them. As mentioned in the Introduction, the code was developed for structures consisting mainly of flat surfaces; it is not really suited modelling curved surfaces, such as an aircraft fuselage. The coordinates of each major element's vertices, called major nodes, must be determined next (see Fig. 1). The simplest major element is defined by two major nodes, which would model a single straight wire. The most complex major element may be defined by a maximum of 10 major nodes.

When generating a mesh, it is important to ensure that meshes in adjacent elements are properly electrically connected across the boundary. (NEC2 users will be aware of a particularly insidious fault caused by two wires whose end-points that are closely located and should be physically connected, but are treated by the code as unconnected.) We will use the term conformality in this paper to describe a properly connected mesh. WIREGRID will ensure conformality provided that major nodes of adjacent major elements coincide on the boundary that the elements share. These requirements mean that when vertices on the boundary between two adjacent polygons are not coincident, extra major nodes for one or both of them must be defined. These extra nodes must coincide with the unmatched vertices (see Fig. 2). The same technique can be used for ensuring that a whip antenna is properly grounded to the vehicle frame. Superfluous nodes (for example, a node in the middle of an element side when there are no conformality problems) do not cause any problem within the program (providing of course that all elements sharing that side contain the extra node). However, the wire mesh generated may be distorted by their presence, and it is recommended that such unnecessary major nodes be avoided.

An additional geometric requirement for the major elements is that they must be convex, i.e. a straight line

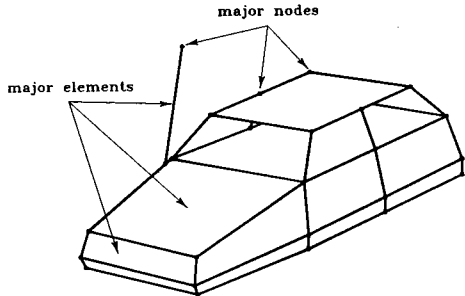


Figure 1: Arbitrary structures can be built up with flat polygonal surfaces. The example shows a simplified model of a generic “hatchback” motor car.

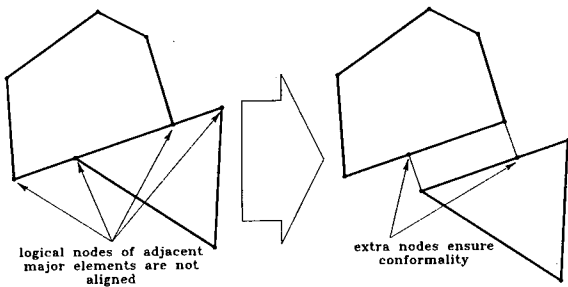


Figure 2: To ensure that the mesh within each major element is electrically continuous across the common side, extra major nodes must sometimes be added as shown here.

joining any two points in the polygon must still be enclosed by the polygon boundaries. The reason for this requirement is that it greatly simplifies the task of the mesh generator in WIREGRID. It can be adhered to easily, since any non-convex polygon can be divided into two or more convex parts.

A number tag starting from 0 is assigned by WIREGRID to each major element. It is often helpful to keep a rough sketch of the structure, indicating all the major elements with their number tags. In the NEC2 input file that WIREGRID generates, all wires belonging to a certain major element will be tagged with this number. When certain wires are to be loaded, excited or even altered by hand, this will help to locate them.

2.2 Discretization

The *nominal length* ℓ_n of the wire segments in the mesh may be changed at any time during the structure modelling process. The new discretization is performed immediately. The nominal segment length is a key concept in the code: each straight wire is divided into p segments, defined by

$$p = \text{int} \left(\frac{L}{\ell_n} + 0.99999 \right), \quad (1)$$

where L is the length of the wire section and $\text{int}(x)$ is the integer operator, taking the integer part of x .

All straight wires belonging to a major element defined by more than two major nodes are divided into segments of equal length. Following the “same surface rule” [8], these wires are modelled with a radius of $\frac{\ell_n}{2\pi}$.¹

When the wire is a major element defined by two nodes, the “same surface rule” is irrelevant, and the user must specify radii for the two end points, which is independent of the discretization. (The code still offers a radius of $\frac{\ell_n}{2\pi}$ as the default, although this will of course almost certainly be incorrect in this case). The number of segment divisions on the wire is still defined by (1). In addition to simple wires of uniform radius (corresponding to a GW NEC2 card), WIREGRID can also handle tapered wires, generating the necessary GW and GC cards.

2.3 A brief overview of the meshing algorithm

A detailed description of the meshing algorithm is beyond the scope of this paper. The following description

¹One reviewer expressed surprise at this radius, but Ludwig’s paper does indeed verify this rule. This rule actually refers to each polarization, so as Ludwig comments, “twice surface area rule” might be a better name. Trueman and Kubina give the same formula for wire radius [2, p.21]. Wires of this radius are on the verge of being too thick for the thin-wire treatment in NEC2 (the extended kernel option does not help with a mesh, since it cannot be used for segments with a complex junction), but experience has produced generally acceptable results following this rule.

is intended to give only a flavour of the meshing algorithm. Figure 3 shows the significant features of the meshing process, and will be referred to during this discussion. Five major nodes are shown by \bullet ; only four are actually required for this major element, but the fifth would be required if another major element were to have a major node at this point. (See for instance Figure 2 for such an example.) At the risk of tedium, we reiterate that the coordinates of these major nodes are all that the user need enter.

- The sides of the polygonal are divided up, as close to the specified nominal segment length as possible. These generate minor nodes along the sides. The minor nodes are represented by \circ in Figure 3. These minor nodes are then used to the basis for the mesh as follows:
- The vertex with included angle closest to 90° is then found.
- The sides of the polygon are then numbered counter-clockwise. Assume that the polygon is close to rectangular; this will then generate sides 1 to 4.
- Starting at the first point on side 1 where a minor node should be located, the code constructs vertical cross-wires from side 1 to side 3, endeavouring to keep the cross-wires as close as possible to parallel to each other. (These wires are coloured red on the screen).
- Once these cross-wires have been constructed, the cross-wires connecting sides 2 and 4 are constructed in a similar fashion. (These are coloured blue). The mesh thus created is shown in Figure 3. The mesh is represented by the dashed lines in the figure. In general, the horizontal cross-wires are individual wires running between each vertical cross-wire, with potentially slightly different lengths and directions. However, due to the geometrical simplicity of this example, all cross-wires in Figure 3 are uniform.
- The code has a number of features to try to generate a “good” mesh for irregularly shaped polygons; for instance, a point on a side may sometimes be skipped if a “better” mesh can be constructed by using the next point on a side as the end-point for a cross-wire. (“Good” and “better” refer to the angles that the cross-wires make with the element sides.) The intersections of the “blue” and “red” wires may also be perturbed slightly with the aim of making the included angles between the wires as close as possible to 90° . (Neither of these mesh improvement stages are required in the mesh of Figure 3.)
- The code tries to avoid creating long, thin triangular meshes. (The triangular examples shown by Najm

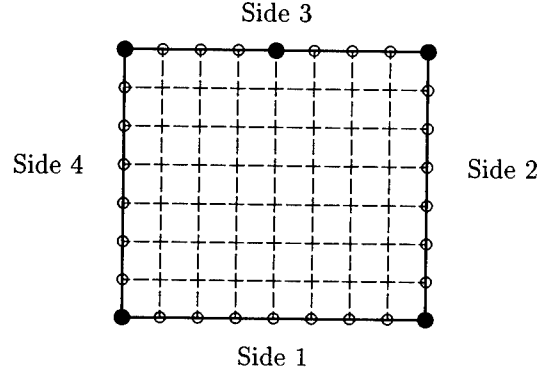


Figure 3: A rectangular major element illustrating the meshing algorithm outlined in Section 2.3. See text for discussion.

[3] are not good meshes for NEC2: with a significant wire radius they are very likely to generate match points inside another wire’s volume; the NEC2 user guide specifically cautions against this [9, p.3-6]). Users should try to avoid entering major elements with such geometries. Automatically detecting such violations of the NEC2 rules and guidelines is a feature we would like to add but have not yet; we will comment on this later.

2.4 Generation of the NEC2 input file

WIREGRID supports two data formats for the NEC2 input file:

- Fixed length data fields. All numbers are separated by spaces, where all integers occupy fields three to five characters long, and floating point numbers occupy 10 character long fields. This is the format documented in the user guide [9].
- Variable length data fields. All numbers are separated by commas. A number of newer versions of NEC2 also support this format.

When satisfied with the model, the first part of the NEC2 input file containing all the geometric data may then be generated on command.

WIREGRID also provides for the generation of control statements which allow maximum coupling computation between voltage sources, and radiation pattern generation at specified frequencies. Only wire segments belonging to major elements defined by *two* nodes may be excited for this purpose. (Of course, the experienced user can edit the NEC2 data file created by WIREGRID to define more complex antennas). Furthermore, the radiation pattern cards generated are only for cross sections

defined by angles of constant azimuth or elevation angles of the full three dimensional patterns. Since it is fairly easy to enter the control statements into the NEC2 input file by hand, only these very common type of requests are catered for by WIREGRID.

Any additional command lines or alterations to the geometry data may be added afterwards, with the user's editor of choice. For this purpose, the following information on the structure of the geometry data section is important:

- Each tag number in the file refers to the number of the major element wherein the wire segment is located. This means that wire segments belonging to major elements defined by more than two major nodes do not have unique tag numbers, and cannot be referred to by the control statements at the end of the file, unless the tag number is changed by the user afterwards. This is also the reason why WIREGRID only allows excitation of segments in two-node major elements in its control statement generation options.
- Geometry data for the polygonal boundaries (yellow²) between the major elements are entered first into the file, starting with the boundaries of major element number 0, and then the two node elements are added.
- This is followed by data statements describing the internal meshes (where relevant). These statements are divided into sets for each polygonal major element, starting with the element with the lowest tag number. In addition, the internal mesh data statements for each polygonal major element are subdivided into a subset of statements describing long, straight, segmented wire sections (red), and a subset describing short, single segment wire sections (blue).

2.5 The user interface

Fig. 4 shows the main menu screen of WIREGRID. An option is selected by moving the cursor to the required one and hitting return. Should the wrong option be selected accidentally, hitting escape at any time while WIREGRID is prompting for input information returns the user to the main menu, without any action being taken³.

²The colours mentioned are used in the graphical display of the model (see Section 2.3).

³Editing major element coordinates, or selecting wire segments for excitation, are exceptions to this rule. In these cases hitting escape ends the editing or selecting session. An element thus incorrectly created is removed by deleting the major element.

WIRE GRID MODELLING FOR NEC

```

Load a model.
Specify nominal segment length.
Add a major element.
Edit a major element.
Delete a major element.
Edit a major node.
Translate major elements.
Rotate major elements.
Mirror major elements.
Check number of segments.
View a major element.
View model.
Save model.
Create input file for NEC.
Quit.

```

Use **<↑>** and **<↓>** to choose an option

Press **<ENTER>** to execute the option

Figure 4: WIREGRID's main menu screen

2.5.1 Creating a new model

When a new model is started, the nominal segment length must be specified before any major elements can be entered. Experience has taught many new users have problems with the code at this initial stage, not realizing that a nominal segment length is *required*. Any reasonable value suffices; as already discussed the nominal segment length can be changes at any time during the modelling process. The first major element can then be entered. If a model is already loaded, and the user wants to start a new model, it is easiest to quit and run the program again.

2.5.2 Deleting major elements

A major element is deleted by selecting the "Delete a major element" option. It is important to note that all elements with tag numbers higher than the one deleted will be assigned a new number, one less than before. When more than one element must be deleted, it is therefore best to start with the highest-numbered element and work downwards. This eliminates the need to continuously recalculate the tag number of the elements still to be deleted.

2.5.3 Adding, editing and saving models

An existing model may be loaded from disk, together with the last discretization used. The user may therefore start to edit major elements or add new ones immediately after loading.

When a new major element is defined, WIREGRID prompts for the element's number tag and the number of nodes defining the element. The default value of the latter is two, and replacing it by larger numbers (up to 10), will result in more complex elements. WIREGRID subsequently presents the user with a table of major node coordinates, with default values corresponding to the respective nodes of the previous major element⁴. The cursor is moved around in the table with the left and right tab keys, and with the up and down arrow keys, to edit the various coordinates. Coordinate editing is followed by specification of the end point radii for two-node major elements. (The default radius of $\ell_n/2\pi$ has already been discussed in Section 2.2).

The default values for the latter is $\ell_n/2\pi$, the value used for the polygonal major element wire sections at that stage. (This is of course probably wrong, since two-node element frequently represent wire antennas, but it is trivial to enter the correct radius).

Editing an existing major element is the same as defining a new one, except that the default values for the number of nodes, coordinates and end point radii, are the actual values specified previously.

Models can be combined by loading an existing model from disc at any time and merging it with the current one in memory, helping the user to model the structure in an organized and structured fashion. An example would be the hull and turret of a ground vehicle, which are conveniently modelled separately and then combined. When the models are merged, WIREGRID ensures that elements from the different models with common edges are correctly picked up, ensuring that the mesh is properly conformal.

A range of subsequent major elements may be spatially translated by adding a vector to all coordinates involved. Alternatively, they can be rotated around an axis (specified by the user as a line through two three-dimensional Cartesian points) by a certain angle, or mirrored in a plane (specified by the user as the spherical coordinate vector from the origin to the nearest point on the plane surface). In the process the elements can be effectively moved to these new positions, or new elements can be created in this way. This helps the user to build up structures with symmetrical properties fairly quickly. Note that these "Translate", "Mirror" and "Rotate" options do not generate associated structure geometry lines (GM, GX, GR - "cards" respectively) [9, p. 16] in the NEC2

input file, but physically generate new or altered major elements.

The model can be saved at any stage by specifying an appropriate file name. It is recommended that this be done often, since a major element may be accidentally deleted, or an unforeseen run-time error may occur. The latter is unfortunately not infrequent, since it is very difficult to foresee all errors that may occur, in particular with incorrect user input. Provided that the model has been recently saved, it is simple to reload WIREGRID, load the model and then continue building the model.

2.5.4 Entering numbers

When typing in a number, or editing one, the **Backspace**, **Delete** and the **Left** and **Right** arrow keys can be used in the usual manner. The default editing mode is always the "Insert" mode, but it can be toggled to the "Over-write" mode with the **Insert** key. **Ctrl + Left** or **Right** arrows will move the cursor to the end or beginning of the number being edited.

2.5.5 Inspecting the model

The entire model can be inspected at any time by selecting the "View model"-option, or a single major element may be inspected by selecting the "View a major element"-option instead.

The boundaries of the major elements are displayed in yellow, while wires generated by the discretizer are displayed in red and blue. These have been discussed in §2.3.

The view of the model can be changed by zooming in or out with the + and - keys, by rotating it with the arrow keys, and by translating it sideways or up and down with the L, R, U, and D keys.

Any major element can be highlighted by hitting **S** and specifying the major element number. When viewing a single major element, this can be used to add other major elements to the picture. This feature is the only one that does not work with a monochrome graphics adapter, since the highlighted (white) colour cannot be distinguished from the other colours.

2.5.6 Excitation of wire segments

In the final generation of the NEC2 input file, the user may specify the excitation of some wire segments for maximum coupling computation and radiation pattern generation (see Section 2.4).

For maximum coupling calculations, up to five segments may be excited, and for an antenna array pattern calculation, up to ten segments may be excited.

⁴This eliminates to a certain extent the need to retype node coordinates common to the previous element.

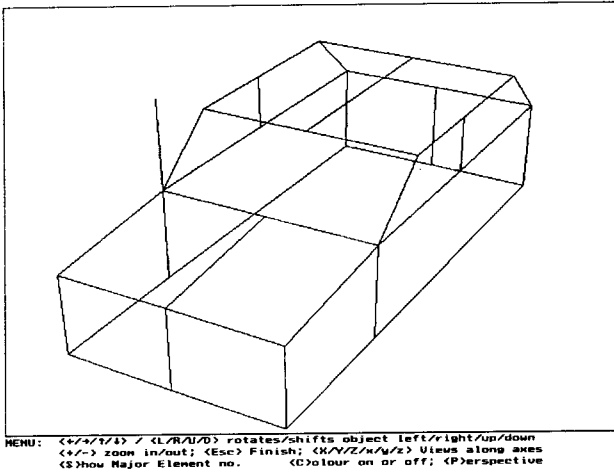


Figure 5: A passenger motor car showing only the major elements. There are 41 segments in this model. The model was generated using symmetry, hence the wires on the centreline.

A list of selected segments (specified by their major element tag number, and the segment number⁵) is shown near the top of the computer screen. Below that, information on all two-node major elements is displayed for one element at a time, while the user is “paging through” the list with the left and right arrow keys. In order to select a wire segment, the user “pages” to the particular two-node major element, and increments or decrements the segment number with the up and down arrow keys. The insert key is finally used to select a segment for excitation, whereupon WIREGRID will prompt for the excitation voltage, and the segment will be added to the list of excited segments. The delete key is used to remove segments from this list.

We have found from experience that users often have trouble using this particular feature of WIREGRID, partly because there is no visual feedback to confirm the location of the sources. Since it is relatively easy to manually append the necessary source commands to the NEC2 input deck created by WIREGRID, many users elect to do this.

2.6 An example

In Figures 5 and 6 we show the WIREGRID mesh for a motor vehicle, very similar, although not identical, to the generic hatchback shown in Figure 1.

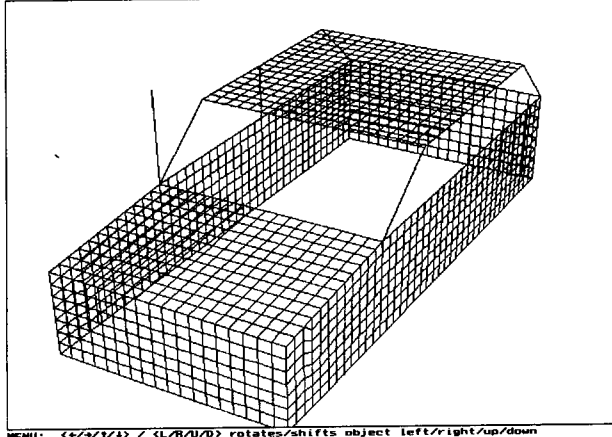


Figure 6: The same passenger motor car with a nominal segment length of $0.1m$. (Using the $\lambda/10$ rule, this model would be valid up to around 300 MHz). The number of segments is now 3008. It must be emphasized that only one key stroke was required to generate this mesh from the model shown in Figure 5. Note that the code does not do hidden line removal. (A very powerful computer would be required to *run* this model: the discretization shown here is to emphasize the capabilities of WIREGRID).

3 Conclusions

We have found that WIREGRID has greatly boosted our productivity for generating NEC2 input decks for simulations involving wire mesh modelling. WIREGRID has a number of limitations, many of which we have outlined in this paper, but there are some other *fundamental* limitations that potential users should be aware of. WIREGRID does *not* check the validity of the structures that it generates with respect to all the NEC2 model generation rules — admirably summarized by Trueman and Kubina [2]. Particularly when the structure involves thin triangular elements, it is quite possible that the WIREGRID mesh may violate some of the validity conditions. Of course, its output could easily be run through such a validity checker, but at the time of writing, Trueman and Kubina’s code, CHECK, is still not generally available due to export restriction problems. We would like to extend WIREGRID to incorporate at least some of these validity checks. We would also like to add a facility to read in and display NEC2 data decks in WIREGRID; it does not presently have such a facility. However, funding for this work is very restricted at present and neither facility is likely to be implemented in the near future. Finally, while we have found the user interface to be very functional, it does not have the latest Windows-style icons, dialogue boxes, hot-keys etc.

⁵Segment numbers start at 1, denoting the segment joined to node 0.

4 Acknowledgements

The authors would like to thank the many users at Stellenbosch and in South Africa who have helped to test the code for their comments and suggestions. D.H.Malan implemented the upgrades described in the appendix "Recent Improvements".

References

- [1] S. J. Kubina and C. Larose, "A NEC topside antenna case study with Didec and Spectrum: model generation and current display codes," *ACES Newsletter*, vol. 1, no. 2, pp. 47-52, 1986.
- [2] C. W. Trueman and S. J. Kubina, "Verifying wire-grid model integrity with program 'CHECK,'" *ACES Journal*, vol. 5, pp. 17-42, Winter 1990.
- [3] R. K. Najm, "Simplified 3-D mesh generator," *ACES Journal*, vol. 6, pp. 86-98, Winter 1991.
- [4] A. P. C. Fourie, D. C. Nitch, and O. Givati, "A complex-body structure interpolation and gridding program (SIG) for NEC," *IEEE Antennas Propagat. Magazine*, vol. 36, pp. 85-89, June 1994.
- [5] D. B. Davidson, "PARNEC," *IEEE Trans. Antennas Propagat. Magazine*, vol. 34, pp. 39-40, April 1992. In "PCs for AP and other EM Reflections" column, edited by E. K. Miller.
- [6] D. B. Davidson, "Parallel processing revisited: a second tutorial," *IEEE Antennas Propagat. Magazine*, vol. 34, pp. 9-21, October 1992.
- [7] D. B. Davidson and C. F. du Toit, "Recent progress with PARNEC and the pre-processor WIREGRID," in *Proceedings of the 1991 IEEE/SAIEE Joint AP-MTT Symposium*, pp. 242-249, August 1991. Held in Fourways, Johannesburg, South Africa.
- [8] A. C. Ludwig, "Wire grid modelling of surfaces," *IEEE Trans. Antennas Propagat.*, vol. AP-35, pp. 1045-1048, September 1987.
- [9] G. J. Burke and A. J. Poggio, "Numerical Electromagnetics Code (NEC) - Method of Moments; Part III: User's Guide." January 1981.

Appendices

A Obtaining and Installing the Code

The code is available on the NEC Archives ftp site. The ftp site name is `ftp.netcom.com`, and the code is in

`pub/rander/NEC` directory as `wiregrid.zip`. The code was compressed using the widely used DOS shareware utility PKZIP; use PKUNZIP to decompress. Details on downloading codes from anonymous ftp sites may be found in any of the many guides to the Internet now appearing. To summarize, proceed as follows:

- Enter `ftp ftp.netcom.com`
- The system will respond with `Name:` (or similar message); reply with `anonymous`.
- The system will then prompt for a password; it is customary to enter your Internet (e-mail) address.
- Enter `cd /pub/rander/NEC`.
- then `binary` (this is actually the default for this site).
- and finally get `wiregrid.zip`.
- To exit the ftp session, `quit`.

There may be an appreciable delay (possibly a number of seconds) between entering a command and obtaining a response, especially if you are accessing the site from outside the USA. South African users should note that `wiregrid.zip` is mirrored on our local Stellenbosch ftp site, viz. `ftp.sun.ac.za`, and should download from this site in preference to `ftp.netcom.com`.

If PKUNZIP cannot unzip the file, check that you have a sufficiently recent version (the index entry for WIREGRID details the version used); if this is not the problem, you may have done a ftp transfer in ASCII mode en route to your PC. Your local Internet guru will be able to advise!

For installation, all files on the distribution disk should be copied to a directory of the user's choice. When `wiregrid.exe` is run, it will prompt for the directories where the wire grid models and the NEC2 input files are to be stored respectively. Several example files are included with the `zip` file. The user may change these directories during a session, and these changes then become the defaults for the next session. Whenever a directory which does not exist is specified, it will be created on request.

B Hardware requirements

WIREGRID.EXE runs under DOS on an IBM compatible PC. The program is written in TurboPascal, and makes extensive use of the TurboPascal graphics calls. As a result, it will unfortunately *not* be a simple matter to port to another hardware platform using

a different operating system (such as an Apple Macintosh). Although a 8087/80287/80387 mathematical co-processor would be advantageous, it is not a prerequisite. (The code automatically detects the presence of a co-processor). A colour graphics adapter and a colour display monitor (or a monochrome display which can differentiate between colours using various shades of grey) are required to fully exploit the graphical features of WIREGRID, but almost all of these will still work satisfactorily with a monochrome graphics adapter. WIREGRID supports the CGA, EGA, IBM8514, Hercules, ATT400, VGA and the PC3270 graphics adapters.

C Recent Improvements

This paper describes WIREGRID Version 3. The latest version, 4.00, incorporates some useful new features for viewing the model. These are :

- The model can now be plotted as if viewed along one of the three axes, X , Y or Z . (Actually, there are six, not three, options here, since x and X rotate the view by 180° .)
- The user can now toggle perspective on and off. The default is to show the model in perspective, but there are cases where it is more convenient to remove this facility, such as when the model is viewed along an axis.
- The display can now be switched to monochrome mode on colour screens. (There is no effect on monochrome screens). This is useful for doing screen-prints and screen-captures; for example, the screen-capture utility that was used to generate Figures 5 and 6 in this paper produces satisfactory images from a monochrome display, but not from a coloured one.

D Further Information

Users are welcome to contact the second author at the address given on this paper to report bugs or make suggestions, but as with most public domain software, we unfortunately cannot offer extensive user support. This paper serves as the user manual at present; no further documentation is available.

The standard software disclaimer applies: no warranty is given or implied that all errors have been eliminated from the program WIREGRID, and the authors and the University of Stellenbosch accept no responsibility for any losses, damages etc. resulting from the use of the program.

The authors

Cornelis (Nelis) F. du Toit was born in South Africa on May 3, 1962. He received the B.Eng., M.Eng. and Ph.D. from the University of Stellenbosch in 1984, 1986 and 1992 respectively. His doctoral dissertation was entitled "The computation of electromagnetic fields from cylindrical near-field measurements at non-asymptotic distances from an antenna". He was a Research Assistant at the University from 1988-1992, and worked at Plessey-Tellumat in Cape Town during 1993 as a contractor. Nelis and his family moved to New Zealand in January 1994, and he is presently working for DelTec in Wellington. The work reported in this paper was performed whilst Nelis was at the University of Stellenbosch. His research interests include electromagnetic field theory, antenna design, near-field measurement techniques and numerical methods in antenna engineering. Nelis is a keen amateur astronomer and an accomplished pianist; he also enjoys listening to music. Nelis is married to Elize (a musician) and they have one child.

David B. Davidson (IEEE Member) was born in London, England on April 13, 1961. He grew up in South Africa. He received the B.Eng., B.Eng. (Honours) and M.Eng. degrees (all cum laude) from the University of Pretoria in 1982, 1983 and 1986 respectively, and in 1991 he received the Ph.D. degree from the University of Stellenbosch. His Ph.D. dissertation was entitled "Parallel algorithms for electromagnetic moment method formulations". David is presently an Associate Professor of Electrical and Electronic Engineering at the University of Stellenbosch, where he started teaching in 1988 following three years as a research engineer at the national research laboratories. His research interests centre around computational electromagnetics — theory, code development and applications — and include the application of parallel processing to this field; the work reported here was closely linked to his work on a parallel version of NEC2. He has worked with both transputer arrays for moment method codes and the CM-2 for FDTD codes. He recently spent six months as a visiting scholar at the University of Arizona, Tucson, AZ, working on applying computational electromagnetics methods to optical device modelling. In his spare time he climbs mountains, builds models, board-sails, plays tennis or squash or listens to music. David is unmarried.

A GUIDE TO IMPLEMENTATIONAL ASPECTS OF THE SPATIAL-DOMAIN INTEGRAL EQUATION ANALYSIS OF MICROSTRIP ANTENNAS

Louis T. Hildebrand & Derek A. McNamara¹

*Electromagnetism Group, Department of Electrical & Electronic Engineering
University of Pretoria, Pretoria, South Africa 0002*

Abstract: *In the analysis of microstrip radiating structures integral equation methods rate among the more accurate approaches. By far the most demanding part in the use of these methods is the actual numerical implementation. This paper presents a detailed illustrated description of the numerical implementation of a spatial domain mixed-potential integral equation analysis of microstrip radiating structures.*

1. INTRODUCTION

In the analysis of microstrip radiating structures integral equation methods rate among the more accurate approaches. The most widely used is the "full-wave" electric field integral equation (EFIE). When both vector and scalar potentials are used in the formulation of the EFIE, it is often referred to as the mixed-potential integral equation (MPIE). There have been two paths followed in the implementation of the integral equation methods to microstrip geometries; these can be classified according to the manner in which the somewhat cumbersome Green functions appropriate to the problem are dealt with numerically in the moment method solution of the integral equation. In both cases one starts with a Green function derived in analytical form in the spectral domain. Expressions for the moment method matrix elements are then established, consisting of three double integrals, over the spectral domain, domain of the testing functions, and domain of the expansion functions for the unknown current-density, respectively. It is in the evaluation of this expression that two different approaches are used. In the full-wave spatial domain approach this is done by carrying out the integration with respect to the spectral variables numerically in order to convert the Green function to spatial domain form, and then proceeding further with the other two integrations. In the full-wave spectral domain approach, the expression for the moment method matrix elements is manipulated in

such a way that it becomes one consisting of two-dimensional spatial Fourier transforms of the expansion and testing functions (and this can usually be done in closed form) whose product with the original spectral domain Green function must be integrated in the spectral domain. In both cases the moment method solution provides the expansion coefficients of the unknown current-density directly in the spatial domain of course. An exposition of the difference between the two approaches is given by Pozar [1, Sect. IV, Part B].

Published information on the application of the integral equation approaches (no doubt in order to satisfy the space restrictions associated with journal articles) essentially takes the form of some useful suggestions on how to overcome numerical difficulties, but has to stop short of the details needed for a direct implementation of the analysis in a code. This is unfortunate since by far the most demanding part in the use of integral equation analyses for microstrip antenna problems is the actual numerical implementation. One does not always want to ask others directly for their computer codes since these are often not available for distribution for proprietary reasons, or the codes are directly related to the livelihood of the developer who has for this reason invested a considerable amount of time in its development (and this is quite understandable). This paper therefore presents a detailed illustrated description of the numerical implementation of the MPIE analysis of Mosig and Gardiol [2], hereafter simply referred to as *the MPIE formulation*; it is our experience that the discussion on implementation given in [2,3] is the most detailed available in the literature at present. We include the information we would have liked to have had available when we began implementing the techniques of [2,3]. It will be assumed that the reader has references [2], [3] and [4] at hand, although matters will be summarised in Section 2.

¹ D.A. McNamara was with the University of Pretoria. He is now with COM DEV Ltd, 155 Sheldon Drive, Cambridge, Ontario, N1R 7H6, Canada

2. BRIEF OVERVIEW OF THE INTEGRAL EQUATION MODELLING SCHEME

Since the Green functions forming the kernel of the integral equation are those for a horizontal electric current element (at $z=0$) in the presence of a grounded dielectric slab, the only unknowns are the current/charge-densities on the etched conductors. The integral equation is obtained by "replacing" the etched conductors by an equivalent surface current-density $\mathbf{J}_s(x, y, 0)$ and enforcing the boundary condition that the total tangential electric field at all points on the slab surface occupied by these conductors be set equal to $Z_s(\hat{\mathbf{z}} \times \mathbf{J}_s)$, where Z_s is the surface impedance of the conducting material. The validity of using the surface impedance concept has been carefully studied by Theron and Cloete [5]. These integral equations are expressed in terms of vector and scalar potentials $\mathbf{A}(x, y, 0)$ and $\Phi(x, y, 0)$, respectively, and thus the Green functions used are those associated with these potentials, namely \mathbf{G}_A and \mathbf{G}_V , as described in [2]. A method of moments procedure with sub-sectional expansion and testing functions is used to solve the MPIE, with overlapping rooftop functions in both the x and y directions selected for the expansion functions of the surface current-density. These are placed as follows: the surface of the etched conductor is divided into elementary charge-density cells, with two adjacent charge-density cells forming a current-density cell. Figure 1(a) shows two charge-density cells. The current-density is represented by overlapping rooftop expansion functions. So-called razor test functions, shown in Figure 1(b), which extend along segments linking the centres of adjacent charge-density cells, are used. Although not a fundamental limitation of the technique, we have here arranged matters so that the antenna structure must be segmented into rectangular cells of *equal size*; this simply eases some of the already substantial computational burden.

3. THE DISCRETISED (MATRIX) FORM OF THE INTEGRAL EQUATION

Let there be M of the x -directed rooftop functions, and N of the y -directed ones. Their introduction, along with the razor testing functions extending from the centres of two adjacent charge cells (that is, along C_{xj} in Figure 1), converts the integral equation to the matrix equation $[\mathbf{C}][\mathbf{I}] = [\mathbf{V}]$ which is written [3,4] in terms of sub-matrices as

$$\begin{pmatrix} \mathbf{C}^{xx} & \mathbf{C}^{xy} \\ \mathbf{C}^{yx} & \mathbf{C}^{yy} \end{pmatrix} \begin{pmatrix} \mathbf{I}_x \\ \mathbf{I}_y \end{pmatrix} = \frac{1}{jZ_0} \begin{pmatrix} \mathbf{V}_x^{(e)} \\ \mathbf{V}_y^{(e)} \end{pmatrix} \quad (1)$$

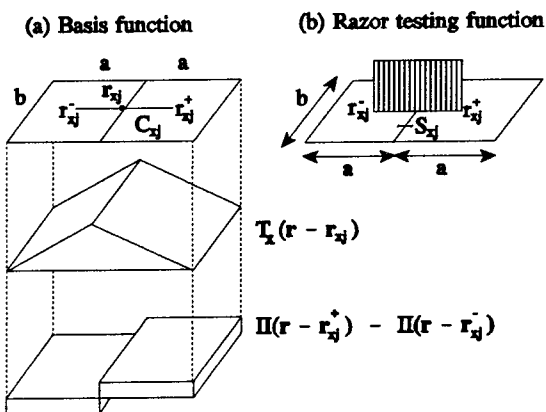


Figure 1 X-directed current cell with a rooftop basis function and razor testing function. The associated charge distribution over the current cell is also shown.

Here the \mathbf{C}^{xx} , \mathbf{C}^{xy} , \mathbf{C}^{yx} and \mathbf{C}^{yy} are sub-matrices of size $M \times M$, $M \times N$, $N \times M$ and $N \times N$, respectively. Thus matrix $[\mathbf{C}]$ is of size $(M+N) \times (M+N)$. The elements of the sub-matrices are given by [3,4]

$$\begin{aligned} C_{ij}^{xx} = & \frac{1}{k_0 a k_0 b} \left[-\Gamma_V(r_{xi}^+ | r_{xj}^-) - \Gamma_V(r_{xi}^- | r_{xj}^+) \right. \\ & \left. + \Gamma_V(r_{xi}^+ | r_{xj}^+) + \Gamma_V(r_{xi}^- | r_{xj}^-) \right] \\ & - \frac{1}{k_0 b} \int_{C_{xj}} \Gamma_A^{xx}(r | r_{xj}) k_0 dx + j \frac{Z_s}{Z_0} \frac{a}{b} \delta_{ij} \end{aligned} \quad (2)$$

$$i = 1 \dots M, j = 1 \dots M$$

$$\begin{aligned} C_{ij}^{xy} = & \frac{1}{k_0 a k_0 b} \left[-\Gamma_V(r_{xi}^+ | r_{yj}^-) - \Gamma_V(r_{xi}^- | r_{yj}^+) \right. \\ & \left. + \Gamma_V(r_{xi}^+ | r_{yj}^+) + \Gamma_V(r_{xi}^- | r_{yj}^-) \right] \end{aligned} \quad (3)$$

$$i = 1 \dots M, j = 1 \dots N$$

In the above, Z_0 is the free space characteristic impedance, k_0 the free space wavenumber and δ_{ij} the Kronecker delta. The Z_s is a surface impedance accounting for the finite conductivity as well as surface roughness and finite thickness of the metallic upper conductor [3]. An expression for C_{ij}^{yy} is obtained by interchanging the couples (x, y) , (a, b) and (M, N) within the expression for C_{ij}^{xx} ; reciprocity requires that for cells of equal size $C_{ij}^{yx} = C_{ji}^{xy}$.

\mathbf{I}^x and \mathbf{I}^y are column sub-vectors of size $M \times 1$ and $N \times 1$, respectively. Their elements are the

coefficients of the x-directed and y-directed expansion functions for the current-density. The excitation column sub-vectors $V_x^{(e)}$ and $V_y^{(e)}$ are similarly of size $M \times 1$ and $N \times 1$, respectively. Thus the column vectors $[I]$ and $[V^{(e)}]$ are both of size $(M+N) \times 1$.

The precise expression for the elements of $[V]$ depends on the type of excitation geometry being considered. Here a coaxial probe feed will be considered for which a simple, yet sufficiently accurate model was introduced in [3]. This model assumes that the current on the coaxial probe is constant and is therefore only accurate for thin substrates (up to about $\lambda/10$ thick). According to this model the excitation current spreads over a single charge cell as described by the following expression:

$$\begin{aligned} J_x &= \hat{x} \frac{I}{4b} \operatorname{sgn}(x) \left(1 - \frac{2|x|}{a} \right) \\ &+ \hat{y} \frac{I}{4a} \operatorname{sgn}(y) \left(1 - \frac{2|y|}{b} \right) \end{aligned} \quad (4)$$

More complex feed models valid for thick substrates are discussed in [6]. The associated excitation surface charge-density distribution over the charge cell is given by a rectangular pulse of value $I/jwab$ where I is the total current carried by the inner coaxial conductor. Figure 2 gives an illustration of the electric surface current-density and charge-density distributions associated with the coaxial probe feed model; note that only the x-directed component is shown in the figure for the sake of clarity. It has been found [7] that the contribution of the excitation *current* (as opposed to the *charge*) to $V^{(e)}$ can usually be neglected; otherwise it must be computed from the expression for Γ_A^{xx} (Γ_A^{yy}) given in (8) with J_{ex} (J_{ey}) replacing T_x (T_y). If we recognise that the matrix elements according to (3) represent the effect of a charge doublet (Figure 1) integrated along a test segment, then since with the above coaxial probe model the excitation is a single pulse of charge (Figure 2), the elements of the excitation vector may be seen to be approximated by [7]

$$V_{xi}^{(e)} \approx \frac{Z_0}{jk_0 a k_0 b} [\Gamma_V(r_{xi}^+ | r) - \Gamma_V(r_{xi}^- | r)] \quad (5)$$

$$V_{yi}^{(e)} \approx \frac{Z_0}{jk_0 a k_0 b} [\Gamma_V(r_{yi}^+ | r) - \Gamma_V(r_{yi}^- | r)]$$

where feedpoint r is located at the centre of a charge cell. The moment method matrix C is ill-conditioned due to the fact that some rows are almost linear combinations of three other rows. Therefore careful evaluation of its elements is necessary to obtain results of sufficient accuracy. On the other hand, C is diagonally dominant, therefore less stringent accuracy requirements apply to the off-diagonal elements. Certain approximations may then be considered. One of these approximations involves the integral term in (2) which may be approximated as follows:

$$\int_{C_{xi}} \Gamma_A^{xx}(r | r_{xi}) k_0 dx \approx k_0 a \Gamma_A^{xx}(r_{xi} | r_{xi}) \quad (6)$$

The validity of this approximation is illustrated in Figures 3 and 4 showing the real and imaginary parts, respectively, of both terms in (6). In fact, this approximation may even be considered for the diagonal elements, since the contribution of the vector potential to the value of the matrix element is overshadowed by that of the scalar potential [7]. A conjugate gradient method [8] is used for the iterative solution of the moment method matrix equation.

In (2), (3) and (5) Γ_A^{xx} and Γ_V are *discrete Green functions* (not to be confused with the Green functions themselves) which have as sources complete basis functions as opposed to conventional elementary point sources. $\Gamma_A^{xx}(r | r_j)$ is then the x-component of the vector potential at r created by an x-directed rooftop distribution of surface current at r_j , whereas $\Gamma_V(r | r_{oj})$ is the scalar potential at the same observation point resulting from a rectangular distribution of unit surface charge at r_{oj} . The discrete Green functions are now defined by the following dimensionless expressions [3]:

$$\Gamma_V(r | r_{oj}) = \int_{S_{oj}} \frac{\epsilon_0}{k_0} G_V(r | r') \Pi(r' - r_{oj}) k_0^2 dS' \quad (7)$$

$$\Gamma_A^{xx}(r | r_{xi}) = \int_{S_{xi}} \frac{1}{\mu_0 k_0} G_A^{xx}(r | r') T_x(r' - r_{xi}) k_0^2 dS' \quad (8)$$

where μ_0 and ϵ_0 are the permeability and permittivity of free space. A similar expression to that given in (8) holds for Γ_A^{yy} . S_{xi} represents the surface of the current source cell centred at r_{xi} (Figure 1) while the charge source cell centred at r_{oj} extends over S_{oj} . Π is a two-dimensional unit pulse function over S_{oj} and

$T_x(r) = 1 - |x|/a$ over S_x . The Green functions appearing in the above expressions for the discrete Green functions, are given by the following expressions:

$$G_V(r|r') = \frac{1}{2\pi\epsilon_0} \int_0^\infty J_0(\lambda R) \frac{\lambda N}{D_{TE} D_{TM}} e^{-\mu_0 \lambda} d\lambda \quad (9)$$

$$G_A^{xx}(r|r') - G_A^{yy}(r|r') = \frac{\mu_0}{2\pi} \int_0^\infty J_0(\lambda R) \frac{\lambda}{D_{TE}} e^{-\mu_0 \lambda} d\lambda \quad (10)$$

where J_0 is the Bessel function of zero'th order and first kind, $D_{TE} = u_0 + u \coth(uh)$, $D_{TM} = \epsilon_r u_0 + u \tanh(uh)$ and $N = u_0 + u \tanh(uh)$; $u_0 = (\lambda^2 - k_0^2)^{1/2}$, $u = (\lambda^2 - \epsilon_r k_0^2)^{1/2}$, h is the substrate thickness and $R = |\mathbf{r} - \mathbf{r}'|$. For the case of a lossy dielectric, $\epsilon_r = \epsilon_r'(1 - j \tan \delta)$ where $\tan \delta$ is the loss tangent. Figure 5 illustrates the effect of the distance between source and observer (R) on the Green function integrands; the real part of the normalised G_A^{xx} integrand is shown for $R = 0.5\lambda_0$ and $0.05\lambda_0$. It can be seen that when the observer (\mathbf{r}') approaches the source point (\mathbf{r}), the zero's of the integrand move away from the origin. In the limiting case ($R = |\mathbf{r} - \mathbf{r}'| \rightarrow 0$) the first zero tends to infinity, producing a non-oscillating, non-zero function to be integrated over a semi-infinite interval. This produces the singularities in the Green functions at the source point. Now, in the evaluation of the discrete Green functions the situation arises where the observation point \mathbf{r} for the potential due to a particular source cell falls within its own source cell boundaries. For this reason the integrands for the discrete Green functions are singular at \mathbf{r} due to the Green functions becoming singular. This situation is illustrated in Figures 6 and 7. We will call any evaluation of the potential due to a given source cell at any point in its own source cell a "self term". By now writing (7), in the evaluation of the self term, as

$$\Gamma_V(r_{oj}|r_{oj}) = \epsilon_0 k_0 \int_{S_{oj}} [G_V(r_{oj}|r') - G_{Vs}(r_{oj}|r')] dS' + \Gamma_{Vs}(r_{oj}|r_{oj}) \quad (11)$$

where an expression for $\Gamma_{Vs}(r_{oj}|r_{oj})$ is given in [3] and

$$G_{Vs}(r_{oj}|r') = \frac{1}{2\pi(\epsilon_r + 1)\epsilon_0 |r_{oj} - r'|} \quad (12)$$

it is possible to evaluate the scalar potential discrete Green function self term since the difference term in (11) is numerically integrable as illustrated in Figures 8 and 9. Even though the difference term is well-behaved at $\mathbf{r}' = \mathbf{r}_{oj}$ both terms comprising the difference term, i.e. G_V and G_{Vs} , become singular. The evaluation of the difference term at the source point is therefore done as follows: $G_V(r_{oj}|r_{oj} + \delta) - G_{Vs}(r_{oj}|r_{oj} + \delta)$ where $\delta \rightarrow 0$. In this way an accurate estimate of the well-behaved difference term may be obtained at the source point. In similar fashion the singularity in the real part (the imaginary part of the Γ_A^{xx} integrand does not exhibit singular behaviour even in self term evaluations) of the vector potential discrete Green function may be dealt with. In this case, however, an expression for Γ_{Vs}^{xx} could not be found in the literature, however, analytical integration yields:

$$\begin{aligned} \Gamma_{Vs}^{xx}(r_x|b) = & \frac{k_0}{2\pi} (a - r_x) \ln \tan \left(\frac{\alpha_1 + \pi}{2} \right) \\ & + \frac{k_0 b}{4\pi} \ln \left[\frac{\tan \left(\frac{\pi}{2} - \frac{\alpha_2}{2} \right)}{\tan \left(\frac{\alpha_1}{2} \right)} \right] + \frac{k_0 (a + r_x)}{2\pi} \ln \tan \left(\frac{\alpha_2 + \pi}{2} \right) \\ & - \frac{k_0 a}{4\pi} \ln \tan \left(\frac{\alpha_2 + \pi}{2} \right) + \frac{k_0 b^2}{16\pi a} [\cosec(\alpha_3) - \cosec(\alpha_2)] \\ & - \frac{k_0 r_x^2}{4\pi a} \ln \tan \left(\frac{\alpha_2 + \pi}{2} \right) + \frac{k_0 b^2}{16\pi a} [\cosec(\alpha_3) - \cosec(\alpha_1)] \\ & - \frac{k_0 (a - r_x)^2}{4\pi a} \ln \tan \left(\frac{\alpha_1 + \pi}{2} \right) + \frac{k_0 r_x b}{4\pi a} \ln \left[\frac{\tan \left(\frac{\alpha_3}{2} \right)}{\tan \left(\frac{\alpha_2}{2} \right)} \right] \end{aligned}$$

$$\begin{aligned}
 & -\frac{k_0 r_x}{2\pi a} (a - r_x) \ln \tan\left(\frac{\alpha_1}{2} + \frac{\pi}{4}\right) \\
 & -\frac{k_0 r_x b}{4\pi a} \ln \left[\frac{\cot(\frac{\alpha_3}{2})}{\tan(\frac{\alpha_1}{2})} \right]
 \end{aligned} \quad (13)$$

where $\alpha_1 = \tan^{-1}[b/(2(a-r_x))]$, $\alpha_2 = \tan^{-1}[b/(2(a+r_x))]$ and $\alpha_3 = \tan^{-1}[b/(2r_x)]$. This expression was derived for an x-directed current cell centred at (0,0) with an observer on the source cell at \hat{x}_x . Therefore, numerical techniques required in the self term evaluation of both the discrete Green functions have now been discussed. For the off-diagonal matrix elements approximations for the discrete Green functions were suggested by Mosig and Gardiol [3]. It is worth mentioning that these approximations have also been implemented successfully by the present authors.

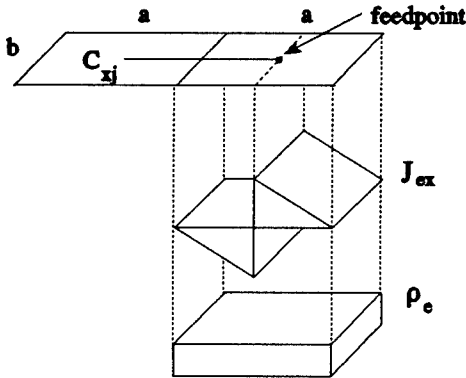


Figure 2 Electric surface current and charge distributions associated with the coaxial probe feed model.

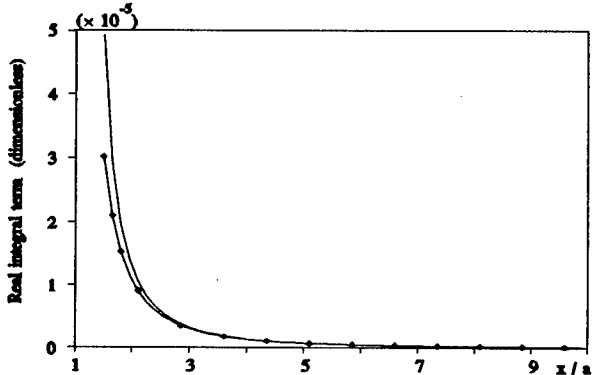


Figure 3 Real parts of the actual integral (—) and approximation (6) (—◇—◇—) suggested by Mosig and Gardiol [1]; $f=1.206$ GHz, $\epsilon_r=4.34-j0.0868$; $h=0.8$ mm and $a=b=6.666$ mm.

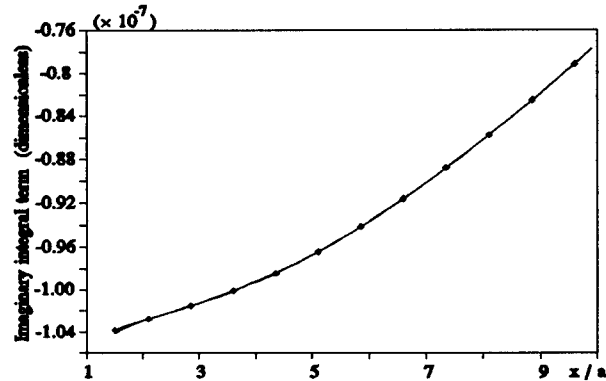


Figure 4 Imaginary parts of the actual integral (—) and approximation (6) (—◇—◇—) with the corresponding real part shown in Figure 3.

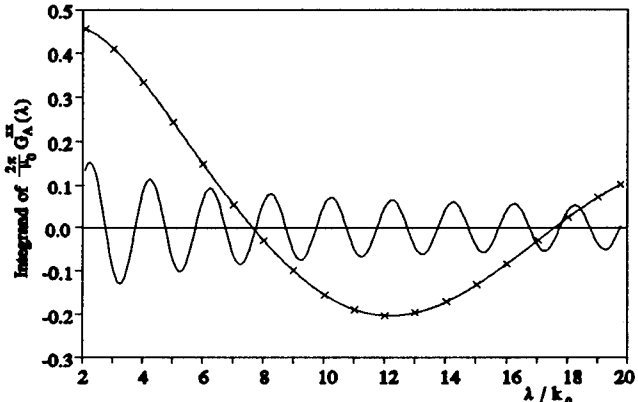


Figure 5 Normalised integrand of $G_A^{xx}(r/r')$ for $R/\lambda_0=0.5$ (—) and $R/\lambda_0=0.05$ (—×—×—) where $h/\lambda_0=0.07$ and $f=1.206$ GHz

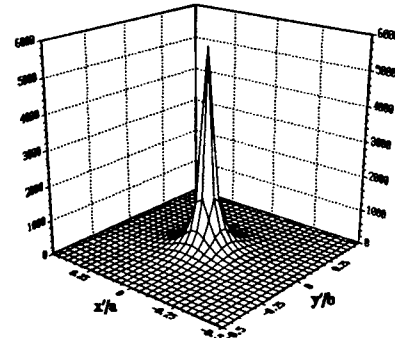


Figure 6 Real part of the integrand, before pole extraction, in the expression for the Γ_v selfterms.

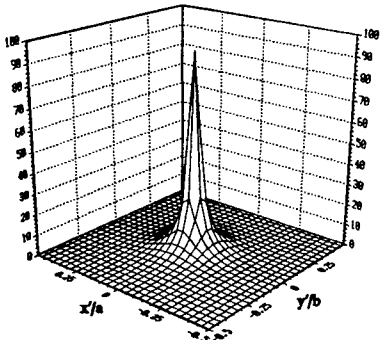


Figure 7 Imaginary part of the Γ_V integrand corresponding to Figure 6. Note that the maximum value is infinite.

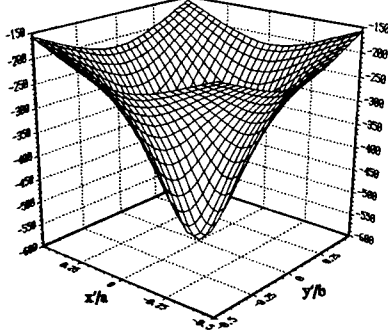


Figure 8 Real part of the difference term integrand in the evaluation of the Γ_V selfterm.

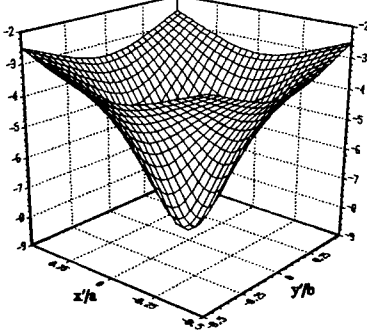


Figure 9 Imaginary part of the difference term integrand corresponding to the real part shown in Figure 8.

4. DETAILED ILLUSTRATION AND DISCUSSION OF THE NUMERICAL EVALUATION OF THE ASSOCIATED INTEGRALS

We next consider the evaluation of the Green functions. Figure 10 shows the integrand of $(2\pi/\mu_0)G_A^{xx}$ as a function of λ/k_0 at 1.206 GHz for $\epsilon_r = 4.34 - j0.0868$, and the particular circumstances $h/\lambda_0 = 0.07$ and $R/\lambda_0 = 0.5$ (λ_0 is the free space wavelength). The scalar potential counterpart, i.e. the integrand of $2\pi\epsilon_0 G_V$ as a function of λ/k_0 , is shown in

Figure 11. As seen from these figures, discontinuous derivatives, singularities and oscillations in the Green function integrands pose distinct problems, complicating the use of numerical integration techniques. Mosig and Gardiol [9] therefore suggested that the semi-infinite integration intervals in (9) and (10) be subdivided, allowing these problems to be addressed separately. For convenience, the Green function integrals are written as

$$\int_0^{\infty} F(\lambda) d\lambda = \int_0^{k_0} F(\lambda) d\lambda + \int_{k_0}^{k_0\sqrt{\epsilon_r}} F(\lambda) d\lambda + \int_{k_0\sqrt{\epsilon_r}}^{\infty} F(\lambda) d\lambda \quad (14)$$

The numerical difficulties in the evaluation of the Green function integrands in each of these sub-intervals will now be discussed, and the use of proposed solutions illustrated.

4.1 Interval $\lambda \in [0, k_0]$

The term $u_0 = (\lambda^2 - k_0^2)^{1/2}$ appearing in the expressions for D_{TE} , D_{TM} and N introduces branch points in the Green function integrands at $\lambda = k_0$. Manifestations thereof are the discontinuities in the derivatives seen at $\lambda = k_0$ (Figures 10 and 11). Standard numerical integration routines may be inefficient in the integration of functions with such discontinuous derivatives. To obtain accurate numerically integrated estimates for the Green functions over the first interval, Mosig and Gardiol [4] have proposed the substitution $\lambda = k_0 \cos t$. Suppose the integrands may be written as $F(\lambda)$, then this substitution implies that

$$\int_0^{k_0} F(\lambda) d\lambda = \int_0^{2\pi} F(k_0 \cos t) (-k_0 \sin t) dt \quad (15)$$

Figures 12 and 13 show $F(k_0 \cos t) (-k_0 \sin t)$ as functions of t , with F representing the integrands of $(2\pi/\mu_0)G_A^{xx}$ and $2\pi\epsilon_0 G_V$ shown in Figures 10 and 11 respectively. The integrands are found to be smooth

and easily integrable. In this way then, it is possible to deal with the effect of the branch points in the Green function integrands at $\lambda = k_0$.

4.2 Interval $\lambda \in [k_0, k_0(\epsilon_r')^{1/2}]$

Since the integrand of G_V (9) contains D_{TM} in the denominator, a singularity due to the existence of the dominant TM_0 surface wave mode, appears in the interval $[k_0, k_0(\epsilon_r')^{1/2}]$, as seen from Figure 11. According to a pole extraction technique described in [4], the $2\pi\epsilon_0 G_V$ integrand may be expanded as follows:

$$\frac{J_0(\lambda R)\lambda N}{D_{TE} D_{TM}} = F(\lambda) - [F(\lambda) - F_{sing}(\lambda)] + F_{sing}(\lambda)$$

where $F_{sing}(\lambda) = \text{Res}/[\lambda - (\lambda_p + j\nu_p)]$; Res is the residue of $F(k_p)$ (where $k_p = \lambda + j\nu$) at pole $k_{pp} = \lambda_p + j\nu_p$ ($F(\lambda)$ is a special case of $F(k_p)$). This leaves k_{pp} and Res to be determined. The present authors have used Müller's method [10] with deflation to determine k_{pp} - a root of the univariate complex function $D_{TM}(k_p)$. This method is numerically implemented in the IMSL routine ZANLY [11].

The residue may furthermore be determined as follows :

$$\text{Res} = \frac{1}{2\pi j} \oint_C F(k_p) dk_p - \frac{1}{2\pi j} \int_a^b F(k_p(t)) \frac{dk_p(t)}{dt} dt \quad (16)$$

where $k_p(t) = \lambda(t) + j\nu(t)$, $t \in [a, b]$ and C is any closed path around the pole at k_{pp} . A condition, however, is that function $F(k_p)$ must be analytic inside C except at k_{pp} [12]. Since C may be represented by any closed path around k_{pp} , it is convenient to choose a circle. Then we have $\lambda(t) = r\cos(t)$ and $\nu(t) = r\sin(t)$ as the parametric equations; $t \in [0, 2\pi]$ and r the radius of the circle. The value of r is not important, provided $F(k_p)$ is analytic inside the borders of the circle except at k_{pp} . Figure 14 shows the normalised distance $|k_{pp}/k_0 - 1|$ between the pole at k_{pp} and the branch point at $\lambda = k_0$ as a function of dielectric thickness (h/λ_0) . It can be seen that in the case of electrically thin substrates, the pole due to the surface wave is very close to the branch point. In such cases, radius r must be chosen carefully to avoid the inclusion of the branch point into the borders of the circle inclusion thereof violating the analyticity of $F(k_p)$. With the use of (16) and careful selection of r , it is

now possible to numerically determine a value for Res. For instance, at 1.206 GHz ($k_0 = 25.2753$) for $h/\lambda_0 = 0.07$, $R/\lambda_0 = 0.5$, $\epsilon_r = 4.34 - j0.0868$ and $r = 1.0153 \text{ m}^{-1}$ we have $\text{Res} = 0.47323 - j0.01815$ where $k_{pp} = 27.3059 - j0.052039$. Once k_{pp} and the residue are known, the pole in the G_V integrand may be extracted according to the technique described above; that is

$$\begin{aligned} & \int_{k_0}^{k_0\sqrt{\epsilon_r}} F(\lambda) d\lambda - \int_{k_0}^{k_0\sqrt{\epsilon_r}} [F(\lambda) - F_{sing}(\lambda)] d\lambda \\ & + \int_{k_0}^{k_0\sqrt{\epsilon_r}} F_{sing}(\lambda) d\lambda \end{aligned} \quad (17)$$

F_{sing} is analytically integrable [4] while the difference term, which is a well-behaved function, may be integrated numerically. In the lossless case (i.e. for $\tan\delta = 0$) we have $k_{pp} = \lambda_p$, in other words, the pole due to D_{TM} lies on the λ -axis which is the path of integration. Therefore, at λ_p both terms constituting the difference term in (17), become singular. However, by evaluating $F(\lambda + \delta) - F_{sing}(\lambda + \delta)$ where $\delta \rightarrow 0$ it is possible to obtain an accurate estimate of the well-behaved difference term at λ_p . In the case of lossy dielectrics, the pole at k_{pp} does not lie on the path of integration (Figure 11), nevertheless, strong variations in the integrand due to the pole still require application of this pole extraction technique. An infinite derivative in the difference term integrand at $\lambda = k_0$ may then be eliminated by the substitution $\lambda = k_0 \cosh t$. The real and imaginary parts of the G_V difference term integrand, after substitution, are shown in Figure 15; the singularity which has been extracted is visible in Figure 11. If the integrand does not contain D_{TM} in the denominator, the substitution may nevertheless be performed to obtain a smooth integrand at $\lambda = k_0$. This is the case for the Green function $G_A^{xx}(r|r')$, for which Figure 16 gives an illustration of the integrand shown in Figure 10, after substitution. At this point, we are able to accurately determine the integrals in (9) and (10) for $0 \leq \lambda \leq k_0(\epsilon_r')^{1/2}$. This leaves the interval $\lambda > k_0(\epsilon_r')^{1/2}$ which is the subject of the following section.

4.3 The method of averages in the interval $\lambda \in [k_0(\epsilon_r')^{1/2}, \infty]$

As seen from Figures 10 and 11 the Green function integrands show oscillatory behaviour in this interval. Furthermore, these integrands have envelopes which converge very slowly and therefore standard integration routines (such as the trapezium rule and Gauss quadrature) prove to be very inefficient since a large number of integration points is required to achieve reasonable accuracy. Mosig and Gardiol [9] have found a technique known as the *method of averages*, introduced by Hurwitz and Zweifel [13], to be suitable for application to Sommerfeld integrals appearing in microstrip problems. This method is based on the decomposition

$$\int_a^\infty g(\xi R) f(\xi) d\xi = \sum_{n=0}^{\infty} \int_{a+np/2}^{a+(n+1)p/2} g(\xi R) f(\xi) d\xi \quad (18)$$

where $g(\xi R)$ is an oscillating function with period p and $f(\xi)$ a smooth, non-oscillating function which behaves asymptotically as $O(\xi^\alpha)$; the integrand therefore diverges for $\alpha > 0$. Although Bessel functions of the first kind - appearing in the Green function expressions - are not strictly periodic, the method of averages may still be applied. However, since the zero's of Bessel functions are not known off-hand the large-argument approximation $J_n(\lambda R) \approx [2/(\pi \lambda R)]^{1/2} \cos(\lambda R - \pi/4 - n\pi/2)$ is used to estimate their zero's. Then we have

$$\xi_m = \left[(m-1) + 0.75 + \frac{n}{2} \right] \frac{\pi}{R} \quad (19)$$

where ξ_m approximates the m 'th zero of $J_n(\lambda R)$. Table 3.1 gives an indication of the accuracy of this approximation in comparing ξ_m ($m=1,2,3,4$) with the actual zero's of $J_0(\lambda)$ determined numerically with the IMSL routine ZREAL [11]. A question about the validity of this approximation for small R values (source and observation points close to each other) might well arise at this point. In order to answer this question, definite integrals for which the answers are known, were evaluated by the authors using (19) in the method of averages. We know from [14] that

$$\int_0^\infty J_n(\lambda R) d\lambda = \frac{1}{R} \quad (20)$$

for $n > -1$. This identity was confirmed for R values ranging from 2.0×10^{-6} to 2.0 and for both $n=0$ and $n=1$. Further tests performed by the authors on similar identities lead to the conclusion that (19) will not introduce a significant error, even for small values of R , when used in the method of averages.

m	m'th zero of $J_0(\lambda)$	ξ_m	error (%)
1	2.404825	2.356194	2.02
2	5.520078	5.497787	0.40
3	8.653727	8.639379	0.16
4	11.79153	11.78097	0.08

Table 3.1 Zero's of $J_0(\lambda)$ determined with ZREAL [11] and (19) respectively.

Figure 17 gives the method of averages in the form of a flowchart. The first step is to perform an integration over a half cycle to determine I_m^1 .

$$I_m^1 = \begin{cases} \xi_m \\ \int_a^{\xi_m} g(\xi R) f(\xi) d\xi \quad (m=1) \\ I_{m-1}^1 + \int_{\xi_{m-1}}^{\xi_m} g(\xi R) f(\xi) d\xi \quad (m>1) \end{cases} \quad (21)$$

where ξ_m is the m 'th successive zero of the oscillating function g , with $\xi_m > a$. I_{m-1}^2 is then determined through the use of a *weighted mean*

$$I_{m-1}^2 = \frac{w_{m-1}^1 I_{m-1}^1 + w_m^1 I_m^1}{w_{m-1}^1 + w_m^1} \quad (22)$$

with both I_m^1 and I_{m-1}^1 having been determined previously through integration and with the weights given by $w_m^k = (\xi_1/\xi_m)^{(\alpha+1+k)}$. In general, (22) is given by

$$I_m^k = \frac{w_m^{k-1} I_m^{k-1} + w_{m+1}^{k-1} I_{m+1}^{k-1}}{w_m^{k-1} + w_{m+1}^{k-1}} \quad (23)$$

If $m-1 \neq 1$ then I_{m-2}^3 is calculated through the use of (23) and the process is repeated until we have I_1^k (where $k=m$) which will give an approximation of the actual value, $I(R)$, despite the fact that no additional integrations were performed. If the error criterion is not met, I_m^1 (where $m = k+1$) may be determined through integration, (21), and I_1^{k+1} through repeated application of (23). In this way, an estimate for $I(R)$ may be obtained.

In the determination of the discrete Green function self terms, the situation arises where the distance between source and observer (R) tends to zero. The effect of this, as discussed earlier and illustrated by (19), is that the zero's of the oscillating Green function integrand move further out from the origin along the λ -axis. In the method of averages, weights are determined according to the zero's of the oscillating function, i.e. $w_m^k = (\xi_1/\xi_m)^{(\alpha+1+k)}$. Now it is apparent that, for $\xi_m > > \xi_1$ and k a positive integer which may be large, the weight w_m^k could become a very large real number, creating possible numerical difficulties (numeric overflow or round-off errors, for instance). The present authors have addressed this problem through mathematical manipulation of (23) after which

$$I_m^k = \frac{I_m^{k-1}}{1+\beta} \left[1 + \beta \left(\frac{I_{m+1}^{k-1}}{I_m^{k-1}} \right) \right] \quad (24)$$

where $\beta = 10 \exp\{(\alpha+2-k)[\log_{10}(\xi_1/\xi_{m+1}) - \log_{10}(\xi_1/\xi_m)]\}$ is now a manageable real number even though w_m^{k-1} and w_{m+1}^{k-1} are very large. Consider for example a situation where $\xi_1=200$, $\xi_{50}=8 \times 10^3$, $\xi_{51}=8.1 \times 10^3$, $k=50$ and $\alpha=0$; then we have $w_{50}^{49}=7.923 \times 10^{76}$ and $w_{51}^{49}=1.438 \times 10^{77}$ whilst $\beta = 1.815$!. Therefore, to avoid numerical difficulties which may be encountered in a straightforward application of (23), we propose (24) as a means to determine I_m^k .

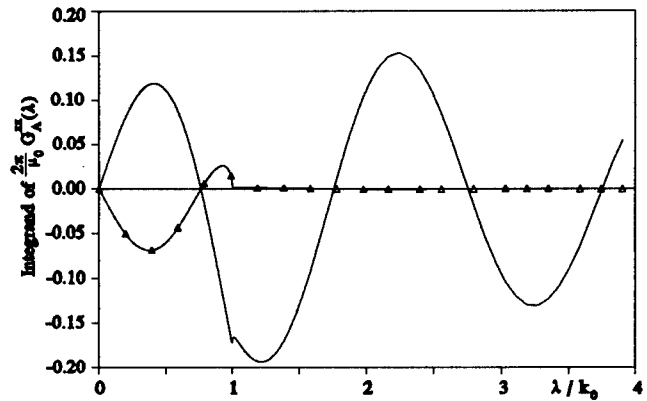


Figure 10 Real (—) and imaginary (—△—△—) integrands of $(2\pi/\mu_0)G_A^{xx}$ for $\epsilon_r=4.34-j0.0868$, $h/\lambda_0=0.07$ and $R/\lambda_0=0.5$.

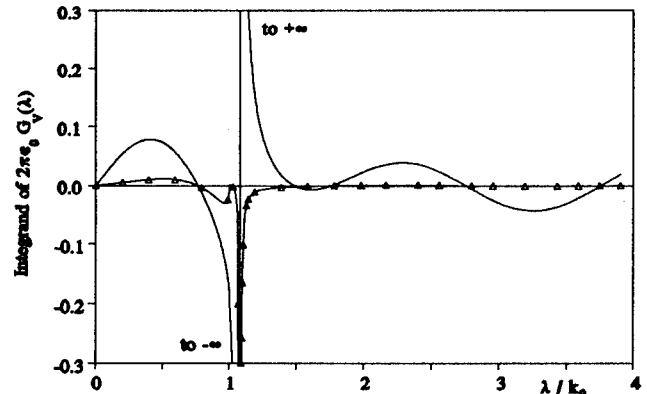


Figure 11 Real (—) and imaginary (—△—△—) integrands of $2\pi\epsilon_0 G_V$ for $\epsilon_r=4.34-j0.0868$, $h/\lambda_0=0.07$ and $R/\lambda_0=0.5$ at 1.206 GHz.

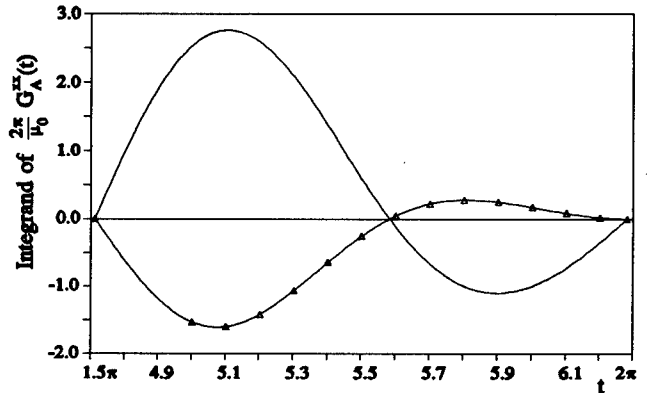


Figure 12 Real (—) and imaginary (—△—△—) integrands of $(2\pi/\mu_0)G_A^{xx}$ for $\lambda \in [0, k_0]$ after substitution $\lambda=k_0 \cos t$.

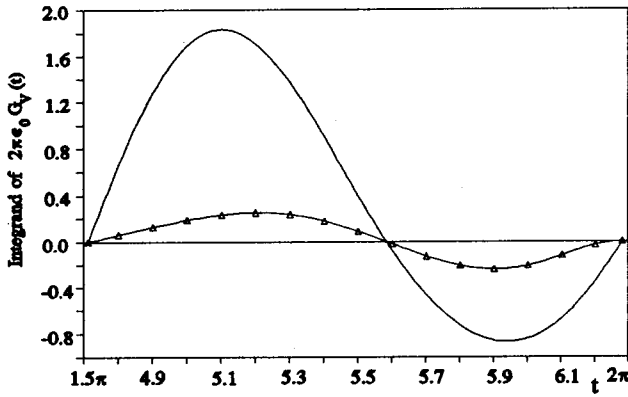


Figure 13 Real (—) and imaginary (—△—△—) integrands of $2\pi\epsilon_0 G_V$ in the interval $\lambda \in [0, k_0]$ after substitution $\lambda = k_0 \cos t$.

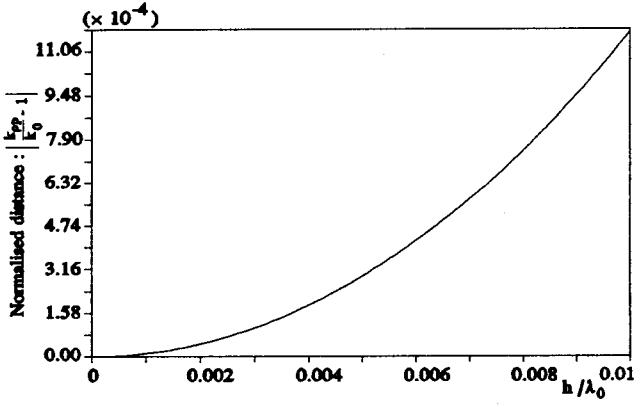


Figure 14 Normalised distance between the pole due to D_{TM} and the branch point due to u_0 as a function of dielectric thickness, i.e. $|k_p/k_0 - 1| (h/\lambda_0)$.

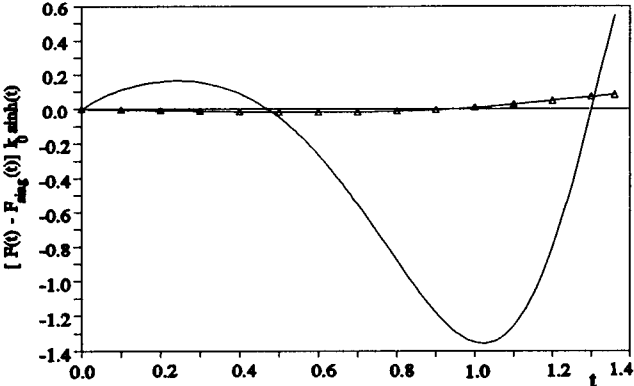


Figure 15 $2\pi\epsilon_0 G_V$ difference term integrand (real (—) and imaginary (—△—△—△—)) after substitution $\lambda = k_0 \cosh t$.

5. INTERPOLATION

As discussed in the previous section, the evaluation of the Green functions require implementation of numerical integration routines. This is in addition to

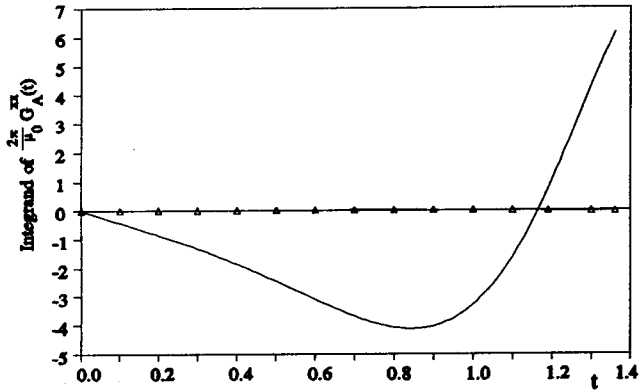


Figure 16 Integrand of $(2\pi/\mu_0)G_A^{xx}$ (real (—) and imaginary (—△—△—△—)) after substitution.

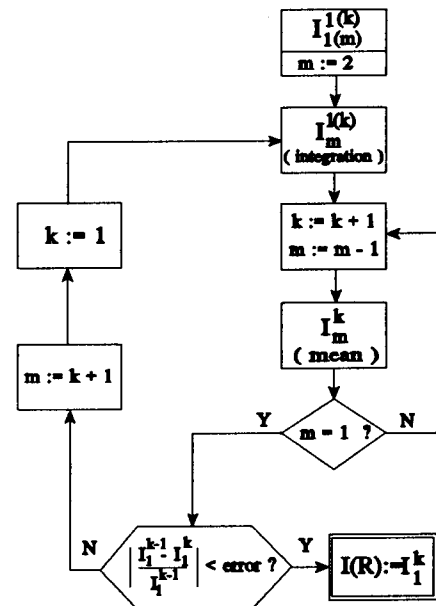


Figure 17 Flowchart for the method of averages

the numerical integration which has to be performed in the evaluation of the discrete Green functions (which contain the Green functions). With these discrete Green functions it is now possible to compute the moment method matrix elements whose solution yields the unknown coefficients I_x and I_y . However, in order to reduce the computation time, Mosig and Gardiol, noting the fact that the relevant Green functions are only dependent on the distance between source and observer (and not the relative orientation), consequently suggest the use of an interpolation table to evaluate the Green functions. This interpolation table consists of a discrete set of Green function

values tabulated against a set of distances R_i where $i=1..P$ and $R_{\min} < R_i < R_{\max}$. Interpolation is then used to evaluate these functions at any distance ranging from R_{\min} to R_{\max} (the maximum linear dimension of the structure). It is suggested that convergence tests be performed to determine optimum values for P (typically from 50 to 250) related to specific problems. Since the value of R_{\min} has an effect on the self term evaluation of the discrete Green functions, care should be taken when choosing values for R_{\min} . However, numerical experiments performed by the present authors, showed differences on the order of 0.1% in the self term values computed for $R_{\min}=10^{-4}$ and for $R_{\min}=10^{-11}$. Furthermore, careful consideration should be given to the computation of R_i . In this regard, the following expressions have been used to good effect:

$$R_i = R_{\min} \left(\frac{R_{\text{inter}}}{R_{\min}} \right)^{\left(\frac{i-1}{N-1} \right)} \quad (25a)$$

for $R_{\min} < R < R_{\text{inter}}$ and

$$R_i = R_{\text{inter}} + (R_{\max} - R_{\text{inter}}) \left(\frac{i-1}{N-1} \right) \quad (25b)$$

for $R_{\text{inter}} < R < R_{\max}$ where $R_{\text{inter}} = (a^2 + b^2)^{1/2}$. With interpolation it is possible to reduce the computation time without sacrificing significant accuracy.

6. COMPUTATION OF FAR-ZONE RADIATION

In solving for the surface current distribution, we are interested in the case where both source and observer are located on the air-dielectric interface i.e. where $z=0$. For far-field radiation computation, on the other hand, this will not be the case. If the radiator is placed in the xy -plane, far-field radiation on broadside now implies that z becomes large and then the following situation arises: since u_0 is purely imaginary in the interval $0 \leq \lambda < k_0$, and z a very large real number, $\exp(-j(k_0^2 - \lambda^2)^{1/2}z)$ causes rapid sign changes in this interval. Furthermore, since u_0 is real for $\lambda \geq k_0$ we have $\exp(-u_0 z) \rightarrow 0$ and thus the integration interval in effect reduces to $0 \leq \lambda < k_0$. An example of a Green function integrand for $z=5.0$ m

is shown in Figure 18 which illustrates the rapid sign changes and reduced integration interval just spoken of. From this figure it is clear that standard numerical integration routines would not be capable of yielding accurate estimates of the Green function integrals with large z values. We therefore resort to *asymptotic techniques* to obtain approximate analytic solutions. Application of the *method of steepest descent* [15] to these integrals yields the following far-field radiation expressions for arbitrarily shaped etched antennas in terms of the coefficients I_x and I_y [3]:

$$E_{\theta} = G_E^{\theta x}(r|0) \sum_{i=1}^M a I_{xi} e^{j k_0 g_i} + G_E^{\theta y}(r|0) \sum_{j=1}^N b I_{yj} e^{j k_0 g_j} \quad (26)$$

$$E_{\phi} = G_E^{\phi x}(r|0) \sum_{i=1}^M a I_{xi} e^{j k_0 g_i} + G_E^{\phi y}(r|0) \sum_{j=1}^N b I_{yj} e^{j k_0 g_j} \quad (27)$$

where $g_k = x_k \sin \theta \cos \phi + y_k \sin \theta \sin \phi$ ($k=i,j$); x_k and y_k are the centre coordinates of the k 'th current cell. We also have

$$G_E^{\theta x}(r|0) = \frac{-j Z_0 \cos \phi f_{\theta}(\theta)}{\lambda_0} \frac{e^{-j k_0 r}}{r} \quad (28)$$

$$G_E^{\phi x}(r|0) = \frac{j Z_0 \sin \phi f_{\phi}(\theta)}{\lambda_0} \frac{e^{-j k_0 r}}{r} \quad (29)$$

$$G_E^{\theta y}(r|0) = \frac{-j Z_0 \sin \phi f_{\theta}(\theta)}{\lambda_0} \frac{e^{-j k_0 r}}{r} \quad (30)$$

$$G_E^{\phi y}(r|0) = \frac{-j Z_0 \cos \phi f_{\phi}(\theta)}{\lambda_0} \frac{e^{-j k_0 r}}{r} \quad (31)$$

$$f_{\theta}(\theta) = \frac{T \cos \theta}{[T - j \epsilon, \cos \theta \cotan(k_0 h T)]} \quad (32)$$

$$f_{\phi}(\theta) = \frac{\cos \theta}{[\cos \theta - j T \cotan(k_0 h T)]} \quad (33)$$

$$T = \sqrt{(\epsilon_r - \sin^2 \theta)} \quad (34)$$

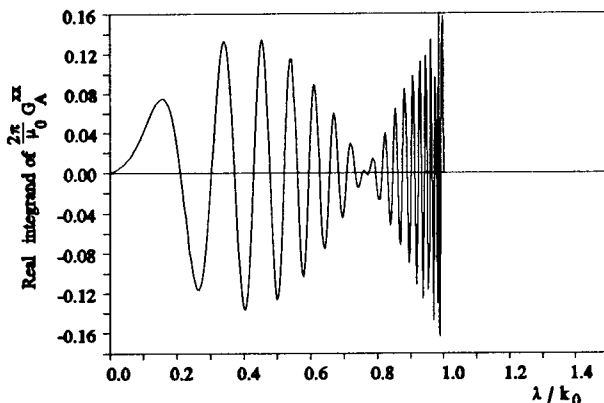


Figure 18

Figure 18 Normalised real integrands of G_A^{xx} (i.e. $J_0(\lambda R)\lambda \exp(-u_0 z)/D_{TE}$ for $R/\lambda_0=0.5$ and $h/\lambda_0=0.07$ at $f=1.206$ GHz and $\epsilon_r=4.34-j0.0868$) for $z = 0.0$ and 5.0 m.

7. SUMMARY

The MPIE formulation rates among the accurate integral equation analysis techniques for microstrip radiating structures. After a brief overview of the modelling scheme, numerical techniques used by the authors in the implementation of the formulation were discussed: a detailed and illustrated discussion of the numerical evaluation of the required Green functions was given, an interpolation method used to improve the computational efficiency was discussed and finally the computation of far-field radiation patterns was considered. A FORTRAN computer code implementation of the MPIE formulation is available on request from the second author.

Acknowledgements :The authors would like to thank Dr.J.R.Mosig of the *Laboratoire d'Electromagnetisme et d'Acoustique (LEMA)*, *Ecole Polytechnique Federale de Lausanne (EPFL)*, Lausanne, Switzerland, who gave generously of his time and advice during the present work.

References

- [1] D.M.Pozar, "Microstrip antennas", *Proc.IEEE*, Vol.80, No.1, pp.79-91, Jan.1992.
- [2] J.R.Mosig & F.E.Gardioli, "A dynamical radiation model for microstrip structures" in P.Hawkes (Edit.) : *Advances in Electronics and Electron Physics* (Academic Press,1982) pp.139-327.
- [3] J.R. Mosig and F.E. Gardiol, "General integral equation formulation for microstrip antennas and scatterers," *IEE Proc.*, vol. 132, Pt.H, no. 7, Dec. 1985.
- [4] J.R. Mosig and F.E. Gardiol, "Numerical analysis of microstrip patch antennas" in J.R.James & P.S.Hall (Edits.) : *Handbook of Microstrip Antennas* (Peter Peregrinus Ltd.,1989).
- [5] I.P. Theron & J.H. Cloete, "On the use of the Leontovich boundary conditions in the analysis of microstrip antennas", *1992 IEEE AP-S Symposium*, pp. 620-623.
- [6] R.C. Hall, J.R. Mosig and F.E. Gardiol, "Analysis of microstrip antenna arrays with thick substrates", *Proc. 17 th European Microwave Conf.*, Rome, 1987.
- [7] J.R. Mosig, Laboratoire d'Electromagnetisme et d'Acoustique, Ecole Polytechnique Federale de Lausanne, Lausanne, Switzerland. Private communication.
- [8] M. Hestenes and E. Stiefel, "Method of conjugate gradients for solving linear systems," *J. Res. Natl. Bur. Stand.*, vol. 49, pp. 409-436, 1952.
- [9] J.R. Mosig and F.E. Gardiol, "Analytic and numerical techniques in the Green's function treatment of microstrip antennas and scatterers," *IEE Proc.*, vol. 130, Pt.H, no. 2, pp. 175-182, March 1983.
- [10] D.E. Müller, "A method for solving algebraic equations using an automatic computer", *Math. Tables Aids Comput.*, vol. 10, pp. 208-215, 1956.
- [11] IMSL Inc., Houston, Texas, USA. Library of Fortran Routines for Mathematical Application, Version 1.0, April 1989.
- [12] E. Kreyszig, *Advanced Engineering Mathematics* (John Wiley & Sons, 1988).
- [13] H. Hurwitz and P.F. Zweifel, "Numerical quadrature of Fourier transform integrals," *Math. Tables Aids Comput.*, vol. 10, pp. 140-149, 1956.
- [14] M.R. Spiegel, *Mathematical handbook* (McGraw-Hill, 1968).
- [15] L.B. Felsen and N. Marcuvitz, *Radiation Scattering of Waves* (Prentice_Hall, 1973).

Performance of a Characteristic-Based, 3-D, Time-Domain Maxwell Equations Solver on the Intel Touchstone Delta

J. S. Shang¹ & Kueichien C. Hill²

Wright Laboratory, Wright-Patterson Air Force Base, Ohio 45433-7913

and

Donald A. Calahan³

University of Michigan, Ann Arbor, Michigan

Abstract⁴

A characteristic-based, windward⁵ numerical procedure for solving three-dimensional Maxwell equations in the time domain has been successfully ported to the Intel Touchstone Delta multicomputer. The numerical results by concurrent computation duplicated the earlier simulations of an oscillating electric dipole on a vector processor and compared well with the exact solutions. The parallelized code is scalable up to 512 nodes and incurs only up to 7.6% performance degradation. The sustained data processing rate is clocked at 6.551 Gi-gaops. However, the data I/O process is unscalable on the shared memory system.

Nomenclature

E	Electric field intensity
H	Magnetic field intensity
i, j, k	Indices of discretized grids
J	Electric current vector
L	One-dimensional difference operator
n	Index of time level
t	Time
W	One-dimensional characteristic
x, y, z	Cartesian coordinates
r, θ, ϕ	Spherical coordinates
ϵ	Electric permittivity
μ	Magnetic permeability
λ	Eigenvalue

1 Introduction

The improvement of numerical efficiency is one of the urgent needs of computational electromagnetics (CEM) in aircraft signature technology. In this area of

applications, the CEM simulations are generally more computationally intensive than computational fluid dynamics (CFD) problems. A part of the reason is that the numerical accuracy requirement for CEM tends to be more stringent than for CFD. For instance, a desirable predictive dynamic range can be as high as 60 dB over broad viewing ranges [1]. Typically for wave propagation, a suitable numerical resolution requires each wavelength to be supported by at least an order of ten grid points or more. Thus, for a scatterer with high refraction indices and material complexities, this more than ten grid points per wavelength requirement translates into the need of a computing system with astronomical computing speed and memory size.

The heavy demand on computer speed and memory for CEM simulations can be illustrated by the following example. For a fixed incident angle, the numerically generated signature of a modern fighter configuration at 1 GHz requires approximately fifty million grid points⁶ to produce a ten grid points per wavelength resolution. For each grid point, the values of at least three coordinates, six field components, and nine direction cosines of a general curvilinear coordinate system need to be stored [2,3,4,5]. This results in a total of nearly one billion memory allocations. A typical CEM code operating on a 100 Megaops (10^6 floating point and integer operations) single vector processor can process data at approximately a rate of three-tenths of a microsecond per grid point per time step. At this rate, a fighter configuration will require almost five hours of computing just to advance the solution to a new time level. In order to complete a signature simulation, usually multiple look angles and hundreds of time steps are required. As a result, the large computer memory requirement and solution time has rendered the use of conventional data processors for solving CEM problems impractical.

The goal of this paper is to provide an efficient way of solving the 3D time domain Maxwell's equations in differential form by combining novel numerical algo-

¹Senior Scientist, Fellow AIAA

²Electronics Engineer, Signature Technology Office

³Professor, Electrical Engineering & Computer Science Department

⁴This paper is declared a work of the U.S. Government and is not subject to copyright protection in the United States.

⁵The windward difference approximation is achieved by using the one-sided stencil for computing the difference quotient according to the sign of the coefficient.

⁶Based on 15mx10mx8m size

rithms and concurrent computing technology. In the recent years, the CFD community has made significant progress in the area of algorithm development [6,7,8]. Numerical algorithms for solving hyperbolic equations⁷ from the CFD discipline have been adopted for solving three-dimensional Maxwell equations in the time domain [2,3,4,5]. Among these, the characteristic-based algorithm is found to be most efficient and appropriate to duplicate the wave motions that are governed by the time-dependent Maxwell equations [1,2,3]. This numerical scheme is derived from the eigenvalue and the eigenvector structure of the hyperbolic equations system. The procedure is to diagonalize the three-dimensional governing equations into three one-dimensional Riemann problems [3,4,5,6]. Although this new numerical procedure has potential to reduce the required computing resources by allowing larger time steps and fewer discretized mesh points in CEM simulations, substantial progress in CEM for practical applications can finally be achieved by incorporating the massively parallel computing technique to deliver the needed computing resources.

Recently, through remarkable progress in microchip and interconnect data link technology, a host of single address, shared memory, and multiple address message-passing parallel computers becomes available for data processing. These scalable multi-processors or multi-computers, in theory, are capable of providing essentially unlimited computing resources for scientific simulations. However, the effective use of these massively parallel computers still rests squarely on balancing the work load and keeping the communication between computing nodes to an absolute minimum [9,10]. These requirements are intrinsically related to the numerical algorithms and hardware architectures. In the present research effort, attempts were made to map a characteristic-based algorithm onto a message-passing parallel computer for computational electromagnetics.

2 Analysis

The characteristic-based fractional-step algorithms have been demonstrated to be very efficient in solving three-dimensional Maxwell equations in the time domain [3,4,5]. In this method, the time-dependent Maxwell equations can be written in the flux vector form [11,12] given by

$$\frac{\partial U}{\partial t} + \frac{\partial F}{\partial x} + \frac{\partial G}{\partial y} + \frac{\partial H}{\partial z} = -J \quad (1)$$

⁷A partial differential equations $AU_{xx} + BU_{xy} + CU_{yy} + DU_{x} + EU_{y} = F$ with $B^2 - 4AC > 0$, or all eigenvalue of these coefficient matrices are real.

where

$$U = \begin{Bmatrix} B_x \\ B_y \\ B_z \\ D_x \\ D_y \\ D_z \end{Bmatrix} \quad F = \begin{Bmatrix} 0 \\ -D_z/\epsilon \\ D_y/\epsilon \\ 0 \\ B_z/\mu \\ -B_y/\mu \end{Bmatrix}$$

$$G = \begin{Bmatrix} D_z/\epsilon \\ 0 \\ -D_x/\epsilon \\ -B_z/\mu \\ 0 \\ B_x/\mu \end{Bmatrix} \quad H = \begin{Bmatrix} -D_y/\epsilon \\ D_x/\epsilon \\ 0 \\ +B_y/\mu \\ -B_x/\mu \\ 0 \end{Bmatrix} \quad J = \begin{Bmatrix} 0 \\ 0 \\ 0 \\ J_x \\ J_y \\ J_z \end{Bmatrix}$$

The above partial differential equation system is hyperbolic, and constitutes an initial value problem. Since the three coefficient matrices can only be diagonalized one at a time [6,7], the three-dimensional equation is split into three one-dimensional formulations. For each one-dimensional formulation, the solving procedure starts with solving the eigenvalues and eigenfunctions of that particular spatial direction. The eigenvalues for all three coefficient matrices turn out to be $\{-c, -c, 0, 0, c, c\}$, where c is the wave propagating speed. The signs of these eigenvalues actually control the direction of the information flow as the wave propagates through the computational domain [3,4,5,6]. Based on the eigenvectors, the field components are then expressed in terms of characteristic variables for that spatial direction. Once expressed in the characteristic form, the one-dimensional formulation becomes that of the Riemann problem [5,6]. After applying the same procedure to the other two dimensions, the characteristic-based fractional-step or time-splitting method can now be summarized in the following formulas:

$$w^{n+2} = L_x L_y L_z L_z L_y L_x w^n \quad (2)$$

$$L_x : \frac{\partial w_{x,i}}{\partial t} + \lambda_i \frac{\partial w_{x,i}}{\partial x} = 0 \quad i = 1, 2, \dots, 6 \quad (3)$$

$$L_y : \frac{\partial w_{y,i}}{\partial t} + \lambda_i \frac{\partial w_{y,i}}{\partial y} = 0 \quad i = 1, 2, \dots, 6 \quad (4)$$

$$L_z : \frac{\partial w_{z,i}}{\partial t} + \lambda_i \frac{\partial w_{z,i}}{\partial z} = 0 \quad i = 1, 2, \dots, 6 \quad (5)$$

where w_x , w_y , and w_z are the one-dimensional characteristic variables associated with the x , y , and z directions; L is the one-dimensional difference operator; λ_i are the eigenvalues of the partial differential equation system; and n is the index of time level⁸.

⁸The fractional Step method sweeps all spatial derivatives twice in a symmetric sequence, thus advances the time step accordingly

The second-order accurate windward difference approximation can be easily constructed by using a single forward or backward difference approximation according to the signs of the eigenvalues. The ability to associate the sign of the eigenvalue with the direction of wave propagation is a very important feature of the present numerical procedure. The windward difference approximation for L_x is given by

$$\frac{\partial w}{\partial t} = \frac{w_{i,j,k}^{n+1} - w_{i,j,k}^n}{\Delta t} \quad (6)$$

$$\frac{\partial w}{\partial x} = \frac{-3w_{i,j,k}^* + 4w_{i+1,j,k}^* - w_{i+2,j,k}^*}{2\Delta x} \quad \lambda < 0 \quad (7)$$

$$\frac{\partial w}{\partial x} = \frac{3w_{i,j,k}^* - 4w_{i-1,j,k}^* + w_{i-2,j,k}^*}{2\Delta x} \quad \lambda > 0 \quad (8)$$

where $*$ takes the values $n + 1$ and n respectively for implicit and explicit procedures; i, j, k are the indices of discretized grids. The windward difference approximations for L_y and L_z are similar to that for L_x . They can be obtained by replacing x in Equations (10) and (11) with y and z , and applying the windward difference to the j and k indices, respectively.

From Equation (5), the time-splitting solving procedure requires six one directional numerical sweeps to update the solution to the next time level. Since the formulation for each numerical sweep is identical, the strategy to map each one directional sweep to a massively parallel computer is identical. Thus, a code based on the time-splitting algorithm can be easily tuned for maximum performance by counting and adjusting arithmetic operations for each numerical sweep.

3 Data Partition Schemes and Fine Tuning for Maximum Parallel Performance

The partition of data structure plays a key role in achieving high parallel efficiency. On a message passing or distributed memory multicomputer system, the performance of concurrent computing is closely tied to memory bandwidth and memory latency. Thus, the basic strategy in achieving high parallel efficiency of any numerical procedure is to minimize data movements between nodes. In this effort, a computer code based on the characteristic-based fractional-step algorithm was mapped onto the Intel Touchstone Delta at Caltech using different data partition schemes to explore the parallel performance of the code.

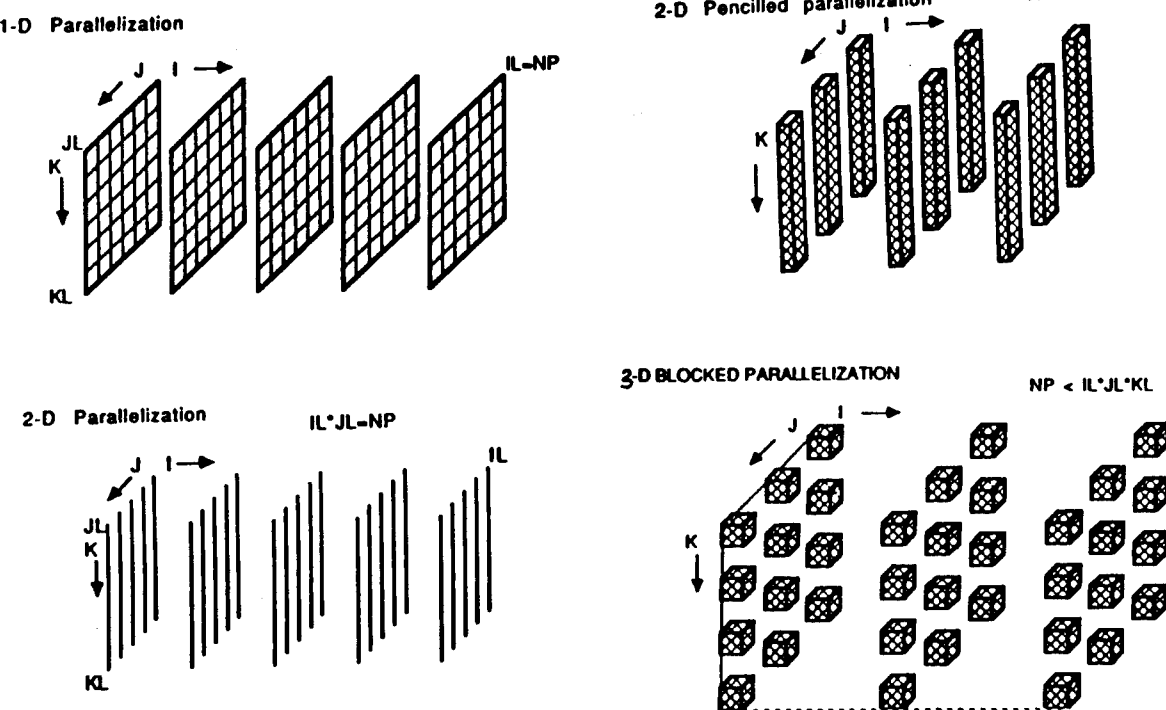


Figure 1: Hierarchy of data partition

The Delta multicomputer consists of a total of 576 heterogeneous nodes [13]. They are designated as numeric, service, gateway, and disk nodes to perform the computation, frame buffer, network link, and disk string functions respectively. A total of 512 numeric nodes are available for parallel computing. Each of the numeric nodes has a peak rate of 80 MFlops for single-precision and 60 MFlops for double-precision, and is interconnected by a two-dimensional mesh network. On this ensemble nodal architecture, the data flow and data management lead to four different approaches for the controlling of data movements between nodes. The most elementary approach to data partition is the one-dimensional parallelization in which the outermost do loop of the numerical sweeps is assigned to a number of numeric nodes. The other data partition schemes include the two-dimensional page structure by partitioning three dimensional space into cross-sectional planes, the pencil grouping, and finally, the three-dimensional block parallelization. A graphic depiction of these data partition schemes is given in Figure 1. The computational domain is assumed to consist of IL , JL , and KL discretized mesh points in each direction of the three dimensional space; the computation is assigned to NP numeric nodes.

As mentioned in the beginning of this section, minimizing the number of message passings is by far most important in achieving high parallel efficiency. In addition, load balancing is also very important in reducing the performance disparity among nodes since the performance of the slowest node actually determines the completion of a numerical simulation. Last, but not least, an ultimate data assigning sequence which takes advantage of the nearest neighbor message-passing priority is essential in reducing the unnecessary message routing length and, therefore, improve the over all parallel performance. In the following discussion, the number of message passings, load balancing, and sequence assigning issues will be addressed.

Although four data partition schemes are identified in mapping the characteristic-based code onto the Delta, only the one-dimensional parallelization and the pencil grouping scheme were investigated in this effort. The one-dimensional scheme is the most straightforward data partition for the time-splitting, windward procedure [5]. In this scheme, the computational domain of $IL \times JL \times KL$ mesh points is divided into either IL , JL , or KL grid planes. Without loss of generality, the computational domain is assumed to be divided into IL grid planes. Thus, each grid plane contains $JL \times KL$ mesh points. The computation associated with the $JL \times KL$ mesh points of each grid plane is assigned to a numeric node. At each time level, each node performs eight mes-

sage passings, which include messages sent to and received from its nearest four neighboring nodes. In all, the total number of message passings is given by the value of $2 \times (4 \times IL - 6)$. With four bytes per message, the message length associated with each message passing is determined by $JL \times KL \times 4$. For example, a $(node \times 48 \times 48)$ mesh system will have a message length of 9,216 bytes.

Since each node performs the same amount of arithmetic operations in the one-dimensional partition, load balance is automatically achieved. This type of data partition can be viewed as a form of task partitioning.

In one-dimensional parallelization scheme, the number of numeric nodes required is equal to the number of grid planes, 'IL'. To locate the desired number of numeric nodes, a Delta partition (m, n) with m rows and n columns should contain 'IL' nodes. Every node in this partition has a logic number assigned to it which a programmer can access through the function call "mynode()". The returned value of "mynode()" ranges from 0 to $nm - 1$ for the (m, n) partition. Since IL equals $nm - 1$, an easy way of mapping the grid planes to the nodes is to assign grid plane number one to node 0, grid plane number two to node 1, and etc. In other word, for the i th grid plane, the computation associated with that grid plane is performed by numeric node $i - 1$. Unfortunately, this logical sequence assignment does not take advantage of the nearest neighbor message-passing priority and incurs unnecessary delay in data movement. Particularly, the message passing in Delta is row biased. If a grid plane is located at or next to a boundary of the Delta partition, the messages of this grid plane will have to be routed through ' n ' or ' $n - 1$ ' nodes before reaching its destination grid plane located in a different row of the Delta partition.

One way to avoid this delay is to use the serpentine sequence in assigning the grid planes to the numeric nodes, such that any message need not travel more than two nodes to reach its destination grid plane [11]. The serpentine arrangement can be easily achieved by the following program instruction:

$$i = \begin{cases} \text{mynode}() + 1 & x = \text{even number} \\ (2 * x + 1) * n - \text{mynode}() & x = \text{odd number} \end{cases}$$

where the row number $x = 0, 1, 2, \dots, m - 1$. The example of a $(4, 5)$ Delta partition with its physical layout and logical node numbers given by mynode() is shown in Table 1 (a). The indices of the grid planes mapped to the $(4, 5)$ partition using logical sequence and serpentine sequence are shown in table 1 (b) and (c), respectively.

In the pencil grouping scheme employed here, the calculations associated with two dimensions of the com-

0	1	2	3	4
5	6	7	8	9
10	11	12	13	14
15	16	17	18	19

1	2	3	4	5
6	7	8	9	10
11	12	13	14	15
16	17	18	19	20

1	2	3	4	5
10	9	8	7	6
11	12	13	14	15
20	19	18	17	16

(a)

(b)

(c)

Table 1: (a) Logical node numbers of a (4, 5) Delta partition given by mynode(). (b) The grid planes mapped to the (4, 5) partition using Logical sequence. (c) The grid planes mapped to the (4, 5) partition using Serpentine sequence.

putational domain, for instance $IL \times JL$, is assigned to an (m, n) partition on the Delta. In other words, each numeric node performs the calculations associated with $(IL \times JL \times KL)/mn$ grid points. If the value of $(IL \times JL \times KL)/mn$ turns out to be an integer, each node will perform the same amount of arithmetical operations and load balance is automatically achieved. If the value is non-integer, some nodes will have more grid points to calculate than some others. In this case, an optimum assignment must be sought to balance the load. Although in some cases load balance is not automatically achieved, a pencil grouping scheme provides greater flexibility than the one-dimensional scheme in assigning grid points to the numeric nodes.

Since in the pencil grouping scheme, only the data near the surface of the pencil must be transferred to the adjacent pencils, the data flow is reduced compared with the one-dimensional partition scheme. Thus, a larger pencil size will reduce the overall data flow and enhance the concurrent performance. The number of message passings depends on the size of each pencil partition.

4 Scope of Numerical Experiments

All numerical solutions reported in this paper were processed on the Delta system. The numerical simulations were focused on a three-dimensional oscillating electric dipole. Although the physics of the oscillating dipole is well known, it is chosen because its theoretical solution [11,12] can be used for validation. Besides, the exact solution contains a singular behavior at the center of the dipole. The leading term of this singularity appears as the inverse cubic power of the radial distance from the dipole [12]. Therefore, it offers a serious challenge to the accuracy of the numerical simulation and the robustness of the solving procedure. To determine the suitable mesh spacing to capture the singular behavior of the dipole, a three-level mesh spacing refinement study was conducted. The numerical results were compared with the theoretical solutions to assess the accuracy of the simulations. Details comparisons will be reported in the next section.

In addition to the validation with the exact solu-

tions, the results generated by the parallel codes for the one-dimensional parallelization and the pencil grouping schemes on a $(48 \times 48 \times 48)$ mesh system were compared with the previous numerical results generated on a single vector processor [5]. The parallel results are identical to the serial results.

As mentioned before, the three keys to improve parallel performance is to balance the load, shorten message routine path lengths, and minimize the number of message passings between nodes. Since for 1D parallelization, the load balance is already achieved, performance evaluation was concentrated on the latter two. In the next section, parallel performance of the logical and serpentine sequence mapping schemes will be compared using mesh systems of $(node \times 48 \times 48)$, where $node$ equals 4, 8, 16, 32, 64, 256, 384, and 512; performance comparison for different number of message passings will be carried out using $(node \times 48 \times 48)$ and $(node \times 96 \times 96)$ mesh systems. For the pencil grouping parallelization scheme, the three keys to improve parallel performance still apply. The pencil grouping performance will be reported as well.

All the parallel performances were evaluated based on the timing data obtained from the execution phase and data output phase of the codes. The execution phase includes updating the fields at all grid points from the first time level up to the last time level of the simulation; the data output phase includes writing the calculated field results and the coordinates of the grid system to the disk for post processing. The program initialization time of the present code is negligible compared to the program execution and data output time; therefore, it will not be reported here. (In the following text, data output is sometime referred to as data I/O since the output performance is tied into the I/O performance of the computer system.)

The execution times were collected at the 480th time level. The duration of 480 time steps was selected for all calculations such that the wave traversed more than ten times the distance across the entire computational domain. This time duration is deemed sufficient for the numerical procedure to yield meaningful results

and repeatable timing data. From the execution time, the data processing rate and scale factor are derived. At each time level and grid point, both one-dimensional and the pencil grouping approach must perform at least 492 mixed integer and real number arithmetic operations. The data processing rate is computed by the total number of arithmetic operations performed during the 480 time steps divided by the maximum and the minimum time elapsed of all nodes in use. These minimum and maximum values bracket the range of performance among nodes. In other word, the data processing rate in Gigaop (10^9 arithmetic operations per second) is calculated by multiplying the numbers of iterations, arithmetic operations, and total grid points, then dividing by the executing time ($480 \times 492 \times (IL \times JL \times KL) / (\text{execution time} \times 10^9)$). This calculated data rate is a conservative estimate because the number 492 does not include 47 basic library function calls and nine system message passing calls at every time step. These library function calls include mostly trigonometry and square root calculations. Together with the system message passing calls, they may account for a significant amount of the execution time. The scale factor of the code is defined by the time elapsed for each array of nodes used then normalized by the execution time required for four nodes. The execution time for the four-node calculation was used as timing basis because in the present code, at least four grid points are required to specify the boundary conditions at the dipole and at the far field.

The data output phase of the one-dimensional parallelization scheme requires 78 arithmetic operations and 38 system message passing calls. Most of the 38 system calls are either synchronous or asynchronous message passing instructions to generate one unformatted field data file and three unformatted grid files. The field data file contains all six components of the electromagnetic field at every grid point; and the grid files contain the three coordinates of the grid system. The longest and the shortest time periods required to output those unformatted files for 4-node up to 512-node simulations were recorded. From these timing data, the scale factor for each simulation was again normalized by the 4-node result to determine the possible performance degradation of data management.

5 Discussion of Results

5.1 Mesh refinement study

The originally planned mesh refinement included mesh systems of $(48 \times 48 \times 48)$, $(96 \times 96 \times 96)$, and a finest mesh system of $(192 \times 192 \times 192)$. However, as the number of processors increased beyond 96, the disparity in execution times among processors grew to a factor of 11.6 for 108 nodes, and 14.43 for 144 nodes. In other

words, the observed scalable performance of the present computer program for the cases of $(48 \times 48 \times 48)$ and $(96 \times 96 \times 96)$ was not sustainable for the mesh system of $(192 \times 192 \times 192)$. Therefore, the mesh refinement study was forced to reduce the scope.

Three mesh systems of $(24 \times 24 \times 24)$, $(48 \times 48 \times 48)$, and $(96 \times 96 \times 96)$ were used for the numerical resolution study instead. For this reduced scope of numerical experiment, the coarse mesh system has only 24 grid points in each coordinate. The mesh point density is sufficient to resolve the wave motion [1,2] away from the dipole, but it may be deficient in simulating the singular field behavior near the dipole [11,12].

The mesh refinement results for the radial component of the electric field are presented in Figure 2. The calculation from the $(24 \times 24 \times 24)$ mesh system revealed significant numerical oscillations in an attempt to overcome the large truncation error near the dipole. As shown in Figure 2, the results exhibits a steady improvement as the mesh systems becomes finer. However, the finest mesh is still not fine enough to overcome the stringent demand for accurate simulation near the dipole. Nevertheless, the present numerical procedure has demonstrated the robustness in treating the problem containing a singular behavior.

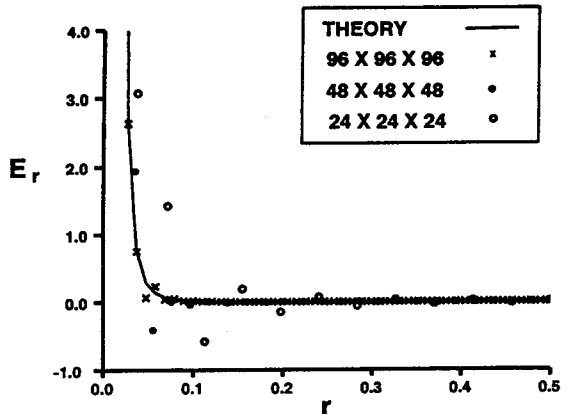


Figure 2: Comparison of computed radial components of the electric fields with theory

Figure 3 depicts the numerical results of the circumferential component of electric intensity on the three mesh systems. The numerical result obtained on the finest mesh attained the best agreement with the analytical result. The maximum deviation from the theoretical results is merely a fraction of one percent. Another desired feature of the characteristic-based formulation also stands out. At a non-dimensionalized radial dis-

tance of 0.14 and beyond, all three solutions agree well with the theory and show no wave reflection from the truncated numerical boundary.

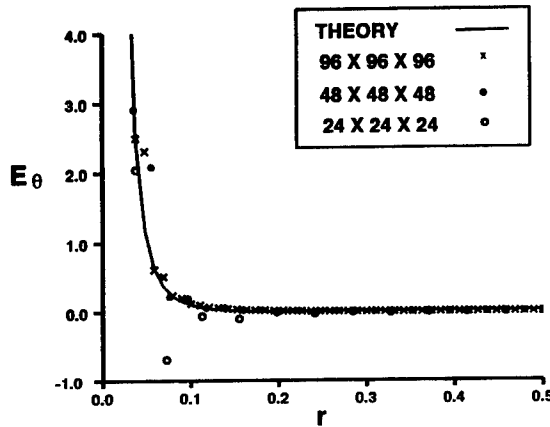


Figure 3: Comparison of computed circumferential components of the electric fields with theory

The comparison of magnetic azimuthal component of the three mesh systems is given in Figure 4. Although the leading term singularity of the magnetic field has a lower order asymptote than that of the electric field, the numerical solutions of the magnetic field generated on the three mesh systems behave similarly to those of the circumferential electric field component. The numerical resolution produced by the finest mesh system, however, is able to suppress the numerical oscillation near the dipole. Finally, the reflected wave from the truncated numerical boundary is completely absent.

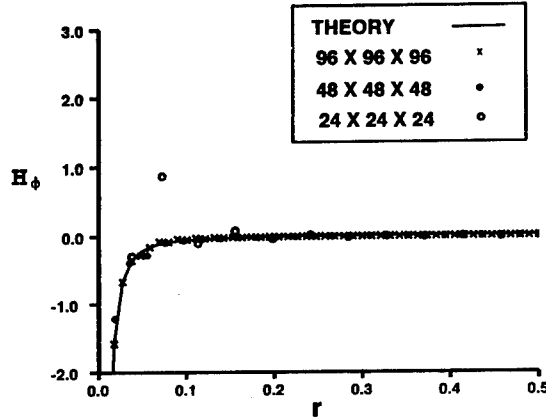


Figure 4: Comparison of computed azimuthal components of the magnetic fields with theory

5.2 Serpentine sequence vs. logical sequence

In this experiment, the one-dimensional parallelization scheme and the grid system ($node \times 48 \times 48$) were used so that every node performs exactly the same amount of computations and writes out the same amount of outputs.

Table 2 shows the data processing rates in Gigaops. The performance difference between the logical sequence and the serpentine message path arrangements begins to appear for the number of nodes beyond 128. Since the serpentine arrangement took advantage of the nearest neighbor priority in message passing hierarchy, the performance degradation is less than that of the logical sequence. In fact, to complete a 512-node computation using serpentine procedure, the slowest node required only 3.1 percent more execution time than the fastest node; whereas, in the logical sequence arrangement, the slowest node is 10.4 percent slower compared with the fastest node. For the same 512-node simulation, the fastest node operating on the serpentine arrangement attained a data processing rate of 5.966 Gigaops; while the fastest node on the logical sequence arrangement only attained 5.412 Gigaops.

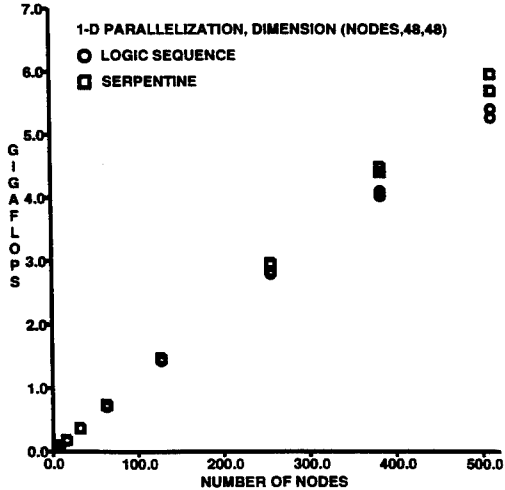


Figure 5: Data processing rates on the Delta

The data processing rates of the serpentine and logical sequences are plotted in Figure 5. The improved data processing rate of the serpentine sequence over that of the logical sequence is clearly demonstrated. As can be seen from the figure, the performance of the logical sequence, which did not honor the data passing priority of the nearest neighbor hierarchy, started to lag behind that of the serpentine sequence when more than 128 numeric nodes were used. From this experiment, the serpentine procedure appears to be more effective for the distributed memory system. However, for both sequences, an increasing disparity of the data processing

Number of nodes	Serpentine		Logical Sequence	
	Maximum	Minimum	Maximum	Minimum
4	0.046	0.046	0.046	0.046
8	0.092	0.092	0.092	0.092
16	0.184	0.184	0.184	0.169
32	0.368	0.368	0.369	0.369
64	0.738	0.738	0.736	0.707
128	1.472	1.472	1.445	1.430
246	2.967	2.952	2.829	2.798
384	4.490	4.413	4.105	4.028
512	5.966	5.704	5.412	5.274

Table 2: Comparison of data rates between serpentine and logical sequences of an $(node \times 48 \times 48)$ mesh system

rate among nodes was noted as the number of nodes increased beyond 64.

The scale factors of the two mapping schemes are demonstrated in Figure 6. All data processing rates are normalized by the value of the 4-node simulation. The superior scalable property of the serpentine sequence over that of the logical sequence is obvious. The scalability of the present code up to 512 nodes is perceived within a performance degradation of less than 3.1 percent. In fact, the significant degradation only appeared when all 512 numeric nodes were employed.

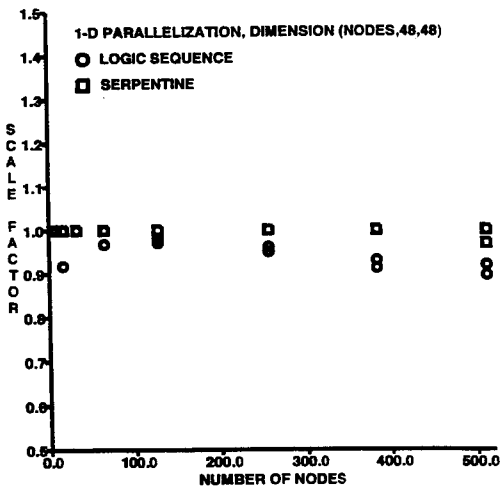


Figure 6: Scalability of executing time on the Delta

Figure 7 presents the data output time in seconds. The data output time varied widely from 0.24 to 32.20 seconds for the serpentine sequence, and from 0.28 to 162.80 seconds for the logical sequence. The shortest waiting time over the entire range of nodes used was only 0.24 seconds. Unfortunately, the aggregated time required by the slowest node in computation and data output actually determines the completion of a numerical simulation. From Figure 7, the data output time in-

creases almost linearly with the number of nodes in use. For the 512-node calculations, the serpentine sequence used 32.2 seconds while the logical sequence needed 162.8 seconds to output the same amount of data.

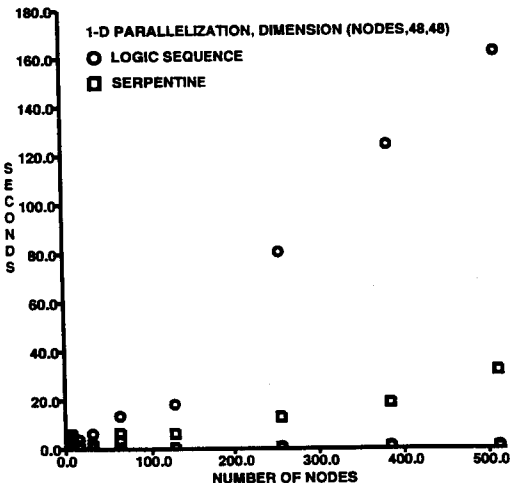


Figure 7: Data I/O time on the Delta

Figure 8 depicts the widely varying data I/O performance among nodes for the entire range of available nodes. Again the performance degrades rapidly as the number of nodes in use increases. The logical sequence yields the maximum parallel performance discrepancy among nodes. The ratio between the most and least efficient nodes is as high as 580.4. The serpentine sequence reduces the disparity to a value about 134.2. If this behavior is a common trend for all distributed memory computer systems, this deficiency shall be a pacing item for research in concurrent computing.

Concurrent performance, similar to those discussed above, were also observed for $(96 \times 96 \times 96)$ and $(96 \times 192 \times 192)$ computations. The data processing rate per node was maintained in the range of 12.89 to 11.65 Megaops. These data processing rates are far be-

low the nominal 60 to 80 Megaops performance level of the i860 microprocessor [13]. Additional performance improvement of the present numerical procedure using the Delta system is still possible.

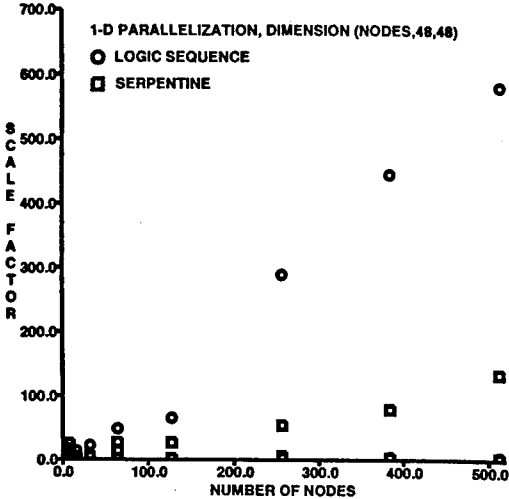


Figure 8: Non-scalability of data I/O on the Delta

5.3 Comparison between $(node \times 48 \times 48)$ and $(node \times 96 \times 96)$ mesh systems

For the one-dimensional parallelization scheme, the vector length is doubled and the message passing length is quadrupled from the coarse grid of $(node \times 48 \times 48)$ to the refined grid of $(node \times 96 \times 96)$. Since the serpentine mapping scheme was proven to give better parallel performance, it was used for the experiment reported in this subsection.

For the $(node \times 48 \times 48)$ systems, the execution time for each node varied from 45.61 to 52.90 seconds regardless of whether the computations were conducted on 4 or 512 numeric nodes. For the $(node \times 96 \times 96)$ case, the execution time ranges from 158.37 to 173.16 seconds. The data processing rates based on the above execution time is given in Table 3. The maximum data processing rate of the refined mesh system is 9.8 percent greater than the coarser mesh computation; and the highest achieved value was 6.551 Gigaops. Apparently at a message passing length of 36,864 bytes and 8 message passings per node per time step, the higher data processing rate by a greater vector length has not been hampered by the limiting memory bandwidth. As a result, the deviation between the fastest and the slowest execution rates is less than one percent.

The execution times expressed in scale factors for the $(node \times 96 \times 96)$ and $(node \times 48 \times 48)$ systems are shown in Figure 9. Small variations of data processing rates for both grid systems were observed over the

entire range of nodes used. The results of the coarse grid computations exhibited a wider performance deviation among nodes than the finer grid calculations. The latter, however, also degraded noticeably from the 4-node to the 8-node result. The difference is about 4.6 percent. As the number of nodes increases to 512, the degradation of scalability of the present procedure reached the maximum value of 7.6 percent. But the major portion of the performance deficiency is incurred at the 4-node to 8-node transition. In all, the present algorithms mapped to Delta system has demonstrated an acceptable scalability of data processing rate up to a grid system consisting of $512 \times 96 \times 96$ grid points.

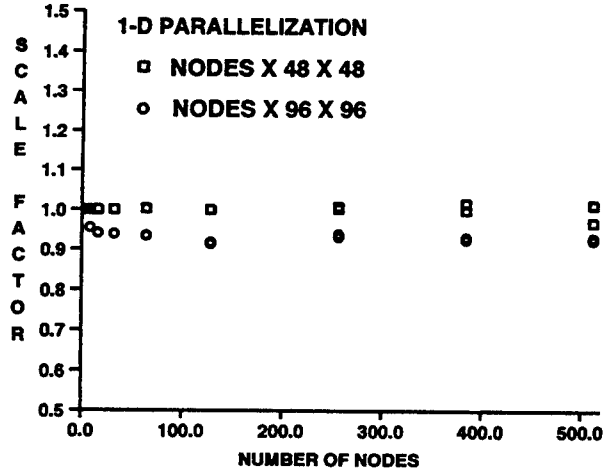


Figure 9: Execution time scale factors for the coarse and fine mesh systems

The data output time varies from 0.2369 to 32.20 for the coarse grid system and from 0.1324 seconds for the 16-node calculation to 30.02 seconds for the 512-node simulation for the finer grid system. Figure 10 shows the scale factors of the output timing results for the coarse and refined mesh systems. Clearly, the I/O performance degrades nearly linearly as the number of nodes in use increases. The worst I/O performance occurred when all 512 nodes were engaged. In this case, the fastest and the slowest nodes used 11.51 and 226.8 times, respectively, the time required to output the same amount of data as the fastest node of the 16-node computation. This observation further asserts that the scalable I/O performance shall be a pacing item for research in concurrent computing.

5.4 Pencil grouping scheme

Owing to similar peculiarities of the Delta compiler observed for the one-dimensional parallelization, only a limited number of timing data from the pencil partition is obtained at present time. In short, the serpentine sequence did improve the performance over that

Number of nodes	node \times 96 \times 96		node \times 48 \times 48	
	Maximum	Minimum	Maximum	Minimum
4	0.055	0.055	0.046	0.046
8	0.105	0.105	0.092	0.092
16	0.207	0.207	0.184	0.184
32	0.413	0.413	0.368	0.368
64	0.823	0.822	0.738	0.738
128	1.616	1.609	1.472	1.472
246	3.305	3.278	2.967	2.952
384	4.915	4.884	4.490	4.413
512	6.551	6.505	5.966	5.704

Table 3: Comparison of data rates between $node \times 96 \times 96$ and $node \times 48 \times 48$ mesh systems

Delta (m,n)	$IL \times JL$ (Pencil Dimension)													
	192x1	96x2	64x3	48x4	32x6	24x8	16x12	12x16	8x24	6x32	4x48	3x64	2 x96	1x192
(6,32)	13.4	9.73	10.6	10.7	12.1	13.1	14.2	15.7	16.8	16.8	16.7	14.3	13.2	8.94
(8,24)	12.6	10.6	11.6	12.1	13.0	13.9	15.7	16.8	17.3	16.4	16.9	14.0	13.2	9.55
(12,16)	12.5	10.6	12.0	13.1	14.0	15.7	17.0	18.2	17.3	16.8	16.5	14.2	13.3	9.75
(16,12)	13.1	11.3	13.1	13.9	15.4	16.2	18.4	17.5	17.1	16.2	14.3	13.2	13.2	10.1

Table 4: Execution rates (Megaops) for a $(192 \times 192 \times 192)$ grid system by pencil grouping scheme

of the logical sequence as the one-dimensional case. The timing information for a $(192 \times 192 \times 192)$ mesh system mapped to the Delta using pencil grouping scheme with various combinations of pencil dimension ($IL \times JL$) and Delta partition (m, n) is tabulated in Table 4. The variation of data processing rates among the different pencil partitions for a fixed Delta partition is significant. In general, slower performance is observed when the pencil dimension and Delta partition are at the extreme situations when the pencil grouping scheme degenerates into one-dimensional parallelization. For example, the pencil dimensions of (192×1) or (1×192) on a Delta partition of $(6,32)$ has a slower data processing rate of 13.2 or 8.94 Megaops, respectively.

A general performance improvement for an $(IL \times JL)$ pencil dimension is noted when IL nearly equals JL . The best performance for a given Delta partition is observed when IL equals m and JL equals n , as underlined in Table 4. The timing data of the pencil partition has revealed a parallel efficiency gain of 37% over that of the one-dimensional partition.

6 Conclusions

A fractional-step, upwind numerical procedure for solving the three-dimensional, time-domain Maxwell equations has been ported to the Intel Touchstone Delta multicomputer. The concurrent computations duplicated the results from earlier numerical results and

compared well with theory. For the mesh systems of $(node \times 48 \times 48)$ and $(node \times 96 \times 96)$, the numerical procedure is scalable up to 512 numeric nodes with only up to 7.6 percent performance degradation. The fastest data processing rate is 6.551 Gigaops and the sustained overall performance is clocked at 5.704 Gigaops. Further increased data processing rate is still possible.

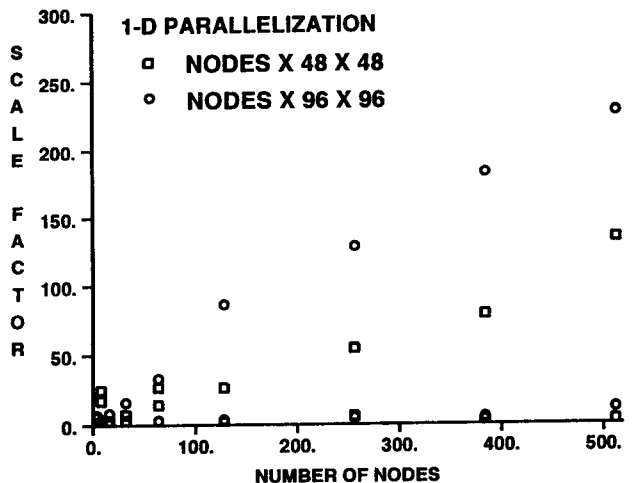


Figure 10: I/O scale factors for the coarse and fine mesh systems

The scalability of concurrent computing is sustained up to a simulation eight times the size of the baseline case. The scalable performance failed at the

fourth level of grid point enrichment ($192 \times 192 \times 192$). Although the architecture of the Touchstone Delta multicomputer and its usefulness are impressive, consistent performance in scaling up for massive data bases remains as a necessary research emphasis. The scalable data I/O is also identified as a pacing item for intense research for attaining high performance computation.

The one-dimension parallelization has been shown as a suitable data partition procedure for a characteristic-based, windward difference algorithm in solving the time dependent, three dimensional Maxwell equations. Further parallel efficiency improvement by pencil structure shows developable potential.

Acknowledgement The computing resource was provided by the Intel Touchstone Delta System operated by Caltech on behalf of the Concurrent Supercomputing Consortium. Access to this facility was granted by Dr G. Weigand of ARPA. Stimulating and fruitful discussions with Stephen J. Scherr and B.G. Vikstrom are also appreciated.

References

1. Taflove, A., Re-Inventing Electromagnetics: Supercomputing Solution of Maxwell's Equations Via Direct Time Integration on Space Grids, Computing Sys. in Engineering, Vol. 3, Nos 1-4, 1992, pp. 153-168.
2. Shankar, V., Hall, W. F., and Mohammadian, A. H., A Time-Domain Differential Solver for Electromagnetic Scattering Problems, Proceedings of IEEE, Vol. 77, No. 5, May 1989.
3. Shang, J. S., Characteristic-Based Methods for the Time-Domain Maxwell Equations, AIAA Paper 91-0606, presented at AIAA meeting held in Reno, NV, January 1991
4. Shang, J. S., A Characteristic-Based Algorithm for Solving 3-D, Time-Domain Maxwell Equations, AIAA Paper 92-0452, presented at AIAA meeting held in Reno, NV, January 1992.
5. Shang, J. S., A Fractional-Step Method for Solving 3-D, Time-Domain Maxwell Equations, AIAA Paper 93-0461, presented at AIAA meeting held in Reno, NV, January 1993.
6. Roe, P. L., Characteristic-Based Schemes for the Euler Equations, Ann Rev. Fluid Mech., Vol 18, 1986, pp 337-365.
7. Steger, J. L., and Warming, R. F., Flux Vector Splitting of the Inviscid Gasdynamics Equations with Application to Finite Difference Methods, J. Comp. Phys. Vol. 40, No. 2, February 1987, pp 263-293.
8. MacCormack, R. W., and Candler, G. V., The Solution of the Navier-Stokes Equations Using Gauss-Seidel Line Relaxation, Computer & Fluid Vol. 17, No. 1, 1989, pp 135-150.
9. Wesley, R., Wu, E., and Calahan, D. A., A Massively-Parallel Navier-Stokes Implementation, AIAA Paper 89-1940CP, 1989.
10. Scherr, S. J., Implementation of an Explicit Navier-Stokes Algorithm on a Distributed Memory Parallel Computer, AIAA Paper 93-0063, January 1993.
11. Harrington, R. R., Time-Harmonic Electromagnetic Fields, McGraw-Hill Book Co., New York, 1961.
12. Jordan, E. C., Electromagnetic Waves and Radiation System, Prentice-Hall, Inc., NJ, 1960.
13. Intel Corporation, Touchstone Delta System User's Guide, Publication 312125-001, October 1991.

ON THE APPLICABILITY OF THE BICONJUGATE GRADIENT FFT METHOD FOR THE THIN CONDUCTING PLATE PROBLEM

T. V. TRAN and A. McCOWEN,

Department of Electrical and Electronic Engineering,
University of Wales Swansea,
Singleton Park,
Swansea SA2 8PP
United Kingdom.

ABSTRACT: The application of the Biconjugate Gradient FFT method to the thin conducting plate problem is investigated. Upon comparing with a Conjugate Gradient FFT method, it is found that the Biconjugate Gradient solution requires a relatively larger error tolerance to achieve a comparatively well-behaved current distribution. Coupled with the requirement of only one matrix–vector product per iteration, the computational cost of the Biconjugate Gradient method is, thus, much smaller than those previously reported in the literature. Of particular importance is the use of the incident electric field as a starting estimate to alleviate the non-convergence behaviour which is usually associated with the application of a Biconjugate Gradient approach to conducting plates at grazing angle. For other angles of incidence, it is shown that this procedure also accelerates the resulting convergence rates as compared to those obtained by simply using zero as an initial estimate.

1. INTRODUCTION

The application of FFT-based methods for the flat, conducting plate problem has been receiving a lot of attention in the computational electromagnetics community since the late 1980s. Most of these use the Conjugate Gradient method (CGM) [1] as the iterative algorithm in conjunction with the fast Fourier transform (FFT) to solve for the discretized matrix equation [2]–[6]. This combination, commonly known as the CGFFT method, is attractive both in the characteristics of convergence associated with the CGM and the reduced computational costs associated with using the FFTs to approximate all occurring convolutions.

The finite-termination property of the CGM is, however, only valid when the defining matrix (or operator) of the linear system to be solved is Hermitian and positive-definite (HPD). For other types of systems, it is necessary to premultiply (implicitly) both sides of the pertinent system by the Hermitian version A^* of the matrix A so that the resulting matrix is HPD. The latter system, often referred to as the *normal equation*, is, however, more ill-conditioned than the original system, which, in turn, makes the convergence rate of the resulting algorithm slower than that associated with the original system. For this reason, it is worthwhile exploring iterative algorithms that can be applied directly to the system of equations in mind.

One such method is the Biconjugate Gradient (Bi-CGM) method, first developed by Lanczos for finding the eigenvalues of an unsymmetric system [7] and later extended by Fletcher [8] and Jacobs [9] to treat complex indefinite systems. When applied to a symmetric system, the Bi-CGM has one more advantage over the CGM in that only one matrix–vector operation is needed within each iteration step [10]. The combination of the Bi-CGM with the FFT to solve a convolutional matrix equation is also possible in exactly the same way as a conventional CGFFT formulation. Despite this, there are only a few applications of the Bi-CGFFT method to electromagnetic scattering problems in the literature compared with the abundance of solutions obtained by its CGFFT counterpart. Recent works on the performance of the Bi-CGFFT for conducting problems have, however, put the Bi-CGFFT in a very favourable position compared with a conventional CGFFT approach [11]–[12].

In this paper, the performance of the Biconjugate Gradient FFT method when applied to a thin conducting plate under plane-wave incidence is investigated. The non-convergence behaviour which usually happens when the Bi-CGFFT is applied to a conducting plate at grazing incidence is overcome by choosing the initial guess to be the incident electric field \mathbf{E}^i . A systematic study is also conducted of the dependence of the Bi-CGFFT method on the use of this initial estimate procedure for other angles of incidence. Greatly accelerated rates of convergence is shown to result when \mathbf{E}^i is used as an estimate for the initial unknown current distribution instead of simply using zero as commonly adopted in most FFT-based implementations. The layout of the paper is as follows. Section 2 shows the functional form of the Bi-CGM when applied to a symmetric, indefinite system. This is followed by Section 3 which deals with the numerical solutions obtained by the Bi-CGFFT and the CGFFT methods for a variety of incident configurations. Finally, Section 4 draws the conclusion on the applicability of the Bi-CGFFT based on the results obtained in Section 3.

2. THE BICONJUGATE GRADIENT METHOD FOR SYMMETRIC COMPLEX SYSTEMS

Table 1 shows the computationally compact form of the Biconjugate Gradient method [10] when applied to a symmetric system of the form

$$AJ = E^i, \quad (1)$$

where J denotes the unknown current distribution to be solved for. The impedance matrix A on the left-hand side of (1) represents the couplings between the different cells on the plate and is often formulated in discrete-convolutional form to enable the FFT to be efficiently applied whenever there is a matrix–vector to be computed [6].

```

Choose an initial guess  $J^{(0)}$ ;  $n = 0$ 
 $F^{(0)} = E^i - AJ^{(0)}$ ;  $p^{(0)} = F^{(0)}$ 
while  $\|F^{(n)}\| / \|F^{(0)}\| > \epsilon$  do
     $\alpha^{(n)} = \frac{\langle F^{(n)*}, F^{(n)} \rangle}{\langle p^{(n)*}, Ap^{(n)} \rangle}$ 
     $J^{(n+1)} = J^{(n)} + \alpha^{(n)} p^{(n)}$ 
     $F^{(n+1)} = F^{(n)} - \alpha^{(n)} Ap^{(n)}$ 
     $\beta^{(n)} = \frac{\langle F^{(n+1)*}, F^{(n+1)} \rangle}{\langle F^{(n)*}, F^{(n)} \rangle}$ 
     $p^{(n+1)} = F^{(n+1)} + \beta^{(n)} p^{(n)}$ 
     $n = n + 1$ 
end while

```

Table 1: The generalized Biconjugate Gradient algorithm for a complex, symmetric indefinite system.

Apart from the definition of the inner product (to calculate $\alpha^{(n)}$ and $\beta^{(n)}$), the form of the Biconjugate Gradient method presented in Table 1 is almost identical to a classical Conjugate Gradient formulation for a real and symmetric positive-definite (SPD) system [1]. In both methods, only one matrix–vector product in the form of $Ap^{(n)}$ is required at each iteration step. For complex indefinite systems, however, the CGM has to be modified to avoid the possible division by zero and substantial error growth when this situation is nearly reached [8]. The main resulting cost is an extra matrix–vector product in the form of $A^*F^{(n)}$, where A^* denotes the complex conjugate of the matrix A [1], [10]. Thus, the computational cost associated with a symmetric indefinite Bi–CGM approach is expected to be half of those required in a CGM formulation when applied to the same problem¹.

The convergence criteria for a Biconjugate Gradient FFT method is specified in the same way as for its Conjugate Gradient counterpart. Let $F^{(n)}$ denotes the

1. For non-symmetric systems, the application of a Biconjugate Gradient method still requires two matrix–vector products per iteration step. However, as most EM scattering formulations are symmetric in nature, the algorithm with reduced costs is applicable.

residual field at the n^{th} step, then the stopping criteria is defined in terms of the *normalized residual norm*,

$$\frac{\|F^{(n)}\|}{\|F^{(0)}\|}, \quad (2)$$

where $F^{(0)}$ denotes the initial field residual and $\| \cdot \|$ denotes the norm of a complex vector. At each step, (2) is compared to an *error tolerance* ϵ which is specified by the user. The usual stopping criteria for a well-behaved CGFFT solution is 0.01 [5]–[6], but as will be demonstrated in the next section, the corresponding value for a Bi–CGFFT solution can be much larger, thus reducing considerably the required number of iterations, and thus computational costs.

An important parameter which is often neglected in other Biconjugate Gradient formulations is the form of the initial guess $J^{(0)}$. It is often assumed that this is taken to be zero. In Section 3, we demonstrate that choosing the initial guess to be the incident electric field E^i , not only alleviates the non-convergence problem that is usually associated with the application of the Bi–CGFFT at grazing incidence, but also helps to accelerate the convergence rates associated with other angles of incidence.

3. A COMPARATIVE STUDY OF COMPUTATIONAL EFFICIENCIES OF THE BI–CGFFT AND CGFFT METHODS FOR THE THIN CONDUCTING PLATE

In this section, the performance of the Bi–CGFFT method when applied to the pulse-basis formulation recently proposed by Tran and McCowen [6] is investigated. For each incident configuration, a comparison is made with a corresponding CGFFT formulation. The fact that the Bi–CGFFT generally requires half the computational workload compared to its CGFFT counterpart when applied to a symmetric system is well-known and has been investigated elsewhere [11], [12]. The aim of this section is to show that the efficiency of the Bi–CGFFT can be enhanced further by virtue of the fact that it needs a relatively larger tolerance to achieve a well-behaved current distribution as that generated by the CGFFT. The importance of the use of the incident electric field as a starting estimate in a Bi–CGFFT formulation will also be investigated. All numerical results are performed on a VAX 8820 computer.

A. Broadside incidence

Fig.1 shows the broadside current distributions obtained by the two FFT-based methods on a $1\lambda_0 \times 1\lambda_0$ square plate using mesh sizes $\Delta x = \Delta y = 0.0303\lambda_0$ with different error tolerances. It can be seen from this figure that the Bi–CGFFT requires a very coarse tolerance to yield a well-behaved solution, as compared with a much finer tolerance as required by the CGFFT to achieve essentially the same results. When applied with the same tolerance as the Bi–CGFFT, i.e. $\epsilon = 0.1$, the CGFFT results are hardly recognizable. For the x –component, only a vague resemblance of the expected lobes along the front and back edges can be assumed (see [5]–[6] for a discussion of these

results with respect to different discretization procedures); the ripples in the centre of the scattering plate are too high in comparison with the edge lobes. The behaviour of the y -component at the same error tolerance is even more out of shape: the lobes along the four edges are nearly of the same amplitudes, as are the ripples in the centre of the scattering plate. Although these anomalies are self-corrected at the finer tolerance of $\epsilon = 0.1 * 10^{-1}$, the resulting computational cost is much higher compared with the corresponding Bi-CGFFT: the CPU times required by

the CGFFT on a VAX 8820 is 08:40 minutes (172 iterations) as compared with only 01:17 minutes (27 iterations) for the Bi-CGFFT—an increase of 676%. Yet there is little difference between the two numerical solutions; the only noticeable discrepancy is in the co-polarized y -component, where the CGFFT current density is slightly smoother along the four edges. The predicted current distribution from the Bi-CGFFT method for the dominant x -component is virtually indistinguishable from its CGFFT counterpart.

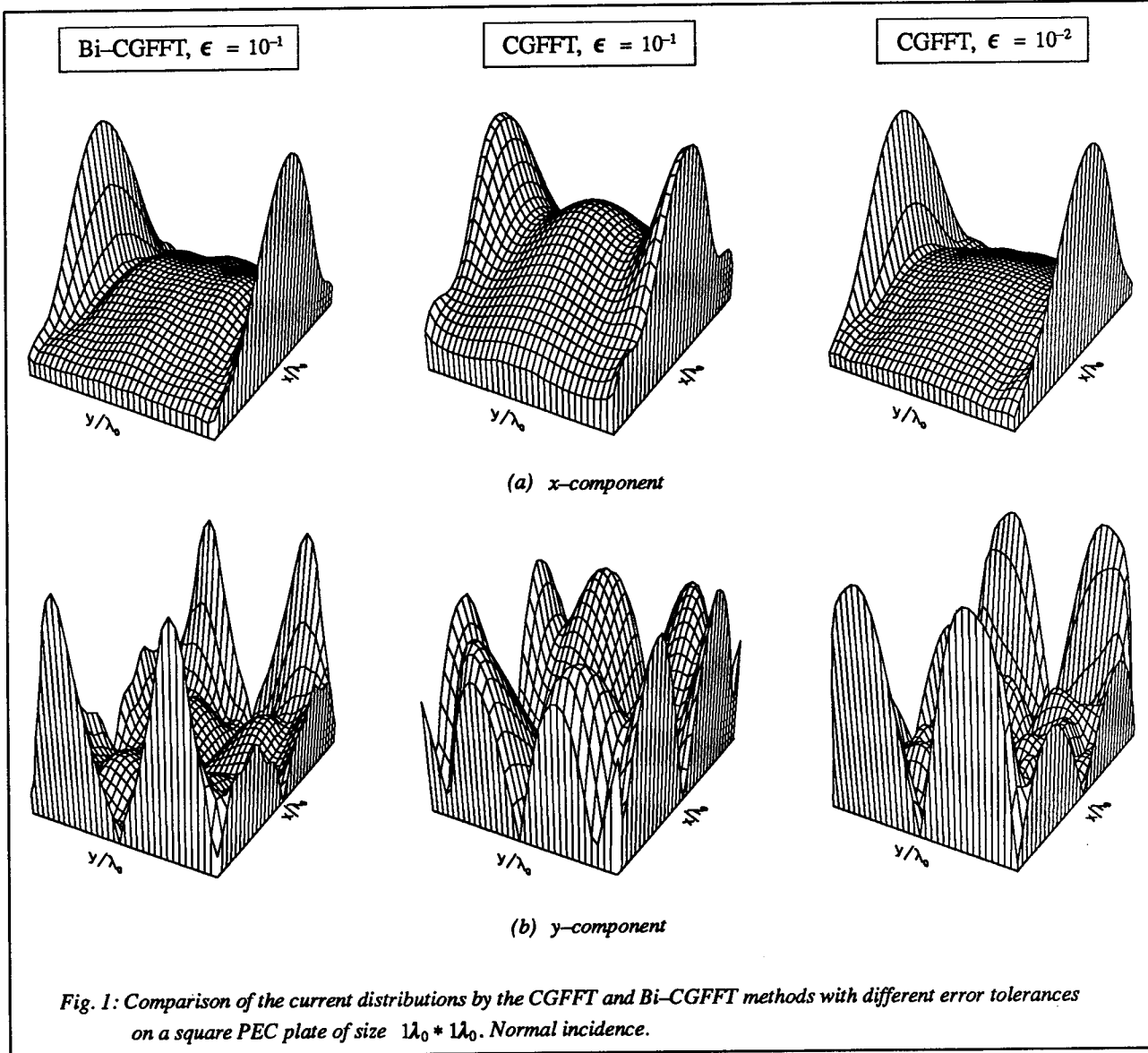


Fig. 1: Comparison of the current distributions by the CGFFT and Bi-CGFFT methods with different error tolerances on a square PEC plate of size $1\lambda_0 * 1\lambda_0$. Normal incidence.

B. Grazing incidence

An important incident configuration of the plate scattering problem is the grazing incidence case. When applied to a geometric shape that possesses edges and corners such as a rectangular plate, the rapidly changing behaviour of the current density near the edge and the corner diffraction effects makes its computation a particularly difficult one [13]. The Bi-CGFFT that gives the solution for the broadside incidence in Fig. 1 fails to give a convergent result when the plate is subject to the grazing

angle. This undesirable behaviour, commonly known as the *stagnation problem*, arises when the constant $\alpha^{(n)}$ becomes close to machine-zero and causes both the current density $\mathbf{J}^{(n+1)}$ and field residual $\mathbf{F}^{(n+1)}$ to be non-incremental as the iteration step is increased (see Table 1). Furthermore, since $\mathbf{F}^{(n+1)}$ is then of approximately the same value as $\mathbf{F}^{(n)}$, the inner product $\langle \mathbf{F}^{(n+1)*}, \mathbf{F}^{(n+1)} \rangle$ is then also approaching

machine-zero and thus, no new direction vector can be created for the advancement of the unknown current vector. The algorithm then becomes stagnated and no meaningful solution can be obtained no matter how many more steps are added.

A simple remedy which involves restarting the iterative solution with a small perturbation of the zero initial estimate — commonly adopted in most FFT-based implementations— has been suggested by Smith, Peterson and Mittra [12]. However, tests performed by the authors using their *ad-hoc* procedure indicated that an erroneous solution may result if insufficient care is taken in choosing the amount of the required perturbation, although convergence is usually alleviated whenever the zero starting vector is slightly perturbed. The extent of perturbation, thus, plays an important role in ensuring both a convergent and correct solution, and since this parameter is not known in advance, general use of Smith *et. al.*'s procedure for scatterers other than a simple conducting strip is fraught with difficulties. For higher-dimensional problems, the perturbations in the different coordinate components at each discretization cell of the computational

domain would best be related to some known quantity of the problem under consideration. At the start of the plate scattering simulation, the only known quantity is the incident field distribution \mathbf{E}^i over the plate. Thus, it is logical that the initial estimate $\mathbf{J}^{(0)}$ should be taken as \mathbf{E}^i .

Fig. 2 shows the current distributions from a H-polarized grazing incidence achieved with this initial estimate procedure. Also included are the CGFFT solution at two different error tolerances. It is clear from this figure that the same behaviour is observed for this configuration as for the broadside case of Fig. 1, i.e. the Bi-CGFFT method requires a much larger error tolerances than its CGFFT counterpart when applied to the same problem. The numerical results associated with the CGFFT method at the tolerance sufficiently required by the Bi-CGFFT are, again, not recognizable — particularly in the y -component, where the spikes at the back corners are certainly non-physical. The final results for the Bi-CGFFT at $\epsilon = 0.3$ and the CGFFT at $\epsilon = 0.5 * 10^{-1}$ are virtually the same.

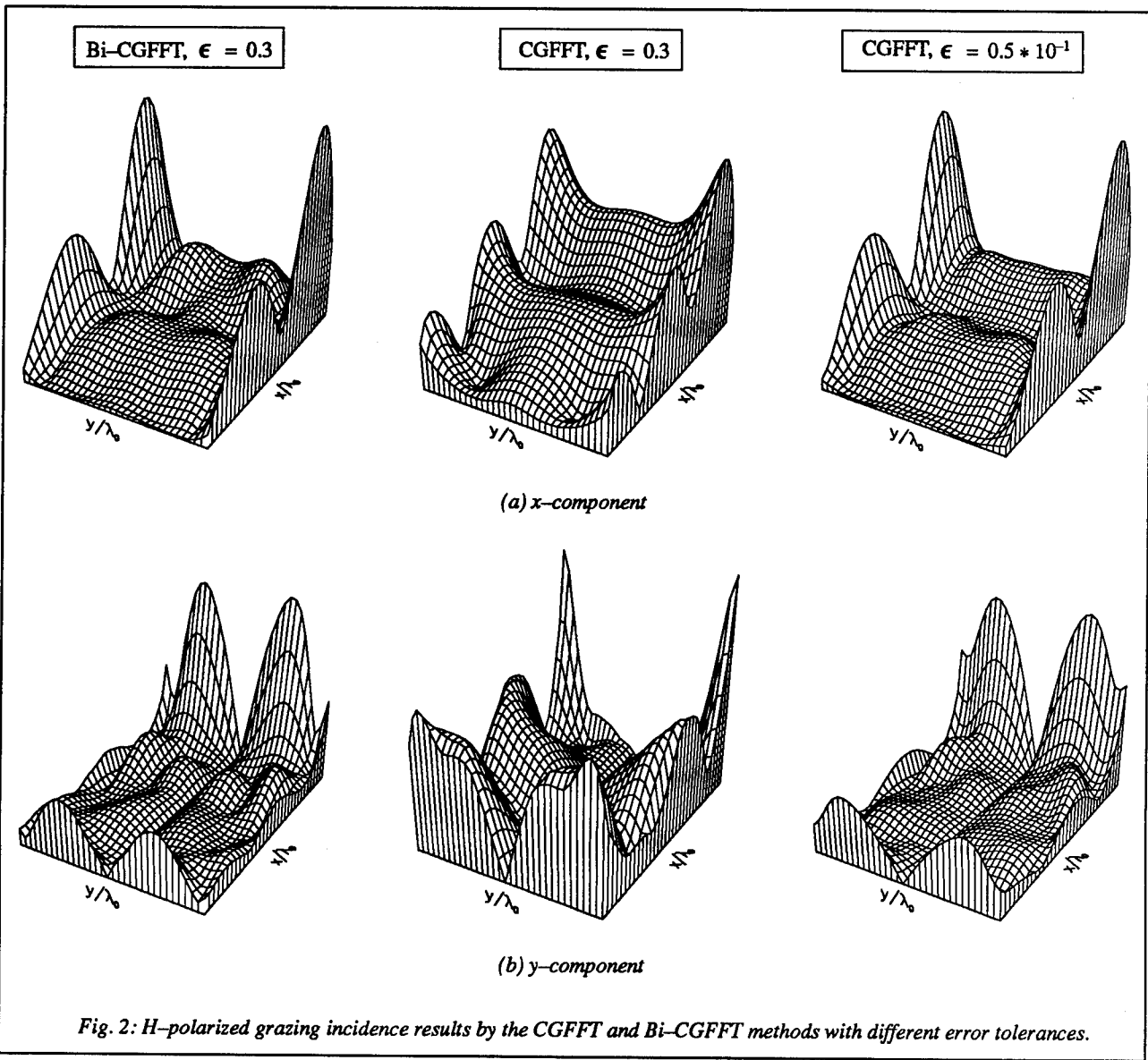
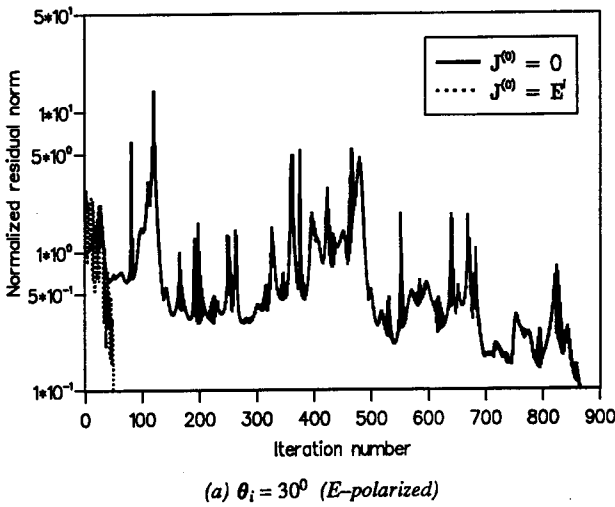


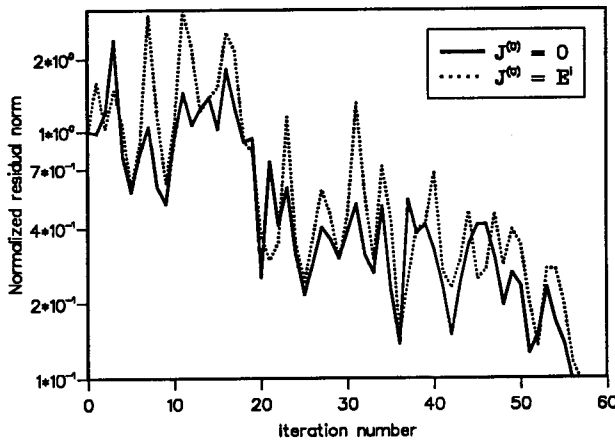
Fig. 2: H-polarized grazing incidence results by the CGFFT and Bi-CGFFT methods with different error tolerances.

C. Oblique incidences

Next, the use of \mathbf{E}^i as an initial estimate for other angles of incidence is investigated. Fig. 3 shows the convergence rates of the Bi-CGFFT method when subject to two arbitrary oblique angles of incidence. The erratic behaviours of the two convergence curves are the consequences of the fact that successive residual norms in a Biconjugate Gradient formulation need not satisfy the inequality $\| \mathbf{F}^{(n)} \| < \| \mathbf{F}^{(n-1)} \|$ at all iteration steps as would be expected in a CGFFT formulation.



(a) $\theta_i = 30^\circ$ (E-polarized)



(b) $\theta_i = 45^\circ$ (H-polarized)

Fig. 3: Comparison of convergence rates between the two methods of estimating the initial unknown from a Bi-CGFFT solution.

It is worth emphasizing, however, that, barring the case of non-convergence for certain grazing incidences, the theoretical finite-termination property of a Biconjugate Gradient approach is still obtainable as with a Conjugate Gradient formulation, albeit with infinite-precision arithmetics [9]. However, as Fig. 3 (a) clearly shows, using \mathbf{E}^i as an initial estimate can substantially reduce the computational cost required to achieve convergence as compared with simply using zero. The increase in iteration count by using $\mathbf{J}^{(0)} = 0$ in this case is a staggering 1680%.

A similar increase rate has also been recorded for the near-grazing angle of 89° , where although convergence is achieved, the huge computational cost makes it necessary to use \mathbf{E}^i as an initial estimate instead of zero. On the other hand, the detrimental effect of using $\mathbf{J}^{(0)} = \mathbf{E}^i$ at $\theta_i = 45^\circ$ in Fig. 3 (b) is minimal.

The convergence behaviours of the two angles in Fig. 3 are typical of a Bi-CGFFT solution when used with two different initial estimate procedures for other angles of incidence in both polarizations: either the convergence rates are considerably accelerated when $\mathbf{J}^{(0)} = 0$ is replaced by $\mathbf{J}^{(0)} = \mathbf{E}^i$, or only negligible decrease in convergence rate is observed [14]. In most cases, the significant speedup ratios indicate that the incident electric field \mathbf{E}^i should be used as an initial estimate for the unknown current distribution in a Bi-CGFFT method.

D. The effect of using the incident electric field as an initial estimate in a CGFFT formulation

Using \mathbf{E}^i as an initial estimate in a CGFFT formulation is, however, not beneficial to its resulting convergence rate as compared to the usual procedure of simply using $\mathbf{J}^{(0)} = 0$. Fig. 4 shows the convergence rates associated with three arbitrary angles of incidence in a CGFFT solution. The differences in convergence rates associated with the two starting procedures appear to be smaller as the angle of incidence increases. At grazing incidence, where $\theta_i = 90^\circ$, the discrepancy is minimal, whereas at broadside incidence ($\theta_i = 0^\circ$), it is best to use zero as a starting estimate. The study in this section shows clearly that no advantages can be gained by using \mathbf{E}^i as an initial estimate for the unknown current distribution in a CGFFT application and zero distribution should be adopted as a starting estimate whenever a CGFFT approach is used to solve the plate scattering problem.

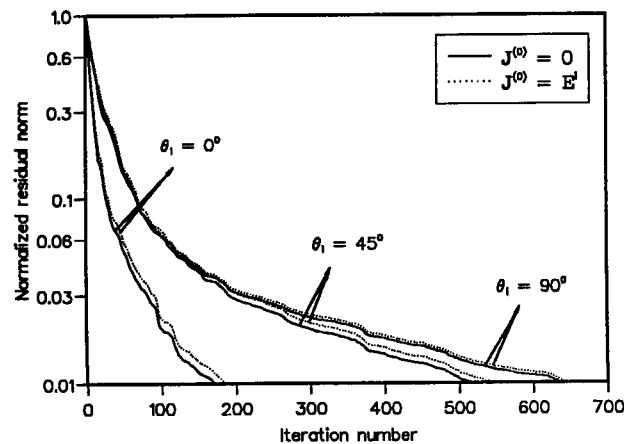


Fig. 4: Comparison of convergence rates of the two methods of estimating the initial unknown with a CGFFT approach on a $1\lambda_0 \times 1\lambda_0$ plate.

I. CONCLUSIONS

In this paper, the applicability of the Biconjugate Gradient FFT applied to a pulse-basis formulation for the conducting plate problem has been demonstrated. The computational cost associated with the Bi-CGFFT is much less than a conventional CGFFT approach due to the reduction of a matrix-vector product per iteration step and a much larger error tolerance to achieve a similar well-behaved result as compared to that obtained by its CGFFT counterpart. The difficulty with non-convergence of the Bi-CGFFT at grazing incidence was alleviated by using the incident electric field \mathbf{E}^i as an initial estimate. Furthermore, it was also demonstrated that using this starting guess procedure also accelerates the convergence rates associated with other angles of incidence.

The use of \mathbf{E}^i as an initial estimate is recently shown to overcome the non-convergence problem associated with the application of the Bi-CGFFT method to 2- and 3-D dielectric bodies [15]. Although the cause of non-convergence is different from that associated with a thin conducting plate, the fact that using $\mathbf{J}^{(0)} = \mathbf{E}^i$ can induce convergence is a particularly pleasing aspect. Although no justification is available to explain for the improvement in convergence rates, this non *ad-hoc* initial starting procedure appears to be mandatory in the successful implementation of a Biconjugate Gradient FFT method.

The Biconjugate Gradient FFT has been increasingly used as an efficient algorithm to solve for the discrete-convolutional system which arises either from a FFT-based formulation similar to that considered in this paper [16], or as part of a hybrid method [17]. The incorporation of the starting guess procedure proposed by the authors in this paper may well help to alleviate any non-convergence problem associated with the application of the Bi-CGFFT to other problems of interest and allay the doubt concerning its consistent performance for computational electromagnetics.

REFERENCES

- [1] M. R. Hestenes and E. Steifel, 'Method of Conjugate Gradients for Solving Linear Systems', *J. Res. Nat. Bur. Stand.*, Vol. 49, No. 152, pp. 409–436, Dec. 1952
- [2] T. J. Peters and J. L. Volakis, 'Application of a Conjugate Gradient FFT Method to Scattering from Thin Planar Material Plates', *IEEE Trans. Ant. Prop.*, Vol. 36, No. 4, pp. 518–526, Apr. 1988.
- [3] C. Y. Shen, K. J. Glover, M. I. Sancer and A. D. Varvatsis, 'The Discrete Fourier Transform Method of Solving Differential-Integral Equations in Scattering Theory', *IEEE Trans. Ant. Prop.*, Vol. AP-37, No. 8, pp. 1032–1041, Aug. 1988.
- [4] M. F. Catedra, J. G. Cuevas and L. Nuno, 'A Scheme to Analyze Conducting Plates of Resonant Size using the Conjugate Gradient Method and the fast Fourier Transform', *IEEE Trans. Ant. Prop.*, Vol. 36, No. 12, pp. 1744–1752, Dec. 1988.
- [5] A. P. M. Zwamborn and P. M. van den Berg, 'A Weak form of the Conjugate Gradient FFT Method for Plate Problems', *IEEE Trans. Ant. Prop.*, Vol. 39, No. 2, pp. 224–228, Feb. 1991.
- [6] T. V. Tran and A. McCowen, 'An Improved Pulse-Basis Conjugate Gradient FFT Method for the Thin Conducting Plate Problem', *IEEE Trans. Ant. Prop.*, Vol. 41, pp. 185–190, Feb. 1993.
- [7] C. Lanczos, 'Solutions of Systems of Linear Equations by Minimized Iterations', *J. Res. Nat. Bur. Stand.*, Vol. 49, No. 1, pp. 33–53, Jul. 1952.
- [8] R. Fletcher, 'Conjugate Gradient Methods for Indefinite Systems', in: *Proc. Dundee Conf. Num. Anal.*, 1975, G. A. Watson, ed., Springer-Verlag, Berlin, pp. 73–89, 1976.
- [9] D. A. H. Jacobs, 'A Generalization of the Conjugate-Gradient Method to Solve Complex Systems', *IMA J. Num. Anal.*, Vol. 6, pp. 447–452, 1986.
- [10] T. K. Sarkar, 'On the Application of the Generalized Biconjugate Gradient Method', *J. Electromagn. Waves Appl.*, Vol. 1, No. 3, pp. 223–242, 1987.
- [11] D. B. Davidson and D. A. McNamara, 'Comparisons of the Application of Various Conjugate-Gradient Algorithms to Electromagnetic Radiation from Conducting Bodies of Revolution', *Microwave Opt. Tech. Lett.*, Vol. 1, No. 7, pp. 243–246, Sep. 1988.
- [12] C. F. Smith, A. F. Peterson and R. Mittra, 'The Biconjugate Gradient Method for Electromagnetic Scattering', *IEEE Trans. Ant. Prop.*, Vol. 38, No. 6, pp. 938–940, Jun. 1990.
- [13] J. S. Hey and T. B. A. Senior, 'Electromagnetic Scattering by Thin Conducting Plates at Glancing Incidence', *Proc. Phys. Soc.*, Vol. 72, No. 468, pp. 981–996, Dec. 1958.
- [14] T. V. Tran, *FFT-based methods for computational electromagnetics*, Ph.D dissertation, Univ. Wales, Swansea, 1993.
- [15] T. V. Tran and A. McCowen, 'A comparison of two FFT-based Methods for Dielectric Scattering Problems', to be published in *Microwave Opt. Tech. Lett.*
- [16] J.-M Jin and J. L. Volakis, 'A Biconjugate Gradient FFT Solution for Scattering by Planar Plates', *Electromagn.*, Vol. 12, pp. 105–119, 1992.
- [17] J. Gong, J. L. Volakis, A. C. Woo and H. T. G. Wang, 'A Hybrid Finite Element-Boundary Integral Method for the Analysis of Cavity-Backed Antennas of Arbitrary Shape', *IEEE Trans. Ant. Prop.*, Vol. 42, No. 9, pp. 1233–1242, Sep. 1994.

1995 INSTITUTIONAL MEMBERS

THE AEROSPACE CORPORATION PO Box 92957 Los Angeles, CA 90009--2957	ANDREW CANADA INC. 606 Beach Street Whitby, Ont, CANADA L1N 5S2	ANDREW CORPORATION 10500 W 153rd Street Orland Park, IL 60462
ARC, INC 8201 Corporate Dr. Ste 3550 Landover, MD 20785	ATEA Raleigh Rd, Private Bag 12 Ascot Vale, Vic, AUSTRALIA 3032	ATOMIC WEAPONS ESTAB UK Building E3, Awe Aldermaston Reading, Berkshire, UK RG7 4PR
BNR London Rd. Essex, UK CM17 9NA	BRITISH AEROSPACE Wharton Aerodrome Preston, Lanc. UK PR4 1AX	BRITISH BRADCASTING CO. Kingswood Warren Harlow, Taddworth, Surrey, UK KT20 6NP
BRITISH LIBRARY Boston SPA Wetherby, W Yorks, UK LS23 7BQ	CAMBRIDGE CONSULTANTS LTD Milton Rd/Science Park Cambridge, Cambs, UK CB5 4DW	CPQD TELEBRAS Caixa Postal 1579 Predio 32 Campinas, SP, BRASIL 13088-061
CSC PROFESSIONAL SERVICES GP. 8201 Corporate Dr. #350 Harlow, Essex, UK CM17 9NA	CSELT-RADIO Via Guglielmo Reiss Romoli 274 Turin, ITALY 10148	CSIRO, CENTER FOR ADV TECH PO Box 883 Kenmore, Qld, AUSTRALIA 4069
CULHAM LAB UK Atomic Energy Auth. Abingdon, Oxfordshire, UK OX14 3D8	D L R OBERPFAFFENHOFEN Zentralbibliothek Wessling, OBB, GERMANY 8031	D S T O SALISBURY LIBRARY Box 1500 Salisbury, SA AUSTRALIA 5108
DCN INTERNATIONAL INC. 147-24 176th St. Jamaica, NY 11434-5410	DEFENCE TECH & PROCUREMENT Nemp Lab - AC Zentrum Spiez, SWITZERLAND CH 3700	DEFENSE RESEARCH ESTAB. 3701 Carling Ave. Ottawa, On, CANADA K1A 0Z2
DYNETICS, INCORPORATED PO Drawer B Huntsville, AL 35814-5050	ELECTRICAL COMMUNICATION LAB/LIB 1 2356 Take Yokosuka Shi Kanagawa, Ken, M2 JAPAN 128	FGAN/FHP Neuenahrer Strasse 20 Wachtberg GERMANY 53343
GRINAKER AVITRONICS PO Box 8492 Hennopsmeir, S. AFRICA 0046	HARRIS CORPORATION 1680 University Avenue Rochester, NY 14610-9983	HKUST LIBRARY Clear Water Bay Road Kowloon, Hong Kong
HOKKAIDO DAIGAKU Nishi 8, Kita 13 Sapporo, JAPAN 060	HUGHES RESEARCH LIBRARY 3011 Malibu Canyon Road Malibu, CA 90255-4797	HUNTING ENGINEERING LTD Redding Wood, Ampthill, Bedford, UK MK45 2HD
IABG Einsteinstrasse 20 Ottobrunn, GERMANY D-85521	IMPERIAL COLLEGE Exhibition Road London, UK SW7 2BX	IPS RADIO & SPACE LIBRARY PO Box 5606 W. Chatswood, AUSTRALIA 2057
KATHREIN-WERKE KG Postbox 100 444 Rosenheim 2, GERMANY D-8200	KERSHNER, WRIGHT & HAGAMAN 5730 Gen. Washington Dr. Alexandria, VA 22312	LINDA HALL LIBRARY 5109 Cherry Street Kansas City, MO 64110
LITTON ELECTRON DEVICES LIBRARY 960 Industrial Road San Carlos, CA 94404	MATRA DEFENSE 37 Av. Louis Breguet BP1 Velizy, Cedex, FRANCE 78146	MISSISSIPPI STATE UNIV LIBRARY PO Box 5408 Mississippi State, MS 39762
MITRE CORPORATION LIBRARY 202 Burlington Road Bedford, MA 01730	MOTOROLA INCORPORATED 1301 E Algonquin Road Schamburg, IL 60196	MPB TECHNOLOGIES INC. 151 Hymus Blvd. Pointe-Claire, CANADA H9R 1E9
NORWEGIAN TELECOM RES. PO Box 83 Kjeller, NORWAY N-2007	PARAGON TECHNOLOGY, INC. 200 Innovation Blvd. Suite 240 State College, PA 16803	PENNSYLVANIA STATE UNIV Pattee Library University Park, PA 16802

1995 INSTITUTIONAL MEMBERS (Continued)

QUEEN MARY & WESTFLD COLLEGE Mile End Road London, UK E1 4NS	RACAL ANTENNAS The Gables, S. Hampton Road Alderbury, Wilts, UK SP5 3AF	RADIO FREQUENCY SYSTEMS 36 Garden Street Kilsyth, Vic, AUSTRALIA 3137
ROCKWELL 855 35th St. NE Cedar Rapids, IA 52498	SAAB-SCANIA AB Tusta 5, Saab Military Aircraft Linkoping, SWEDEN S-58188	SPEARS ASSOCIATES INC. 249 Vanderbilt Avenue Norwood, MA 02062-5033
STG NATIONAL LUCHT-EM Ruitervest Lab. A Fokkerweg 2 Amsterdam, NETHERLANDS 1059	SWETS SUBSCRIPTION SERVICE 440 Creamery Way Suite A Exton, PA 19341	SYRACUSE RESEARCH CORP. Merrill Lane Syracuse, NY 13210-4080
TASC LIBRARY 55 Walkers Brook Drive Reading, MA 01887	TECHNICAL RESEARCH CENTRE Vit/Info Tech/PO Box 1202 Espoo, FINLAND 02044	TECHNION-ISRAEL Faculty of Electrical Engineering Technion City, ISRAEL 32000
TECHNISCHE UNIV DELFT FACULTY Elektrotech 200 Bibl/Mekelweg 4 Delft, Holland, NETHERLANDS 2628 CD	TELECOM AUSTRALIA Private Bag 37/770 Blackburn Road Clayton, Victoria, AUSTRALIA 3168	TELEX COMMUNICATIONS INC. 8601 E. Cornhusker Hwy. Lincoln, NE 68507
THORN EMI ELECTRONICS Wookey Hole Rd. Wells, Somerset, UK 13A5 1AA	UNIV. OF CENTRAL FLORIDA LIB. PO Box 162440 Orlando, FL 32816-2440	UNIV. AUTONOMA DE CHIHUAHUA Ciudad Universitaria Chihuahua-Chih, MEXICO 31170
UNIVERSITAT DER BUNDESWEHR Werner Heisenberg Weg 39 Neubiberg, GERMANY W-8014	VISTA RESEARCH INC. 100 View St, #202, Box 998 Mountain View, CA 94042	

CALL FOR PAPERS

**THE APPLIED COMPUTATIONAL ELECTROMAGNETICS SOCIETY
ANNOUNCES A SPECIAL ISSUE OF THE ACES JOURNAL ON:**

ADVANCES IN THE APPLICATION OF THE METHOD OF MOMENTS TO ELECTROMAGNETIC RADIATION AND SCATTERING PROBLEMS

The Applied Computational Electromagnetics Society is pleased to announce the publication of a 1995 Special Issue of the ACES Journal on the use of the Method of Moments in the evaluation of electromagnetic radiation and scattering problems. The objectives of this special issue are: (1) to provide the computational electromagnetics community with an assessment of the current capabilities and uses of the Method of Moments for electromagnetics problems from the low-frequency to the high-frequency regimes and (2) to provide information on recent advances that may extend range of applicability and usefulness of the Method of Moments. Prospective authors are encouraged to submit papers of archival value that address these objectives and other suggested topics listed below.

SUGGESTED TOPICS

- Modeling Guidelines for Complex Geometries
- Accuracy Assessment and Improvement
- Special Formulations: Low Frequency/High Frequency
- Hybrid Method of Moment Approaches
- New Integral Equation Formulations
- Parallelization of Moment Method Codes
- Novel Equivalence Principle Applications for the Method of Moments
- Fast Matrix Computation/Solution Techniques
- Large-Scale Problems

DEADLINE FOR PAPERS IS MARCH 31, 1995

Send papers and inquiries to:

A.W. Glisson and A.A. Kishk
Special Guest Editors
Department of Electrical Engineering
University of Mississippi
University, MS 38677

Tel: (601) 232-5353
FAX: (601) 232-7231
E-mail: eeallen@vm.cc.olemiss.edu

Call for Papers

The Applied Computational Electromagnetics Society
Announces a Special Issue of the ACES Journal on:

Applied Mathematics: meeting the challenges presented by Computational Electromagnetics

The objectives of this special issue are **a**) to illuminate some of the current mathematical techniques in computational electromagnetics, by a series of review or survey articles, and **b**) to initiate and encourage interaction between the applied mathematics community on the one hand, and the electrical engineers and physicists on the other. Papers submitted must address mathematical problems arising in computational electromagnetics, and the conclusions must have, moreover, some practical value. Contact the Guest Editors.

Suggested Topics:

- ★ Integral equations and integrodifferential equations
- ★ Eigenfunction expansions, both interior and exterior
- ★ Selfadjoint, as well as non-selfadjoint, operator approximation
- ★ Singularity expansion method, scattering poles, natural modes
- ★ Diffraction and asymptotics, application of special functions

- ★ Variational principles, Galerkin and related methods
- ★ Finite element methods, finite difference methods
- ★ The radiation boundary problem

- ★ Solution of large scale linear systems
- ★ Eigenvalue estimation, especially for non-selfadjoint problems
- ★ Optimization, conjugate and bi-conjugate gradient methods, GMRES
- ★ Numerical evaluation of integrals with oscillatory or singular integrands

Wherever possible, attention should be given to error estimates. This is not just a difficult mathematical issue¹, it is absolutely vital for all engineering considerations and it is still largely unresolved in computational electromagnetics. Modern numerical analysis seems not to have lived up to its basic premise, because we do not yet possess useful error estimates.

The deadline for papers is June 30, 1995.
Mail one hard copy to each of the Guest Editors:

Eugene Tomer
Applied Mathematics and Computing
150 Hernandez Avenue
San Francisco, CA 94127, USA
Tel: (415) 665-9555 Fax: (415) 731-3551
e-mail: etomer@netcom.com

Andrew F. Peterson
School of Electrical Engineering
Georgia Institute of Technology
Atlanta, GA 30332, USA
Tel: (404) 853-9831 Fax: (404) 853-9171
e-mail: ap16@prism.gatech.edu

¹ See, e.g., S.G. Mikhlin, *Error Analysis in Numerical Processes*, Wiley, 1991.

For information regarding ACES or to become a member in the Applied Computational Electromagnetics Society, contact Dr. Richard W. Adler. ECE Department, Code EC/AB, Naval Postgraduate School, 833 Dyer Rd, Rm. 437, Monterey, CA. 93943-5121, telephone (408) 646-1111, Fax: (408) 649-0300. E-mail 554-1304@mcimail.com. You can subscribe to the Journal and become a member of ACES by completing and returning the form below.

ACES SUBSCRIPTION FORM

please print

LAST NAME FIRST NAME MIDDLE INITIAL

COMPANY/ORGANIZATION/UNIVERSITY DEPARTMENT/MAIL STATION

PLEASE LIST THE ADDRESS YOU WANT USED FOR PUBLICATIONS

MAILING ADDRESS

CITY PROVINCE/STATE COUNTRY ZIP/POSTAL CODE

TELEPHONE FAX AMATEUR RADIO CALL SIGN

E-MAIL ADDRESS E-MAIL ADDRESS CAN BE INCLUDED IN ACES DATABASE YES NO

PERMISSION IS GRANTED TO HAVE MY NAME PLACED ON MAILING LISTS WHICH MAY BE SOLD YES NO

CURRENT SUBSCRIPTION PRICES (BELOW) ARE VALID THROUGH 31 MARCH 1995

*** NOTE AFTER 31 MARCH 1995, PRICES WILL INCREASE BY \$5.00 ***

AREA	INDIVIDUAL SURFACE MAIL	INDIVIDUAL AIRMAIL	ORGANIZATIONAL (AIRMAIL ONLY)
U.S. & CANADA	() \$ 65	() \$ 65	() \$115
MEXICO, CENTRAL & SOUTH AMERICA	() \$ 68	() \$ 70	() \$115
EUROPE, FORMER USSR TURKEY, SCANDINAVIA	() \$ 68	() \$ 78	() \$115
ASIA, AFRICA, MIDDLE EAST & PACIFIC RIM	() \$ 68	() \$ 85	() \$115

**FULL-TIME STUDENT RATE IS \$25 FOR ALL COUNTRIES
(NO INCREASE IN PRICE AFTER 31 MARCH 1995)**

Method of payment:	<input type="checkbox"/> A bank check for the total amount is enclosed. ⁽¹⁾
	<input type="checkbox"/> Traveler's checks for the total amount are enclosed. ⁽²⁾
Card Exp. date:	<input type="checkbox"/> International Money Order is enclosed. ⁽³⁾
Mo. _____ Yr. _____	<input type="checkbox"/> Charge to: <input type="checkbox"/> MasterCard <input type="checkbox"/> Visa. <input type="checkbox"/> Discover <input type="checkbox"/> Amex. ⁽⁴⁾

Card No. SIGNATURE REQUIRED

Non-USA participants may remit via (1) **Bank Checks**, if (a) drawn on a U.S. Bank, (b) have bank address, (c) contain series of (9) digit mandatory routing numbers; (2) **Traveler's Checks** (in U.S. \$\$); (3) **International Money Order** drawn in U.S. funds, payable in U.S.; (4) **Credit Cards**: Visa, Master Card, Discover Card, Amex.

March 1995

Total Remittance (U.S. Dollars Only) \$ _____

ADVERTISING RATES

	FEE	PRINTED SIZE
Full page	\$200.	7.5" x 10.0"
1/2 page	\$100.	7.5" x 4.7" or 3.5" x 10.0"
1/4 page	\$ 50	3.5" x 4.7"

All ads must be camera ready copy.

Ad deadlines are same as Newsletter copy deadlines.

Place ads with Ray Perez, Newsletter Editor, Martin Marietta Astronautics, MS 58700, PO Box 179, Denver, CO 80201, USA. The editor reserves the right to reject ads.

ACES JOURNAL AND NEWSLETTER COPY INFORMATION

<u>ISSUE</u>	<u>COPY DEADLINE</u>
March	January 25
July	May 25
November	September 25

ACES COPYRIGHT FORM

This form is intended for original, previously unpublished manuscripts submitted to ACES periodicals and conference publications. The signed form, appropriately completed, MUST ACCOMPANY any paper in order to be published by ACES. PLEASE READ REVERSE SIDE OF THIS FORM FOR FURTHER DETAILS.

TITLE OF PAPER:

RETURN FORM TO:
Dr. Richard W. Adler
Naval Postgraduate School
Code EC/AB
Monterey, CA 93943

AUTHORS(S)

PUBLICATION TITLE/DATE:

PART A - COPYRIGHT TRANSFER FORM

(NOTE: Company or other forms may not be substituted for this form. U.S. Government employees whose work is not subject to copyright may so certify by signing Part B below. Authors whose work is subject to Crown Copyright may sign Part C overleaf).

The undersigned, desiring to publish the above paper in a publication of ACES, hereby transfer their copyrights in the above paper to The Applied Computational Electromagnetics Society (ACES). The undersigned hereby represents and warrants that the paper is original and that he/she is the author of the paper or otherwise has the power and authority to make and execute this assignment.

Returned Rights: In return for these rights, ACES hereby grants to the above authors, and the employers for whom the work was performed, royalty-free permission to:

1. Retain all proprietary rights other than copyright, such as patent rights.
2. Reuse all or portions of the above paper in other works.
3. Reproduce, or have reproduced, the above paper for the author's personal use or for internal company use provided that (a) the source and ACES copyright are indicated, (b) the copies are not used in a way that implies ACES endorsement of a product or service of an employer, and (c) the copies per se are not offered for sale.
4. Make limited distribution of all or portions of the above paper prior to publication.
5. In the case of work performed under U.S. Government contract, ACES grants the U.S. Government royalty-free permission to reproduce all or portions of the above paper, and to authorize others to do so, for U.S. Government purposes only.

ACES Obligations: In exercising its rights under copyright, ACES will make all reasonable efforts to act in the interests of the authors and employers as well as in its own interest. In particular, ACES REQUIRES that:

1. The consent of the first-named author be sought as a condition in granting re-publication permission to others.
2. The consent of the undersigned employer be obtained as a condition in granting permission to others to reuse all or portions of the paper for promotion or marketing purposes.

In the event the above paper is not accepted and published by ACES or is withdrawn by the author(s) before acceptance by ACES, this agreement becomes null and void.

AUTHORIZED SIGNATURE

TITLE (IF NOT AUTHOR)

EMPLOYER FOR WHOM WORK WAS PERFORMED

DATE FORM SIGNED

PART B - U.S. GOVERNMENT EMPLOYEE CERTIFICATION

(NOTE: If your work was performed under Government contract but you are not a Government employee, sign transfer form above and see item 5 under Returned Rights).

This certifies that all authors of the above paper are employees of the U.S. Government and performed this work as part of their employment and that the paper is therefore not subject to U.S. copyright protection.

AUTHORIZED SIGNATURE

TITLE (IF NOT AUTHOR)

NAME OF GOVERNMENT ORGANIZATION

DATE FORM SIGNED

PART C - CROWN COPYRIGHT

(Note: ACES recognizes and will honor Crown Copyright as it does U.S. Copyright. It is understood that, in asserting Crown Copyright, ACES in no way diminishes its rights as publisher. Sign only if *ALL* authors are subject to Crown Copyright.)

This certifies that all authors of the above Paper are subject to Crown Copyright. (Appropriate documentation and instructions regarding form of Crown Copyright notice may be attached).

AUTHORIZED SIGNATURE

TITLE OF SIGNEE

NAME OF GOVERNMENT BRANCH

DATE FORM SIGNED

Information to Authors

ACES POLICY

ACES distributes its technical publications throughout the world, and it may be necessary to translate and abstract its publications, and articles contained therein, for inclusion in various compendiums and similar publications, etc. When an article is submitted for publication by ACES, acceptance of the article implies that ACES has the rights to do all of the things it normally does with such an article.

In connection with its publishing activities, it is the policy of ACES to own the copyrights in its technical publications, and to the contributions contained therein, in order to protect the interests of ACES, its authors and their employers, and at the same time to facilitate the appropriate re-use of this material by others.

The new United States copyright law requires that the transfer of copyrights in each contribution from the author to ACES be confirmed in writing. It is therefore necessary that you execute either Part A-Copyright Transfer Form or Part B-U.S. Government Employee Certification or Part C-Crown Copyright on this sheet and return it to the Managing Editor (or person who supplied this sheet) as promptly as possible.

CLEARANCE OF PAPERS

ACES must of necessity assume that materials presented at its meetings or submitted to its publications is properly available for general dissemination to the audiences these activities are organized to serve. It is the responsibility of the authors, not ACES, to determine whether disclosure of their material requires the prior consent of other parties and if so, to obtain it. Furthermore, ACES must assume that, if an author uses within his/her article previously published and/or copyrighted material that permission has been obtained for such use and that any required credit lines, copyright notices, etc. are duly noted.

AUTHOR/COMPANY RIGHTS

If you are employed and you prepared your paper as a part of your job, the rights to your paper initially rest with your employer. In that case, when you sign the copyright form, we assume you are authorized to do so by your employer and that your employer has consented to all of the terms and conditions of this form. If not, it should be signed by someone so authorized.

NOTE RE RETURNED RIGHTS: Just as ACES now requires a signed copyright transfer form in order to do "business as usual", it is the intent of this form to return rights to the author and employer so that they too may do "business as usual". If further clarification is required, please contact: The Managing Editor, R.W. Adler, Naval Postgraduate School, Code EC/AB, Monterey, CA, 93943, USA (408)656-2352.

Please note that, although authors are permitted to re-use all or portions of their ACES copyrighted material in other works, this does not include granting third party requests for reprinting, republishing, or other types of re-use.

JOINT AUTHORSHIP

For jointly authored papers, only one signature is required, but we assume all authors have been advised and have consented to the terms of this form.

U.S. GOVERNMENT EMPLOYEES

Authors who are U.S. Government employees are not required to sign the Copyright Transfer Form (Part A), but any co-authors outside the Government are.

Part B of the form is to be used instead of Part A only if all authors are U.S. Government employees and prepared the paper as part of their job.

NOTE RE GOVERNMENT CONTRACT WORK: Authors whose work was performed under a U.S. Government contract but who are not Government employees are required to sign Part A-Copyright Transfer Form. However, item 5 of the form returns reproduction rights to the U.S. Government when required, even though ACES copyright policy is in effect with respect to the reuse of material by the general public.

APPLIED COMPUTATIONAL ELECTROMAGNETICS SOCIETY JOURNAL

INFORMATION FOR AUTHORS

PUBLICATION CRITERIA

Each paper is required to manifest some relation to applied computational electromagnetics. **Papers may address general issues in applied computational electromagnetics, or they may focus on specific applications, techniques, codes, or computational issues.** While the following list is not exhaustive, each paper will generally relate to at least one of these areas:

- 1. Code validation.** This is done using internal checks or experimental, analytical or other computational data. Measured data of potential utility to code validation efforts will also be considered for publication.
- 2. Code performance analysis.** This usually involves identification of numerical accuracy or other limitations, solution convergence, numerical and physical modeling error, and parameter tradeoffs. However, it is also permissible to address issues such as ease-of-use, set-up time, run time, special outputs, or other special features.
- 3. Computational studies of basic physics.** This involves using a code, algorithm, or computational technique to simulate reality in such a way that better or new physical insight or understanding is achieved.
- 4. New computational techniques,** or new applications for existing computational techniques or codes.
- 5. "Tricks of the trade"** in selecting and applying codes and techniques.
- 6. New codes, algorithms, code enhancement, and code fixes.** This category is self-explanatory but includes significant changes to existing codes, such as applicability extensions, algorithm optimization, problem correction, limitation removal, or other performance improvement.
NOTE: CODE (OR ALGORITHM) CAPABILITY DESCRIPTIONS ARE NOT ACCEPTABLE, UNLESS THEY CONTAIN SUFFICIENT TECHNICAL MATERIAL TO JUSTIFY CONSIDERATION.
- 7. Code input/output issues.** This normally involves innovations in input (such as input geometry standardization, automatic mesh generation, or computer-aided design) or in output (whether it be tabular, graphical, statistical, Fourier-transformed, or otherwise signal-processed). Material dealing with input/output database management, output interpretation, or other input/output issues will also be considered for publication.

8. Computer hardware issues. This is the category for analysis of hardware capabilities and limitations in meeting various types of electromagnetics computational requirements. Vector and parallel computational techniques and implementation are of particular interest.

Applications of interest include, but are not limited to, antennas (and their electromagnetic environments), networks, static fields, radar cross section, shielding, radiation hazards, biological effects, electromagnetic pulse (EMP), electromagnetic interference (EMI), electromagnetic compatibility (EMC), power transmission, charge transport, dielectric and magnetic materials, microwave components, MMIC technology, remote sensing and geophysics, communications systems, fiber optics, plasmas, particle accelerators, generators and motors, electromagnetic wave propagation, non-destructive evaluation, eddy currents, and inverse scattering.

Techniques of interest include frequency-domain and time-domain techniques, integral equation and differential equation techniques, diffraction theories, physical optics, moment methods, finite differences and finite element techniques, modal expansions, perturbation methods, and hybrid methods. This list is not exhaustive.

A unique feature of the Journal is the publication of unsuccessful efforts in applied computational electromagnetics. Publication of such material provides a means to discuss problem areas in electromagnetic modeling. Material representing an unsuccessful application or negative results in computational electromagnetics will be considered for publication only if a reasonable expectation of success (and a reasonable effort) are reflected. Moreover, such material must represent a problem area of potential interest to the ACES membership.

EDITORIAL REVIEW

In order to ensure an appropriate level of quality control, papers are refereed. They are reviewed both for technical correctness and for adherence to the listed guidelines regarding information content. Authors should submit the initial manuscript in draft form so that any suggested changes can be made before the photo-ready copy is prepared.

<continued on next page>

STYLE FOR CAMERA-READY COPY

The ACES Journal is flexible, within reason, in regard to style. However, certain requirements are in effect:

1. The paper title should NOT be placed on a separate page. The title, author(s), abstract, and (space permitting) beginning of the paper itself should all be on the first page. The title, author(s), and author affiliations should be centered (center-justified) on the first page.
2. An abstract is REQUIRED. The abstract should state the computer codes, computational techniques, and applications discussed in the paper (as applicable) and should otherwise be usable by technical abstracting and indexing services.
3. Either British English or American English spellings may be used, provided that each word is spelled consistently throughout the paper.
4. Any commonly-accepted format for referencing is permitted, provided that internal consistency of format is maintained. As a guideline for authors who have no other preference, we recommend that references be given by author(s) name and year in the body of the paper (with alphabetical listing of all references at the end of the paper). Titles of Journals, monographs, and similar publications should be in boldface or italic font or should be underlined. Titles of papers or articles should be in quotation marks.
5. Internal consistency shall also be maintained for other elements of style, such as equation numbering. As a guideline for authors who have no other preference, we suggest that equation numbers be placed in parentheses at the right column margin.
6. The intent and meaning of all text must be clear. For authors who are NOT masters of the English language, the ACES Editorial Staff will provide assistance with grammar (subject to clarity of intent and meaning).
7. Unused space should be minimized. Sections and subsections should not normally begin on a new page.

MATERIAL, SUBMITTAL FORMAT AND PROCEDURE

The preferred format for submission and subsequent review, is 12 point font or 12 cpi, double line spacing and single column per page. Four copies of all submissions should be sent to the Editor-in-Chief. Each submission must be accompanied by a covering letter. The letter should include the name, address, and telephone and/or fax number and/or e-mail address of at least one of the authors. Only camera-ready original copies are accepted for publication, although authors may submit other copies for publication

review. The term "camera-ready" means that the material is neat, legible, and reproducible. The preferred font style is Times Roman 10 point (or equivalent) such as that used in this text. A double column format similar to that used here is preferred. **No author's work will be turned down once it has been accepted because of an inability to meet the requirements concerning fonts and format.** Full details are sent to the author(s) with the letter of acceptance.

There is NO requirement for India ink or for special paper; any plain white paper may be used. However, faded lines on figures and white streaks along fold lines should be avoided. Original figures - even paste-ups - are preferred over "nth-generation" photocopies. These original figures will be returned if you so request.

While ACES reserves the right to re-type any submitted material, this is not generally done.

Four copies of all submissions should be sent to the Editor-in-Chief. Each submission should be accompanied by a covering letter. The letter should include the name, address, and telephone of at least one of the authors.

PUBLICATION CHARGES

ACES members are allowed 12 pages per paper without charge; non-members are allowed 8 pages without charge. Mandatory page charges of \$75 a page apply to all pages in excess of 12 for members or 8 for non-members. Voluntary page charges are requested for the free (12 or 8) pages, but are NOT mandatory or required for publication. A priority courtesy guideline, which favors members, applied to paper backlogs. Full details are available from the Editor-in-Chief.

COPYRIGHTS AND RELEASES

Each primary author must sign a copyright form and obtain a release from his/her organization vesting the copyright with ACES. Forms will be provided by ACES. Both the author and his/her organization are allowed to use the copyrighted material freely for their own private purposes.

Permission is granted to quote short passages and reproduce figures and tables from an ACES Journal issue provided the source is cited. Copies of ACES Journal articles may be made in accordance with usage permitted by Sections 107 or 108 of the U.S. Copyright Law. This consent does not extend to other kinds of copying, such as for general distribution, for advertising or promotional purposes, for creating new collective works, or for resale. The reproduction of multiple copies and the use of articles or extracts for commercial purposes require the consent of the author and specific permission from ACES. Institutional members are allowed to copy any ACES Journal issue for their internal distribution only.